

Studies of Novel Gain Materials and Resonant Light Emitters for Silicon Photonics

Lewis Ashley Reeves

Doctor of Philosophy

University of York

Physics

September 2019

Abstract

Microprocessor clock speeds have stagnated in the 2010s no longer keeping up with Moore's Law. With node sizes down to 7 nm it is becoming difficult to fit more transistors onto a chip due to quantum tunneling. The energy consumption of microprocessors is also a major problem for climate change and the battery life of mobile devices. To combat these problems we look to silicon photonics to provide a solution. Transmitting data optically has two main benefits, reducing the resistive heating of electrical data transfer and increasing possible data transfer bandwidth. These two properties in concert would allow a microprocessor with optical data connects to run faster and use less energy.

The main problem with silicon photonics is the lack of an on-chip light source due to the poor light emission of silicon. An on-chip light source must be compatible with current CMOS fabrication processes and easy to mass produce. We seek to solve this problem by employing two-dimensional transition metal dichalcogenides (TMDs) as a laser gain material. Two-dimensional materials became a popular area of research after the "graphene revolution" pioneered by Andre Geim and Konstantin Novoselov. The techniques developed to produce atomically thin layers of graphene can be transferred to TMDs. TMDs exhibit the same strong in-plane bonding and weak interlayer van der Waals bonding as graphene, however when thinned down to monolayers they have a direct bandgap. The direct bandgap makes them good optical emitters.

In this thesis I review the performance of TMD microcavity emitters in the literature and then focus on two main areas, the design and fabrication of photonic crystal cavities to produce a laser resonator and the optical and structural characterisation of 2H-MoTe₂. For technological applications, large area monolayers of 2H-MoTe₂ that can be grown on a device are required. I investigate the optical and structural differences between 2H-MoTe₂ exfoliated from a bulk crystal and the CVD growth of MoTe₂.

Contents

Abstract	3
Contents	4
List of Tables	7
List of Figures	8
Acknowledgements	17
Author Declaration	19
1 Introduction	20
1.1 Background and Motivation	20
1.2 State-of-the-Art 2D TMD Light Emitters	22
1.2.1 Tungsten Diselenide Photonic Crystal Cavity	22
1.2.2 Tungsten Disulfide Microdisk	24
1.2.3 Molybdenum Disulfide Microdisk	26
1.2.4 Molybdenum Ditelluride Nanowire	27
1.2.5 Summary	28
2 Theory	29
2.1 Photonic Crystals	29
2.1.1 The Electromagnetic Wave Equation	29
2.1.2 Light Propagating in Free Space	30
2.1.3 Waveguides	31
2.1.3.1 Planar Waveguides	31
2.1.3.2 2D Waveguides	33
2.1.4 1D Photonic Crystal Band Gap	34
2.1.5 2D Photonic Crystal Band Gap	35
2.1.5.1 2D Photonic Crystal Slab	36

2.1.6	Defects in 2D Photonic Crystal Slabs	38
2.1.6.1	2D Photonic Crystal Cavities	39
2.1.7	Q-factor Optimization of 2D Photonic Crystal Cavities	40
2.1.8	Farfield Optimization of 2D Photonic Crystal Cavities	43
2.2	2D Materials	44
2.3	Conditions for Lasing	46
2.3.1	Laser Fundamentals	47
2.3.1.1	Semiconductor Laser Gain Medium	48
2.3.1.2	Pump Source	48
2.3.1.3	Optical Resonators	49
2.3.1.4	Lasing Threshold	49
2.3.2	Quantum Threshold	50
2.3.3	Linewidth Narrowing	51
2.3.4	Hanbury-Brown and Twiss Experiment	53
2.3.5	Beta Factor	54
2.3.6	Explanation of Apparent Lasing	55
2.3.7	Summary	56
3	Photonic Crystal Cavities	58
3.1	Nanofabrication of Photonic Crystal Cavities	58
3.1.1	Substrate Preparation	59
3.1.2	Spin Coating	60
3.1.3	Electron-beam Lithography	61
3.1.3.1	Resists	61
3.1.3.2	Resist Development	62
3.1.3.3	Design of Electron Beam Lithography Pattern	63
3.1.3.4	RAITH Voyager Electron Beam Lithography	63
3.1.4	Reactive Ion Etching	66
3.1.5	Resist Removal	71
3.1.6	Underetching the Cavity	71
3.1.7	Summary	72
3.2	Optical Characterization	73
3.2.1	Resonant Scattering	73
3.2.1.1	Theory of Resonant Scattering	74
3.2.1.2	Resonant Scattering Setup	75
3.2.1.3	Results	77
3.2.2	Tunable Laser	80
3.2.3	Emission from Silicon	81

3.2.3.1	Optical Setup	82
3.2.3.2	Measurements	83
3.2.4	Summary	84
4	2D Materials	85
4.1	Exfoliation of Molybdenum Ditelluride	85
4.2	CVD growth of Molybdenum Ditelluride	90
4.2.1	Molybdenum Ditelluride CVD Procedure	90
4.3	Structural Characterisation	92
4.3.1	Raman Spectroscopy	92
4.3.2	X-Ray Diffraction	94
4.3.3	Transmission Electron Microscopy	96
4.3.3.1	Imaging	97
4.3.3.2	Selected-area Diffraction	97
4.3.3.3	Exfoliated Molybdenum Ditelluride	100
4.3.3.4	CVD Molybdenum Ditelluride	102
4.3.4	Summary of Structural Characterisation Measurements . .	103
4.4	Optical Characterisation	104
4.4.1	Microphotoluminescence	104
4.4.2	Design and Optimisation of Optical Setup	104
4.4.2.1	Czerny-Turner Spectrometers	106
4.4.2.2	Dispersion and Bandpass	107
4.4.2.3	Coupling Light to Spectrometers	108
4.4.2.4	Array Detectors	109
4.4.2.5	Objectives	112
4.4.2.6	Array Detector Performance	113
4.4.3	Temperature Dependent Microphotoluminescence of Silicon	116
4.4.4	Room Temperature Microphotoluminescence of Molybdenum Ditelluride	119
4.4.5	Temperature Dependent Microphotoluminescence of Molybdenum Ditelluride	121
4.4.6	Photoluminescence from CVD Molybdenum Ditelluride . .	123
4.5	Summary	124
5	Conclusions	126
5.1	Future Work	128
	References	130

List of Tables

2.1	Comparison of the four TMD light emitters in light of the lasing conditions put forward [41, 42].	47
3.1	RAITH Voyager EBL specification.	63
3.2	Silicon RIE etch chemistry.	68
3.3	Silicon RIE recipe.	69
4.1	Spectrometer resolution (nm) for C-T spectrometers with $f = 150, 300, 500, 750$ mm.	107
4.2	Specification comparison between Andor iDus DU490A [79] and Princeton Instruments PyLon-IR:1024-1.7 [80].	111
4.3	Microscope objective specifications.	112
4.4	Varshni function fit data for monolayer (ML) MoTe_2 and bilayer (BL) MoTe_2	122

List of Figures

- 1.1 (a) Cartoon depiction of the device architecture, where the electric field profile (in plane, xy) of the fundamental cavity mode (pristine cavity before WSe_2 transfer) is embedded as the color plot. Inset: cartoon of the atomic structure of the monolayer. (b) Light output intensity as a function of the optical pump power (L-L curve) at 130 K. Red filled squares correspond to the cavity emission. Violet half-filled squares correspond to the spontaneous emission (SE) off cavity resonance. Solid lines are the simulated curves using the laser rate equation with different β -factors. $\beta = 0.19$ is the best fit to the lasing data. Dark gray dashed line corresponds to the defined laser threshold, labeled by "Thd." (c) L-L curve for the same lasing device at 80 K (red squares), where the solid line is a guide for the eye to the transition region. (d) Photoluminescence spectra for increasing pump power. The solid lines are Lorentzian fits to the photoluminescence spectra. (e) Cavity linewidth as a function of the detected output power at 160 K (open red squares). Dashed line is a guide to the eye to the nonlinear line width rebroadening area, which corresponds to the lasing threshold region. Figure and caption reproduced from Ref. [13]. 23

- 1.2 (a) Schematic image of a monolayer WS_2 microdisk device highlighting the $\text{Si}_3\text{N}_4/\text{WS}_2/\text{HSQ}$ sandwich structure. (b) Experimental data and rate equation analytical fits. The best fit to the experimental data gives a threshold pump intensity of $\approx 5\text{-}8 \text{ MW cm}^{-2}$ with a spontaneous emission factor, β , of 0.5. The fits to β of 0.005, 0.05, and 1 are also presented for comparison. (c) Steady-state photoluminescence emission spectra with increasing pump intensity, normalized to pump intensity, illustrating the transition from spontaneous emission to stimulated emission and lasing. (d) Monolayer WS_2 photoluminescence background and cavity emissions as a function of pump intensity. Dashed lines represent linear fits to the experimental data. The WS_2 photoluminescence background emission shows a linear dependence on the pump intensity, and the green dashed lines (cavity emission) show a kink indicating the onset of superlinear emission and lasing operation. (e) FWHM versus input pump intensity. Linewidth narrowing of the lasing mode is observed as the excitation intensity exceeds the lasing threshold. The red dashed line is a guide to the eye. Figure and caption reproduced from Ref. [15]. 25
- 1.3 (a) Schematic configuration of the coupled microsphere/microdisk optical cavity with the incorporation of 2D MoS_2 . (b) RT-micro-PL spectra of the laser device with an excitation power of $3 \mu\text{W}$ (lower spectrum) and $30 \mu\text{W}$ (upper spectrum). (c) L-L plot of the integrated intensity as a function of excitation power. Figure and caption reproduced from Ref. [12]. 26

- 1.4 (a) Crystal structure of MoTe_2 (2H). (b) Device schematic (silicon photonic crystal nanobeam laser structure suspended in air with a monolayer of MoTe_2 on top). (c) PL spectra of the nanobeam light emitter with increasing pump power levels at room temperature. (d) Fitting of the PL spectra for different pump levels. Solid squares represent the measured data points. The lines represent Lorentzian fits. (e) SEM of an undercut silicon nanobeam cavity. (f) Log-log plot of light in versus light out for the first two modes and for a background spontaneous emission. The solid squares represent data from experimental measurements, and the solid line is a rate-equation fitting. (g) Linewidth (black) and resonant wavelength (blue), with arrows pointing to their respective axes, versus pump power. Figure and caption reproduced from Ref. [17]. 27
- 2.1 (a) A schematic diagram of the self-consistency condition for a planar waveguide. (b) A dispersion diagram for the TE modes of a planar waveguide. 32
- 2.2 (a) A schematic of a silicon nanowire waveguide on SOI substrate. (b) A schematic of a polymer strip-loaded waveguide on thermal oxide on silicon wafer. The electric field profiles $TE_{0,0}, |E_y|^2$ were simulated using EIMS [19] and overlaid onto a schematic diagram. 33
- 2.3 Schematic diagram of (Left) 1D periodic dielectric stack, in the z -direction with high (n_2) and low (n_1) refractive indices. The field intensity of the two standing wave solutions is shown upper wave (ω^+) and lower wave (ω^-). (Right) Band diagram of the 1D dielectric stack shown on the left. The band gap is highlighted in yellow and the irreducible Brillouin zone is highlighted in orange. Figure adapted from [18]. 35
- 2.4 Band-diagram of a two-dimensional photonic crystal (infinite in z -direction) ($n_1 = 3.5$) with hexagonal array of air holes ($n_2 = 1, r/a = 0.35$), as shown in the right inset. The directions of the wavevector are shown in the left inset with specific points corresponding to the graph. The red lines show the bands with the electric field in-plane (TE modes). The dashed blue lines show the bands with the electric field out of plane (TM modes). Mode calculations performed by Dr Bryan J O'Regan. 37

2.5	Band-diagram of a two-dimensional photonic crystal slab (220 nm z -direction) ($n_1 = 3.5$) with hexagonal array of air holes ($n_2 = 1, r/a = 0.35$), as shown in the right inset. The directions of wavevector are shown in the left inset with specific points corresponding to the graph. The red lines show the bands with the electric field in-plane (TE modes). The light lines are shown with dashed lines and the leaky region is highlighted in grey. Mode calculations performed by Dr Bryan J O'Regan.	38
2.6	Ln-type photonic crystal cavities. Left to right: L3, L5, and L7 photonic crystal cavities.	39
2.7	Schematic of the gentle confinement L3 cavity. The holes in red are shifted away from the cavity by $\Delta x/a$ and have radius r'	41
2.8	(a) Schematic diagram of a standing wave within a perfectly reflecting Fabry-Perot cavity, the square envelope function is in blue. (b) Schematic of a standing wave in a distributed Bragg reflector with a defect. This is similar to the gentle confinement case. The Gaussian envelope curve is in blue.	41
2.9	(a) & (b) The electric field profile inside a cavity with a very short (2.5λ) length, and the spatial FT spectra. The leaky region is indicated as a blue area. (c) & (d) The electric field profile with a gentle envelope function (Gaussian curve) and its spatial FT spectrum. Reproduced from [26].	42
2.10	(a) The electric field profile (E_y) of the fundamental mode of photonic crystal cavity. (b) The FT spectra of (a). The region inside the grey circle corresponds to the leaky region. (c) & (d) The electric field profile and 2D FT spectrum, respectively, for the L3 cavity. Figure and caption reproduced from Ref. [26].	42

- 2.11 (a) Schematic of far-field optimized L3 PhCC. Holes with red edge are shrunk and shifted to optimize the Q-factor. Dark holes are modified to increase the vertical out-coupling. (b) Calculated Q-factor and out-coupling efficiency (η_{out}) as a function of radius variation of the alternating holes highlighted in yellow. (c) A selection of calculated far-field patterns (electric field intensity profile, $|E|^2$) corresponding to the labeled numbers on the efficiency plot (see numbers in panel (b)). Field intensities are normalized to the total emitted power in the vertical half-space. Concentric circles correspond to $\theta = 20^\circ, 30^\circ, 40^\circ, 50^\circ, 60^\circ, 90^\circ$ from the inner to the outer one, respectively. Figure and caption reproduced from Ref. [28]. 43
- 2.12 Schematic bandstructure of monolayer TMDs showing the circular dichroism and the K and K' valleys. The K and K' valleys are energy degenerate due to the inversion symmetry of the 2D Brillouin zone. The interband transitions at the K point are coupled to σ^+ circularly polarised light and at the K' point the interband transitions are coupled to σ^- circularly polarised light. These valley specific selection rules are the basis of valleytronics. 45
- 2.13 Photoluminescence (PL) spectra of a variety of monolayer TMDs at room temperature. The PL intensities are each normalized to unity for ease of comparison. Data is shown for MoTe₂ [14], MoS₂ [39], WSe₂ [39], and WS₂ [40]. 46
- 2.14 Jablonski diagram of (a) spontaneous emission and (b) stimulated emission. 48
- 2.15 (a) Different types of light classified by a Hanbury-Brown-Twiss measurement. Injection current dependences of (b) photon number and (c) equal-time second-order photon correlation for an emitter consisting of 50 QDs in a cavity with a spontaneous emission factor $\beta = 0.01$. The different curves correspond to photon loss rates $\gamma_c = 10^{10} \text{ s}^{-1}$, $5 \times 10^{10} \text{ s}^{-1}$, 10^{11} s^{-1} , and $5 \times 10^{11} \text{ s}^{-1}$. QD, quantum dot. Figure reproduced from Ref. [44]. 52
- 2.16 Equal-time intensity correlation versus pump power for a QD-micropillar (a) LED, (b) cavity-enhanced LED, and (c) laser. The gray curves represent theory. The data points are from experiment, where the solid symbols indicate $g^{(2)}(0)$ analysis by integration and the open symbols indicate fits considering the instrument impulse response of the setup. Figure and caption reproduced from Ref. [49]. 54

3.1	Overview of nanofabrication steps for photonic crystal cavities. (1) Sample cleaning and spin coating. (2) Electron beam lithography exposure. (3) Development. (4) Reactive-ion etching. (5) Resist removal. (6) Underetching.	58
3.2	(a) Forward and backscattering effects for electrons entering a resist and a substrate. Secondary electrons SE_I are formed in the path of the beam after a forwards scattering event, SE_{II} are secondary electrons formed after a backscattering event. (b) Exposure of a single point due to the point spread function of the EBL process.	66
3.3	EBL exposure of two points closely placed together. The black line is the total exposure due to the combination of SE_I and SE_{II} electrons.	66
3.4	Schematic diagram of the reactive-ion etching system used in this PhD project.	67
3.5	Schematic of etching processes of silicon within the RIE system.	70
3.6	Schematic diagram showing the RIE etch depth dependence with feature size.	71
3.7	SEM micrograph of undercut photonic crystal membrane fabricated and imaged as a part of this PhD project. The etched area next to the photonic crystal shows that none of the thermal oxide layer remains. The light area surrounding the undercut marks the extent of the etch laterally.	72
3.8	Broadband light sources for examining photonic crystal cavity resonances. Spectra measured using an Ando AQ6317B optical spectrum analyser (OSA) and plotted with normalised intensity.	74
3.9	Schematic diagram of the resonant scattering setup built at York (a) used to characterize the fabricated photonic crystal cavities. Either a broadband SLD or a tunable laser is linearly polarized [P] and focused onto the cavity by a microscope objective. The cavity emission is collected by the objective and directed to the spectrometer/detector via a beamsplitter and an analyzer [A]. (b) A L3 PhCC is mounted at 45° with respect to the polarizer and analyzer. The cavity polarization is illustrated by the red arrow.	75
3.10	Clover leaf spot pattern when the analyzer is perpendicular to polarizer. (a) Simulation from Ref. [57]. (b) Image of cloverleaf pattern obtained from the resonant scattering setup built in York.	76

3.11	(a) L3 PhCC with tightly focused excitation spot. (b) L3 PhCC with slightly defocused excitation spot. (c) Fano lineshape plotted as a function of q from Equation 3.2.	77
3.12	(a) L3 PhCC with period $a = 324$ nm with tightly focused excitation producing asymmetric lineshape. (b) L3 PhCC with period $a = 324$ nm with tightly focused excitation producing asymmetric lineshape. . . .	78
3.13	Resonant scattering spectra of L3, L5 and L7 PhCC with period $a = 320$ nm. Resonant wavelength (1270 nm) normalized to compare each cavity length.	79
3.14	Q -factors of L3, L5 and L7 PhCC with period $a = 320$ nm.	80
3.15	Tunable laser resonant scattering spectrum of PhCC with resonance at 1554.5 nm and Q -factor of 45000.	81
3.16	Schematic diagram of silicon photoluminescence setup.	82
3.17	Stacked spectra of L3, L5, L7 and L9 cavities with period $a = 310$ nm plotted on a normalised wavelength scale. Lorentzian lineshapes are fitted to the cavity peaks.	83
3.18	Plot of the quality factor of the resonance with respect to cavity length Ln for L3, L5, L7 and L9 cavities.	84
4.1	Optical microscope images at 50x magnification of (a) MoTe ₂ flake on PDMS substrate and (b) MoTe ₂ flake on 300 nm SiO ₂ -on-Si substrate.	86
4.2	Inset: Optical contrast image of MoTe ₂ flake from Figure 4.1(b). The layers of flake are outlined using a dashed line with number of layers annotated. Graph: Linescan (green line in inset) of green pixel values. Linear fits to pixel value with associated number of layers determined by a linear fit to average pixel values for each step.	87
4.3	The PDMS dry transfer method. The flake to be transferred is exfoliated onto a PDMS stamp (1) and the stamp is then attached to a glass slide connected to a micromanipulator (2). Using a microscope, the flake can be aligned with the final substrate (3) and brought in contact (4). By slowly peeling of the PDMS stamp (5), the flake can be deposited on the substrate (6). Figure reproduced from Ref. [67].	88
4.4	Photograph of the York 2D material transfer system designed by Dr Yue Wang.	89
4.5	2H and 1T' polymorphs of MoTe ₂ . Circles in blue represent molybdenum atoms and circles in yellow represent tellurium atoms. Figure reproduced from Ref. [72].	90
4.6	Diagram of CVD growth furnace.	91

<i>List of Figures</i>	15
4.7 Jablonski diagram representing energy transitions for Rayleigh and Raman scattering.	92
4.8 Raman spectrum performed under inert atmosphere of unoxidized CVD 2H-MoTe ₂ . Figure courtesy of James Fraser University of Glasgow.	93
4.9 Raman spectra of (a) 2H-MoTe ₂ (b) 2H+1T'-MoTe ₂ (c) 1T'-MoTe ₂ . Figure reproduced from Ref. [72].	94
4.10 The $\theta - 2\theta$ XRD measurement geometry. Crystal planes are shown in red. The x-ray beam k_0 and detector k_g are scanned simultaneously maintaining \mathbf{K} perpendicular to the crystal planes.	95
4.11 $\theta - 2\theta$ XRD spectrum of 2H-MoTe ₂ bulk crystal provided by HQ Graphene.	95
4.12 $\theta - 2\theta$ XRD spectrum of 3.5 nm CVD 2H-MoTe ₂ on (100) cut SOI. XRD conducted by of James Fraser at University of Glasgow.	96
4.13 The two basic operations of the TEM imaging system involve (A) diffraction mode: projecting the diffraction pattern (DP) onto the viewing screen and (B) image mode: projecting the image onto the screen. In each case the intermediate lens selects either the back focal plane (BFP) (A) or the image plane (B) of the objective lens as its object. Figure reproduced from Ref. [75].	98
4.14 Several kinds of DPs obtained from a range of materials in a conventional 100-kV TEM: (a) amorphous carbon, (b) an Al single crystal, (c) polycrystalline Au, (d) Si illuminated with a convergent beam of electrons. In all cases the direct beam of electrons is responsible for the bright intensity at the center of the pattern and the scattered beams account for the spots or rings that appear around the direct beam. Figure reproduced from Ref. [75].	99
4.15 (a) Bright-field TEM image of a 2H-MoTe ₂ flake. (b) Dark-field TEM image of the same 2H-MoTe ₂ flake at higher magnification. TEM by Dr Jon Barnard.	101
4.16 (a) SAD diffraction pattern of a 2H-MoTe ₂ flake. (b) HR-TEM of a 2H-MoTe ₂ flake. TEM by Dr Jon Barnard.	101
4.17 (a) Bright-field TEM image of CVD 2H-MoTe ₂ flake. (b) Magnified bright-field TEM image of CVD 2H-MoTe ₂ flake. TEM by Dr Jon Barnard.	102
4.18 (a) SAD diffraction pattern of CVD 2H-MoTe ₂ flake. (b) HR-TEM of CVD 2H-MoTe ₂ flake. TEM by Dr Jon Barnard.	103

4.19	Diagram of microphotoluminescence setup built as a part of this PhD. A 532 nm laser is expanded by a beam expander then is focussed onto the sample using a long working distance objective. The photoluminescence is captured by the objective and the excitation laser is filtered by a longpass beamsplitter. The photoluminescence is analysed using a spectrometer with an InGaAs array detector.	105
4.20	Diagram of Acton Spectrapro 2750 with dual CCD ports. Figure reproduced from Ref. [78].	106
4.21	Schematic of blazed grating geometry.	108
4.22	520 cm^{-1} silicon Raman peak measured with objectives with varying numerical aperture. N.B. the 1.42NA objective uses an immersion oil with $n = 1.52$. 100x objective and 20x objective have been magnified by 10 times to be visible on the same scale.	113
4.23	Dark noise comparison between the Princeton Instruments PyLon detector cooled to -100°C and the Andor iDus cooled to -75°C	114
4.24	PL count rate comparison between the Princeton Instruments PyLon-IR and the Andor iDus using a GaAs quantum dot sample with identical excitation conditions.	115
4.25	Schematic illustrations of (a) radiative recombination processes in Si, (b) energy band diagram and (c) density distribution of electrons in conduction band and holes in valence band. Figure reproduced from Ref. [85].	116
4.26	Silicon photoluminescence from SoI at varying temperatures.	117
4.27	Plot of silicon temperature dependant bandgap from the Varshni relation (black). Measured photoluminescence peak energy (red). Full-width half-maximum of photoluminescence (blue).	118
4.28	Fitted Maxwell Boltzmann distributions to temperature dependent photoluminescence of SoI Figure 4.26. Inset: Phonon energy from Maxwell Boltzmann fit.	119
4.29	Monolayer and bilayer MoTe_2 photoluminescence.	120
4.30	Temperature dependent photoluminescence of MoTe_2	121
4.31	Photoluminescence peak energy of monolayer (red circles) and bilayer (black squares) MoTe_2 versus temperature. The solid red lines represent fits by the Varshni function.	122
4.32	Stacked photoluminescence plot of O_2 plasma treated CVD MoTe_2 at 40, 10, 7.1, 6.3 and 5 K.	124

Acknowledgements

I would like to thank the photonics group at York both past and present. Dr Chris Reardon for all your encouragement and great discussions. Dr Yue Wang for all of your help with 2D materials, I hope the μ PL setup brings you success during your fellowship. Dr Jose Juan-Colas, Dr Donato Conteduca, Alexander Drayton, George Duffett, Manuel Deckart, Josh Male, Dr Ben Coulson. And past members Dr Daan Stellinga, Dr Graham Triggs, Dr Bryan O'Regan, Dr Mark Scullion and Dr Matthias Fischer.

Thank you to the Technical staff in the Physics department: Jason Flatt, Adam Stroughair, Dr Andy Vick and Dave Coulthard. To my TAP members Prof Andrei Andreyev and Dr Stuart Cavil, Dr Alison Laird and Prof Kieran Gibson for support during tough times.

Thank you to Marco Clementi and Dr Matteo Galli for your warm welcome at University of Pavia and teaching me the ways of Resonant Scattering.

Thanks to Dr Alexey Ganin and James Fraser for the CVD growth of MoTe_2 and characterisation.

To Dr Andrew Pratt and Dr Iain Crowe, thank you for taking the time to read this thesis and the in depth discussions about this work at viva. The advice you gave has greatly improved this thesis.

I would like to thank everyone who made my time during this PhD at York a pleasurable experience. From the Magnetic Materials group: Dr Will Frost, Dr John Sinclair, Dr Ed Jackson, Joe Gompertz and Dan Clarke. From the Nuclear Physics Group: Dr James Cubiss, Prof David Jenkins, Dr Ruchi Garg, Dr Nick Hubbard and Dr Jos Riley. From the York Plasma Institute: Dr James Dedrick and

Dr Chris Murphy. Prof Kevin O'Grady for your encouragement and thesis writing methodology. Dr Nikky Farthing and Sarah Jenkins for all the great times during the PhD. To Paul and Mandy Marshall at the Rook who are always there with a pint and a chat when I've needed them. Tom Bacon and Zac Gorley for all the great nights at the Rook and Brew York.

To Dr Dom Reed and Martyn Gosling, thank you for all the memories during the MPhys. To Dr Mike Laverick, thank you for all the great times we've had in York and my visits to Leuven. Our nights in the Oude Markt and Seven Oakes were memorable albeit hazy!

Much gratitude for all the amazing times I've had outside the PhD with Simon Peel Yates, Smiley Dave, Jack and Tom Watson, Debora Claudio, Freddie Green, Michelle Cee, Ollie Route, Max Such, Ryan Cornall, Griffin Dickinson, Ryan Hamilton, Harry Jennings, Grant Knight, Youssef Ashraf, Rou Reynolds, Danny Price, Dave Dearing, Corrine Cummings and Stevie D, gone but never forgotten.

I would like to thank my father, Bal, and my grandparents John and Lyn for their support throughout my life.

And finally, my dearest, Alastair without your endless support and encouragement I don't think I would have been able to achieve this. Don't worry I'll repay you when it comes time for your thesis!

Author Declaration

I declare that this thesis is a presentation of original work and I am the sole author. This work has not previously been submitted for an award at this, or any other, University. All sources are acknowledged as References.

List of Publications

1. L. Reeves et al. "2D Material Microcavity Light Emitters: To Lase or Not to Lase". In: *Advanced Optical Materials* 6.19 (2018), pp. 1-11. DOI: 10.1002/adom/201800272

1 Introduction

1.1 Background and Motivation

The clock speed of microprocessors has increased exponentially since 1965, as predicted by Intel CEO Gordon Moore [1] who foresaw that microprocessor speeds would be likely to double every 18 months. In fact, Moore predicted that by 1975 as many as 65000 components could be squeezed onto a single silicon chip. In 2019, AMD produced their 64 core Epyc CPU containing 32 billion transistors[2]. While Moore's law has held until recently, it has begun to slow down and clock speeds have remained relatively stable in the 2010's with effort being spent to improve power efficiency and add more cores to larger dies as to leverage parallel processing. This slow down can be attributed to transistor node size shrinking from 10 μm in 1970 to 7 nm in 2019. Transistors can no longer be made smaller due to the problematic quantum tunneling of electrons from the source to drain in metal-oxide semiconductor field-effect transistors (MOSFETs). Another problem faced when increasing clock speed is the dynamic power consumption of activating logic gates in the CPU. The dynamic power consumption scales proportionately to the CPU frequency. This is a major problem for CPUs that are widely integrated into mobile devices where battery life is critical. It is also a major environmental problem due to the energy consumption of data centers with current figures putting global data centers as exceeding 200 TWh of energy (around 1% of global energy usage) [3]. Data centre electricity use is projected to increase 15-fold by 2030 which equates to 8% of projected global demand [4].

One solution to the heating problem is to replace as much electrical wiring as possible with optical interconnects. Optical data transmission is widely adopted for transoceanic data cables, with these forming the backbone of the internet.

Optical fibers to personal premises are becoming more ubiquitous and optical data connections are linking servers together in datacenters through use of products developed by companies like Luxtera [5]. To further increase computer speeds and reduce power consumption, optical interconnects need to be brought on-chip [6] and this is where silicon photonics will play a crucial role. Silicon photonics is a mature technology in which high-performance modulators [7], detectors [8], and waveguides [9] are already well developed. The larger inherent bandwidth of silicon photonics disentangles the link between bandwidth and power consumption. Bandwidth can also be increased by wavelength division multiplexing (WDM). The missing piece in the silicon photonics jigsaw is a light source that can be easily implemented with current CMOS processing techniques. Silicon itself is a poor light emitter due to its indirect bandgap which has resulted in other materials being investigated commercially by Intel and IBM. A popular approach is hybrid integration where a III-V laser module is bonded to a Si chip. Intel's approach [10] was to directly bond an AlGaInAs strained Quantum Well (QW) laser operating at 1550 nm to a waveguide and evanescently couple the light in. Active alignment between the laser and waveguide were required during the bonding process which added cost and complexity along with a poor yield. These insurmountable problems hampered commercialization of this technology.

To address the lack of an on-chip light source for silicon photonics, we have investigated two-dimensional materials such as transition metal dichalcogenides (TMDs). 2D materials gained notoriety in 2010 when Andre Geim and Konstantin Novoselov won the Nobel Prize in Physics for their work on graphene. There are a whole family of 2D materials ranging from conducting graphene to insulating hexagonal boron nitride. The family of 2D materials are characterized by their strong in-plane bonding and weak interlayer van der Waals bonding. This weak interlayer bonding allows for them to be exfoliated mechanically by the "scotch tape" method *citescotchtape*. Of most interest for silicon photonics are the transition metal dichalcogenides which are semiconducting. When thinned to a monolayer, the TMDs exhibit direct bandgaps which is opposed to their bulk behaviour where they exhibit an indirect bandgap. This direct bandgap make them good optical emitters. They also exhibit strong exciton binding energies and high mobility [11]. Most research into 2D material light sources have focused on TMDs which emit in the visible wavelength range. These include molybdenum disulfide, MoS₂ [12], and tungsten diselenide, WSe₂ [13]. The problem with these TMDs is that silicon absorbs light below 1100 nm which

renders these visible light sources unsuitable for silicon photonics. TMDs with lower bandgap energies emitting above 1100 nm are good candidates for a 2D material on-chip light source. Of particular interest is molybdenum ditelluride MoTe_2 . MoTe_2 has a bandgap of 1.1 eV (1130 nm) [14] which is just within the transparency window of silicon.

In the next section we will review four transition metal dichalcogenide light emitting devices from the literature.

1.2 State-of-the-Art 2D TMD Light Emitters

Based on these favorable properties, it is no surprise that researchers have sought to realize laser action using TMD gain materials. So far, all reported laser devices are optically pumped, but electrical pumping is a real possibility given the ability of forming sandwich structures with boron nitride as the insulator and graphene as the electrode.

1.2.1 Tungsten Diselenide Photonic Crystal Cavity

The first nanoscale laser with two-dimensional gain material was reported by Wu et al. in 2015 [13]. The team transferred a monolayer of tungsten diselenide (WSe_2) onto an L3 photonic crystal (PhC) cavity fabricated in a gallium phosphide thin membrane (Figure 1.1). Gallium phosphide was chosen as the substrate because its bandgap energy is higher than the WSe_2 emission energy. The L3 PhC cavity, which is a line defect cavity created by the removal of three adjacent holes, was tuned to be resonant around the PL peak at low temperature, i.e., 740 nm. The cavity exhibited a loaded Q-factor of 1300 at room temperature which increased to 2500 when the device was cooled to cryogenic temperatures.

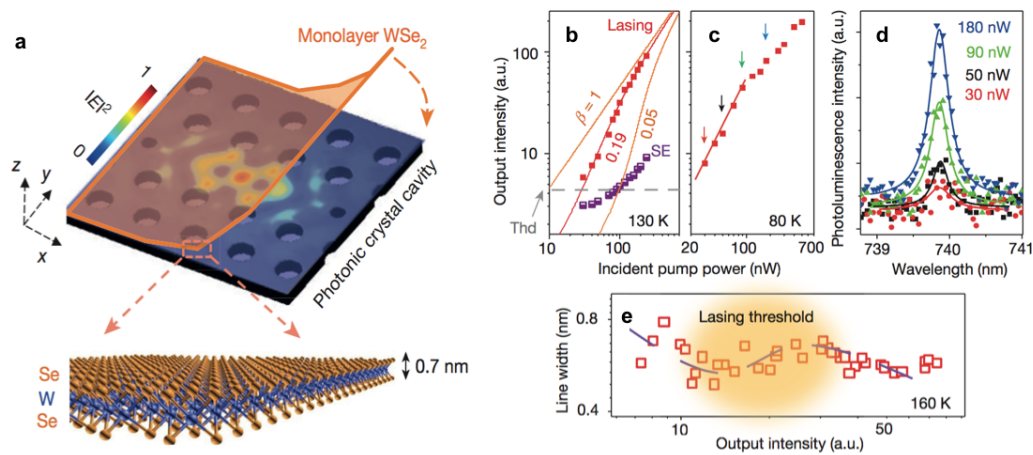


Figure 1.1: (a) Cartoon depiction of the device architecture, where the electric field profile (in plane, xy) of the fundamental cavity mode (pristine cavity before WSe₂ transfer) is embedded as the color plot. Inset: cartoon of the atomic structure of the monolayer. (b) Light output intensity as a function of the optical pump power (L-L curve) at 130 K. Red filled squares correspond to the cavity emission. Violet half-filled squares correspond to the spontaneous emission (SE) off cavity resonance. Solid lines are the simulated curves using the laser rate equation with different β -factors. $\beta = 0.19$ is the best fit to the lasing data. Dark gray dashed line corresponds to the defined laser threshold, labeled by "Thd." (c) L-L curve for the same lasing device at 80 K (red squares), where the solid line is a guide for the eye to the transition region. (d) Photoluminescence spectra for increasing pump power. The solid lines are Lorentzian fits to the photoluminescence spectra. (e) Cavity linewidth as a function of the detected output power at 160 K (open red squares). Dashed line is a guide to the eye to the nonlinear line width rebroadening area, which corresponds to the lasing threshold region. Figure and caption reproduced from Ref. [13].

A remarkable feature of this device was that the gain material was placed in the evanescent tail of the cavity, not at the center. Using finite-difference time-domain simulation (Figure 1.1(a)), however, the intensity of the lasing mode at the position of the monolayer was found to be 40% of the maximum, which showed that strong gain-cavity coupling can be achieved even via the evanescent tail.

The emission spectrum of the laser is shown in Figure 1.1(d), obtained by pumping with a 632 nm continuous wave laser at 80 K. The device emits at 739.5 nm with a linewidth of 0.3 nm FWHM. The emission is polarized in the y -direction

which is consistent with the cavity polarization. Figure 1.1(b) and 1.1(c) show plots of the output intensity as a function of incident pump power indicating lasing action at 130 K (b) and 80 K (c). The typical nonlinear "kink" in the L-L curve is clearly apparent. The β -factor, which is the fraction of spontaneous emission coupled into the lasing mode, was deduced by fitting the cavity laser rate equations. A β -factor of 0.19 was found to be the best fit as shown in Figure 1.1(b). The threshold was found to be 27 nW corresponding to a pump density of $\approx 1 \text{ W cm}^{-2}$ and linewidth narrowing was observed around the lasing threshold Figure 1.1(e).

1.2.2 Tungsten Disulfide Microdisk

Shortly after this first demonstration, Ye et al. presented a monolayer excitonic microcavity light emitter[15] based on a monolayer of tungsten disulfide (WS_2) placed onto a silicon nitride microdisk resonator. A schematic view of the device is shown in Figure 1.2(a).

A monolayer of WS_2 has a direct bandgap around 2 eV (Figure 1.2), corresponding to a photoluminescence peak at 610 nm. The WS_2 is sandwiched between the silicon nitride microdisk resonator and a thin layer of hydrogen silsesquioxane (HSQ) (Figure 1.2(a)), which serves to enhance the lasing mode overlap with the gain material, additionally encapsulating the WS_2 to prevent degradation by exposure to air. This encapsulation serves the additional purpose of increasing the optical confinement factor by $\approx 30\%$ compared to the monolayer directly placed on the cavity.

The microdisk structure was designed to have a diameter of $3.3 \mu\text{m}$ to give a strong TE polarized whispering gallery mode (WGM) resonance at 612 nm. The small diameter of the cavity increases the free spectral range hence there is only one mode available within the gain bandwidth. The Q-factor of the cavity is $Q = 2604$. The device was cooled to 10 K and optically pumped with a 190 fs pulsed 473 nm laser and emission spectra collected via a 50 x objective. The emission characteristics as a function of pump power density are shown in Figure 1.2(c). Above 22.4 MW cm^{-2} , the intensity of the peak at 612 nm increases sharply, suggesting lasing. A nonlinear "kink" in the L-L curve is shown in Figure 1.2(b)

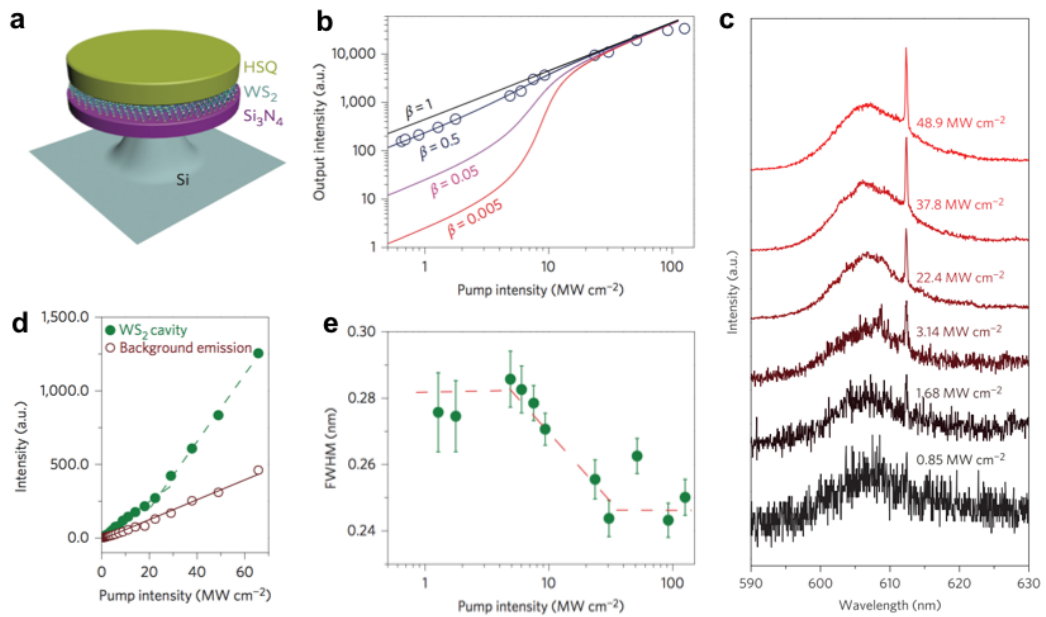


Figure 1.2: (a) Schematic image of a monolayer WS_2 microdisk device highlighting the $\text{Si}_3\text{N}_4/\text{WS}_2/\text{HSQ}$ sandwich structure. (b) Experimental data and rate equation analytical fits. The best fit to the experimental data gives a threshold pump intensity of $\approx 5\text{--}8 \text{ MW cm}^{-2}$ with a spontaneous emission factor, β , of 0.5. The fits to β of 0.005, 0.05, and 1 are also presented for comparison. (c) Steady-state photoluminescence emission spectra with increasing pump intensity, normalized to pump intensity, illustrating the transition from spontaneous emission to stimulated emission and lasing. (d) Monolayer WS_2 photoluminescence background and cavity emissions as a function of pump intensity. Dashed lines represent linear fits to the experimental data. The WS_2 photoluminescence background emission shows a linear dependence on the pump intensity, and the green dashed lines (cavity emission) show a kink indicating the onset of superlinear emission and lasing operation. (e) FWHM versus input pump intensity. Linewidth narrowing of the lasing mode is observed as the excitation intensity exceeds the lasing threshold. The red dashed line is a guide to the eye. Figure and caption reproduced from Ref. [15].

compared to the linear behavior of the background emission. A β -factor of 0.5 was determined from the fit shown in Figure 1.2(b). The corresponding threshold analysis indicates a threshold value of around $5\text{--}8 \text{ MW cm}^{-2}$. The linewidth of the lasing mode was shown to narrow from 0.28 to 0.24 nm at threshold (Figure 1.2(e)).

1.2.3 Molybdenum Disulfide Microdisk

Also in 2015, Salehzadeh et al. [12] presented the first room temperature laser based on MoS₂. Four-layer MoS₂ was placed on a freestanding SiO_x microdisk cavity, illustrated in Figure 1.3(a). The four-layer MoS₂ was treated with an O₂ plasma [16], resulting in an increased PL intensity due to the decoupling of electronic states in individual layers. Using multilayer TMDs affords a higher optical confinement factor compared to a monolayer. The device was optically characterized at room temperature using a micro-PL setup with a 514 nm cw pump laser, using a silica microsphere to facilitate coupling (Figure 1.3(a)). At low pump power, below threshold, the characteristic WGM spectrum can be seen weakly superimposed on the PL background Figure 1.3(b). At higher pump powers, above threshold, the WGMs are enhanced by a factor of 20 whereas the background PL is only enhanced by a factor 2. Polarization dependent measurements were carried out showing that the observed modes were TE-polarized. Around the lasing threshold, a linewidth narrowing of the TE₅₂¹ mode from 0.36 ± 0.02 to 0.26 ± 0.02 nm was observed together with an abrupt change in slope of the L-L curve. The Q factor of the WGMs was measured to be in the range of 2600-3300. The threshold power was estimated to be $20 \mu\text{W}$ Figure 1.3(c). The threshold pump power density was not reported.

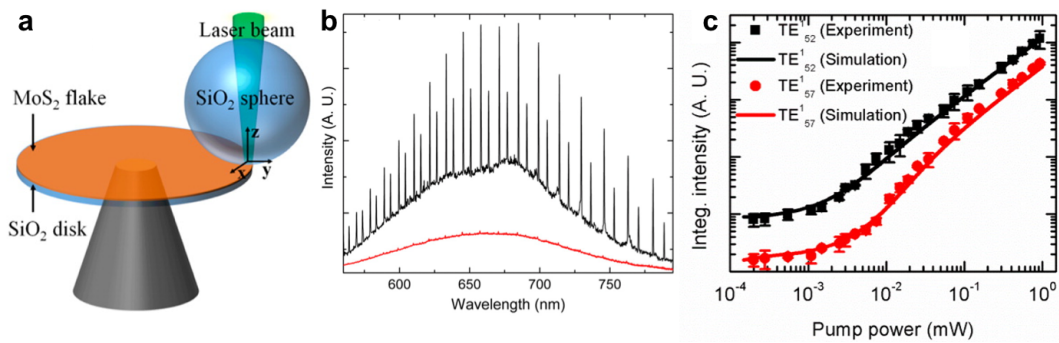


Figure 1.3: (a) Schematic configuration of the coupled microsphere/microdisk optical cavity with the incorporation of 2D MoS₂. (b) RT-micro-PL spectra of the laser device with an excitation power of $3 \mu\text{W}$ (lower spectrum) and $30 \mu\text{W}$ (upper spectrum). (c) L-L plot of the integrated intensity as a function of excitation power. Figure and caption reproduced from Ref. [12].

1.2.4 Molybdenum Ditelluride Nanowire

Correspondingly, the first silicon-compatible TMD light emitter was presented by Li et al. [17] using a monolayer of MoTe_2 on a 1D silicon photonic crystal nanobeam cavity as illustrated in Figure 1.4(b). Monolayer MoTe_2 has a bandgap around 1.72 eV but an excitonic photoluminescence emission peak exists at 1.1 eV, just below the bandgap of silicon. Silicon is only weakly absorbing at 1.1 eV, so transparent enough to support cavity modes of sufficiently high quality factor. The team measured their devices at room temperature pumping with 633 nm and obtained the spectra shown in Figure 1.4(c).

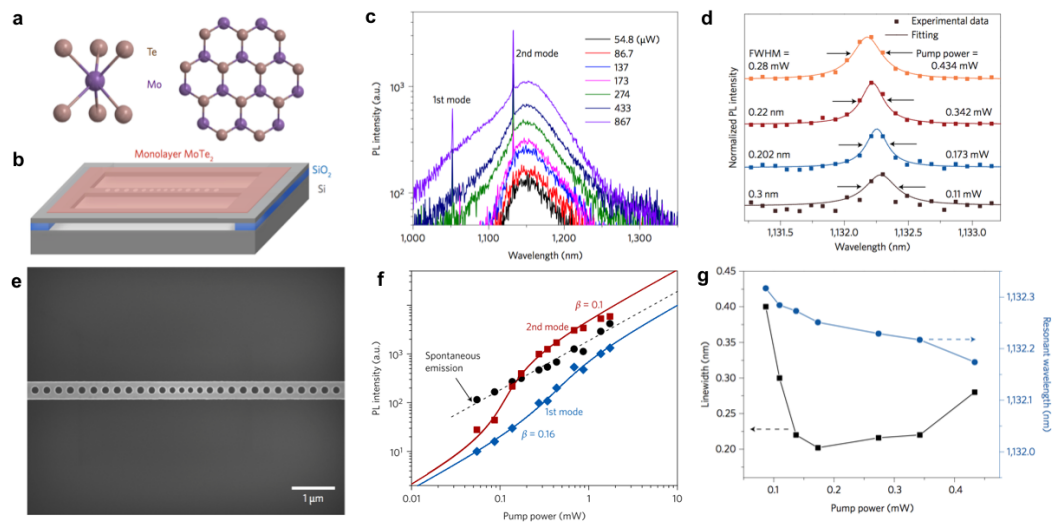


Figure 1.4: (a) Crystal structure of MoTe_2 (2H). (b) Device schematic (silicon photonic crystal nanobeam laser structure suspended in air with a monolayer of MoTe_2 on top). (c) PL spectra of the nanobeam light emitter with increasing pump power levels at room temperature. (d) Fitting of the PL spectra for different pump levels. Solid squares represent the measured data points. The lines represent Lorentzian fits. (e) SEM of an undercut silicon nanobeam cavity. (f) Log-log plot of light in versus light out for the first two modes and for a background spontaneous emission. The solid squares represent data from experimental measurements, and the solid line is a rate-equation fitting. (g) Linewidth (black) and resonant wavelength (blue), with arrows pointing to their respective axes, versus pump power. Figure and caption reproduced from Ref. [17].

The first lasing mode at 1052 nm has a significantly larger threshold of 0.426 mW compared to the 2nd mode at 1132 nm, because it experiences higher absorption from the silicon due to its shorter wavelength as well as less gain,

being further away from the gain peak. The spontaneous emission exhibits a linear response to increasing pump power compared to the nonlinear behavior of the lasing modes shown in the L-L curves in Figure 1.4(f). The linewidth of the 2nd mode at 1132 nm was measured to be 0.202 nm at 172 μW pumping power corresponding to a Q factor of 5603. This is the highest Q factor of any TMD laser demonstrated so far. The β -factor of 0.1 was deduced from fitting the laser rate equations. The threshold was determined from Figure 1.4(f) to be 0.097 mW corresponding to a pump density of 6.6 W cm^{-2} , although the authors used a very nonstandard method to obtain this pump density data. Applying standard methods, i.e., calculating the incident power density directly on the gain materials without taking absorption and coupling coefficients into account, based on the information given in the paper, we determined the pump threshold to be $\approx 2.1 \text{ kW cm}^{-2}$. We also note that Figure 1.4(g) plots a factor 2 reduction in the emission linewidth at threshold, although the spectrum that would support a factor 2 narrowing is not shown in Figure 1.4(d).

1.2.5 Summary

We have described a number of representative examples of microcavity light emitters based on 2D-TMD materials reported in the literature, all of which claim lasing action based on a careful analysis of the light input-output curve, demonstrating the characteristic “kink” in the curve that is traditionally seen as evidence for lasing. In Section 2.3 the conditions required for lasing will be discussed with particular emphasis on microcavity lasers.

2 Theory

In this section, we will discuss the background theory underpinning this thesis. First we will examine photonic crystals, then move on to two dimensional dichalcogenides and conclude with an analysis of lasing from microcavity emitters.

2.1 Photonic Crystals

2.1.1 The Electromagnetic Wave Equation

The following section has been partially adapted from [18]. We begin with Maxwell's equations and then describe a photonic bandgap in a 1D photonic crystal. We consider an isotropic material with electric permittivity ϵ and magnetic permeability μ that are scalar quantities. We also assume that our material is non-magnetic therefore $\mu = \mu_0$ (vacuum permeability) and non-electric (both the charge density and electrical conductivity are zero). With these assumptions, the Maxwell equations can be written as:

$$\nabla \cdot \mathbf{E} = 0 \tag{2.1}$$

$$\nabla \times \mathbf{E} = -\frac{\partial \mathbf{B}}{\partial t} \tag{2.2}$$

$$\nabla \cdot \mathbf{B} = 0 \tag{2.3}$$

$$\nabla \times \mathbf{B} = \mu_0 \epsilon \frac{\partial \mathbf{E}}{\partial t} \tag{2.4}$$

where \mathbf{B} and \mathbf{H} are the vector electric and magnetic fields, respectively, and ϵ is the vacuum permittivity ϵ_0 multiplied by the dielectric function $\epsilon(r)$. We start by

taking the curl of Equation 2.2:

$$\nabla \times (\nabla \times \mathbf{E}) = -\frac{\partial}{\partial t} \nabla \times \mathbf{B} = -\mu_0 \epsilon \frac{\partial^2 \mathbf{E}}{\partial t^2} \quad (2.5)$$

Then using the vector identities (where \mathbf{V} is any vector function of space):

$$\nabla \times (\nabla \times \mathbf{V}) = \nabla(\nabla \cdot \mathbf{V}) - \nabla^2 \mathbf{V} \quad (2.6)$$

$$\nabla^2 \mathbf{V} = \nabla \cdot (\nabla \mathbf{V}) \quad (2.7)$$

and using Equations 2.1 and 2.3 we obtain the fundamental electric wave equation:

$$\nabla^2 \mathbf{E} = \mu_0 \epsilon \frac{\partial^2 \mathbf{E}}{\partial t^2} \quad (2.8)$$

Similarly, the magnetic wave equation is:

$$\nabla^2 \mathbf{B} = \mu_0 \epsilon \frac{\partial^2 \mathbf{B}}{\partial t^2} \quad (2.9)$$

The solutions to these equations are of a harmonic nature in the form of a mode profile times a complex exponential, therefore light propagates as a wave.

$$\mathbf{E}(\mathbf{r}, t) = \mathbf{E}(\mathbf{r}) e^{-i\omega t} \quad (2.10)$$

$$\mathbf{B}(\mathbf{r}, t) = \mathbf{B}(\mathbf{r}) e^{-i\omega t} \quad (2.11)$$

2.1.2 Light Propagating in Free Space

Propagation of the plane wave in free space is governed by the optical frequency ω and the wave vector \mathbf{k} . The direction of the propagating wave is determined by the direction of \mathbf{k} and the phase velocity of the wave is determined by $v_\phi = \omega/k$. The optical frequency and wave vector are linked together by the dispersion relation:

$$\omega = k \frac{c}{n} \quad (2.12)$$

where c is the speed of light in free space and n is the refractive index of the dielectric medium in which the light is propagating. In an isotropic medium, the dispersion relation is independent of the propagation direction and so there is only one possible wave vector k for each frequency ω . This can be described by a

straight line $\omega = kc/n$ in the dispersion diagram (ω vs k) and this is often referred to as the light line.

2.1.3 Waveguides

Light incident on an interface between two homogeneous media can be reflected (Fresnel's formula) or refracted (Snell's law). Typically both occur, except for the case of total internal reflection. If we consider light incident on an interface with a higher refractive index $n_1 > n_2$, as we increase the angle of incidence θ_1 the angle of refraction θ_2 also increases to the point where $\theta_2 = 90^\circ$. This angle of incidence is known as the critical angle of incidence where $\theta_c = \sin^{-1}(n_2/n_1)$. For angles of incidence higher than the critical angle $\theta_i > \theta_c$, all the light is reflected back into the medium, and hence, is totally internally reflected. When light is totally internally reflected there is no change in the amplitude of the propagating wave, however, there is a phase change that is dependent on the angle of incidence θ_1 and the polarization of the incident light. The phase change relation is given by the Fresnel equations:

$$R_{TE} = \frac{\tan(\theta_1 - \theta_2)}{\tan(\theta_1 + \theta_2)} = e^{i\phi^{TE}} \quad (2.13)$$

$$R_{TM} = -\frac{\sin(\theta_1 - \theta_2)}{\sin(\theta_1 + \theta_2)} = e^{i\phi^{TM}} \quad (2.14)$$

where R is the reflectivity coefficient and $\phi^{TE/TM}$ is the phase shift for the TE and TM polarization.

2.1.3.1 Planar Waveguides

A planar dielectric waveguide is a slab of dielectric material (core) that has a thickness d in the x -direction and is isotropic in the y and z -directions. This slab is surrounded on the top and bottom by a lower refractive index material (cladding) illustrated in Figure 2.1(a). Light that propagates at angles higher than the critical angle θ_c is totally internally reflected at the core cladding interfaces. However, as light cannot be guided at any arbitrary angle $\theta > \theta_c$, it is also necessary that after two reflections the reflected wave interferes constructively with the original

wave to allow propagation in the waveguide. This is known as the self-consistency condition and is illustrated schematically in Figure 2.1(a). For a simple step index waveguide, the self-consistency condition can be written as:

$$\underbrace{\frac{2\pi}{\lambda_0} 2d \sin \theta_m^{TE/TM}}_{\text{propagation}} - \underbrace{2\phi^{TE/TM}}_{\text{reflection}} = 2\pi m \quad (2.15)$$

where $m = 0, 1, 2, \dots, N$, d is the slab thickness, and λ_0 is the vacuum wavelength. The angle $\theta_m^{TE/TM}$ defines the wave vector components in the direction of propagation and the propagation constant $\beta_m^{TE/TM} = n_2 k_0 \cos \theta_m^{TE/TM}$. The propagation constant is different for TE and TM modes due to the polarization dependence of the phase shift term ϕ . The frequency dependence of the

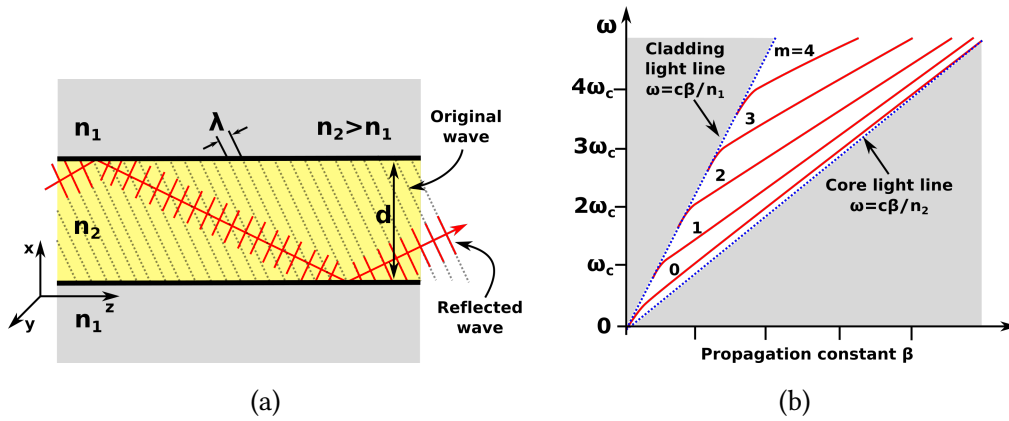


Figure 2.1: (a) A schematic diagram of the self-consistency condition for a planar waveguide. (b) A dispersion diagram for the TE modes of a planar waveguide.

propagation constant gives the dispersion diagram (Figure 2.1(b)). For a symmetric slab waveguide, the fundamental mode $m = 0$ is always supported and higher order modes are supported above their cutoff frequencies ω_c . Above the cutoff frequency, the propagation constant increases from $n_1 k_0$ towards $n_2 k_0$ as the light becomes more confined in the high-index medium. The dispersion curves of the guided modes are bounded by the core and cladding light lines. For frequencies higher than the cladding light line, the total internal reflection condition is not satisfied and hence light refracts into the cladding. These are known as leaky modes and can cause high propagation losses. However, leaky modes can be useful for coupling light into waveguides.

2.1.3.2 2D Waveguides

In planar waveguides, light is only confined in the vertical direction by the refractive index contrast in the slab and diverges within the plane of the slab. Two-dimensional waveguides allow light to be confined in both the x and y -directions. The physics that governs 2D waveguides is analogous to the planar waveguide, only more complex mathematically. For 2D waveguides the polarization of the guided mode is no longer purely TE or TM, but quasi-TE and quasi-TM. When there are bends in the waveguide or the cladding top and bottom are asymmetric, the quasi-TE and quasi-TM modes can interact causing cross talk between the two.

A common type of waveguide used in integrated photonics is a nanowire waveguide which is fabricated on Silicon-on-Insulator (SOI) wafers, see Figure 2.2(a). Trenches either side of the nanowire are etched through the top device layer of SOI, leaving a 500×220 nm cross-section waveguide bounded by air on the top and the sides and by silica underneath. These dimensions are chosen to guide a single quasi-TE mode in SOI with a silicon layer thickness of 220 nm. The waveguide modes were simulated using EIMS (Effective Index Mode Solver) [19]. EIMS is a 2D multilayer waveguide mode solver that calculates the propagation constant and effective index of guided modes. The calculated mode field profiles were overlaid on the schematic diagrams in Figure 2.2.

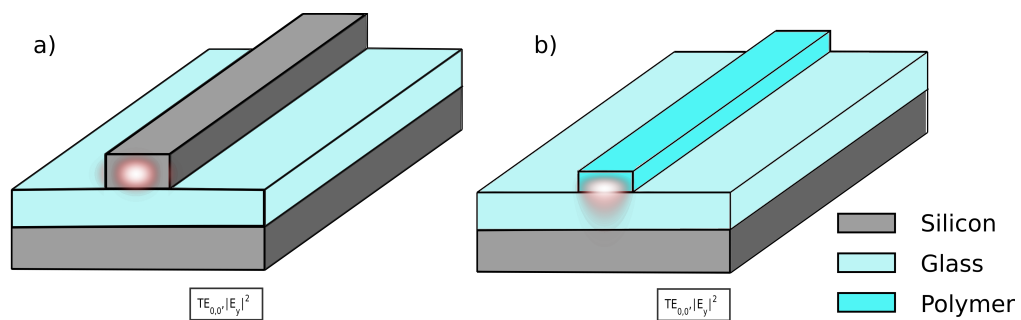


Figure 2.2: (a) A schematic of a silicon nanowire waveguide on SOI substrate. (b) A schematic of a polymer strip-loaded waveguide on thermal oxide on silicon wafer. The electric field profiles $TE_{0,0}, |E_y|^2$ were simulated using EIMS [19] and overlaid onto a schematic diagram.

Another type of waveguide that is relevant to this thesis is the strip-loaded waveguide, where a thin layer of high refractive index material is deposited on a

lower index material, see Figure 2.2(b). The influence of the high index strip guides the light, however, the majority of the optical mode overlaps with the low index substrate which is beneficial for producing waveguide amplifiers.

2.1.4 1D Photonic Crystal Band Gap

The simplest photonic crystal consists of alternating layers of materials with different dielectric constants. These layers are finite in the z -direction and infinite in the xy -plane. Lord Rayleigh first published an optical analysis of such a system in 1887 [20], so light propagation in a periodic system is not at all a new concept; what is relatively new is the extension of this concept to 2 and 3 dimensions, as we will see later. Since the layer stack is periodic in the z -direction, we can consider the periodic dielectric function as $\epsilon(z) = \epsilon(z+la)$ where l is an integer and a is the lattice vector. The wave propagating through the layer structure in the z -direction has a wave vector, k_z . As we are dealing with a periodic structure, we can apply the Bloch theorem. The Bloch theorem states that for a system that is periodic in k -space, the solution at point z must equal that of a point an integer number of lattice vectors away $z+la$.

$$\mathbf{E}(z) = u_{k_z}(z)e^{-ik_z z} \quad (2.16)$$

where \mathbf{E} is the electric field vector with wave vector \mathbf{k}_z and u_{k_z} the periodic function with the lattice vector a .

$$u_{k_z}(z) = u_{k_z}(z+R) \quad (2.17)$$

where $R = la$ which is an integer multiple of the lattice period. The Bloch theorem can be expressed in the alternate form by combining Equation 2.16 and Equation 2.17:

$$\mathbf{E}(z+R) = \mathbf{E}(z)e^{-ik_z R} \quad (2.18)$$

The Bloch mode with wave vector \mathbf{k}_z is identical to the Bloch mode with wave vector $\mathbf{k}_z + l(2\pi/a)$. We will now consider waves that propagate only in the z -direction crossing each dielectric interface at normal incidence. If we consider the case where $n_1 = n_2$, i.e. a homogeneous medium, then $\omega = ck$ which is represented by the solid blue lines in Figure 2.3(b). The dispersion relation replicates itself every $k_z = k_g$, where $k_g = 2\pi/a$ is the reciprocal lattice vector. At

each crossing point of the dispersion lines at $k = \pm\pi/a$ the solution is degenerate. By changing the refractive index of the two layers such that $n_1 \neq n_2$, the degeneracy is lifted allowing for two different values of ω for the same \mathbf{k}_z . Due to the periodicity of the structure and by simple symmetry arguments, to arrange the modes in the structure, the nodes of each mode must lie at the center of either the high or low index regions. In analogy to solid-state physics, the high-index region can be considered equivalent to the lower potential. Therefore, the lower frequency mode (ω^-) preferentially occupies the high index region and, conversely, the higher frequency mode (ω^+) occupies the low-index region as shown in Figure 2.3(a). Consequently, there are a range frequencies where no modes can exist, called the photonic band gap, highlighted by the yellow band in Figure 2.3(b). When light with a frequency within the photonic band gap of the structure is incident on the structure, it is reflected as there are no allowed modes into which the light can couple. The size of this photonic band gap is proportional to the refractive index contrast.

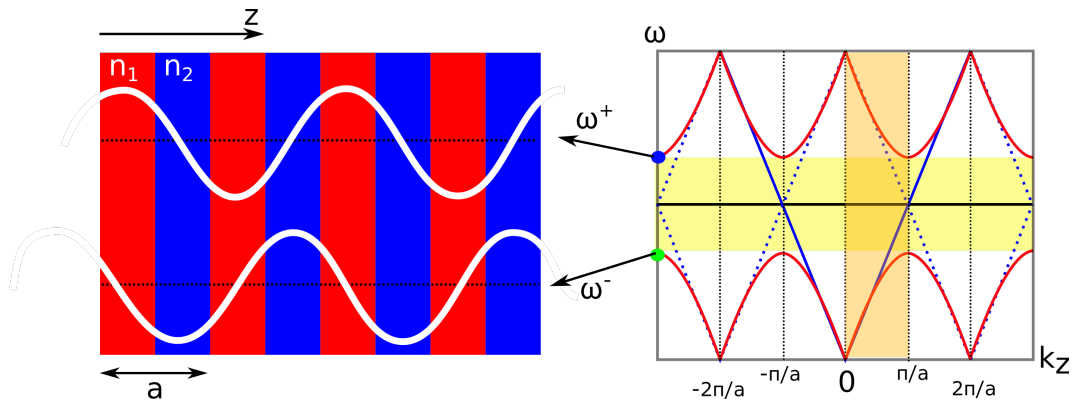


Figure 2.3: Schematic diagram of (Left) 1D periodic dielectric stack, in the z -direction with high (n_2) and low (n_1) refractive indices. The field intensity of the two standing wave solutions is shown upper wave (ω^+) and lower wave (ω^-). (Right) Band diagram of the 1D dielectric stack shown on the left. The band gap is highlighted in yellow and the irreducible Brillouin zone is highlighted in orange. Figure adapted from [18].

2.1.5 2D Photonic Crystal Band Gap

The concept of the 1D photonic crystal can be extended to two dimensions. Two dimensional photonic crystals are periodic within the xy -plane and homogeneous in the z -direction. The physics that governs 2D photonic crystals

is broadly the same as in 1D, so the concepts of Bloch modes and band structures similarly apply. The added dimension adds interest and complexity to the band structure. The most common two dimensional photonic crystal lattices are the square and triangular lattices. These lattices are defined by a pair of lattice vectors \mathbf{a}_1 and \mathbf{a}_2 . Since 2D photonic crystals are not isotropic, the dispersion diagram needs to be specified in all possible propagation directions. Figure 2.4 shows the dispersion relation for a photonic crystal with a triangular lattice plotted along the 3 possible dispersion paths: $\Gamma - K$, $\Gamma - M$, and $M - K$. A photonic band gap then opens up for TE polarized light at both K and M symmetry points. For the range of frequencies that the two band gaps overlap, highlighted in yellow, light is forbidden to propagate in any direction. Note that this band gap is polarization sensitive, i.e. it only applies for the TE mode (the in-plane E-field). The orthogonal TM mode does not exhibit a band gap for this structure. Structures with dielectric bulk and air holes favour opening a TE band gap, whereas, dielectric pillars in air favour a TM band gap. Other lattice geometries can be carefully engineered to provide a band gap for both TE and TM polarizations. Another parameter that is important to 2D photonic crystals is the filling fraction of the air holes. While in the 1D case any refractive index contrast is sufficient to produce a photonic band gap, for the 2D case the filling fraction (i.e. the fraction of the total surface area that the air hole occupies) and the refractive index contrast are the crucial parameters. There is only a limited range of filling fractions available that open up a complete band gap for 2D photonic crystals. TM photonic band gaps can be opened when there are isolated islands of high-index material (rods of high-index in air), whereas, a TE bandgap is opened when there is a connected network of high-index material (air-holes in high-index materials). A TE and TM band gap can be achieved in a triangular lattice of air holes in silicon through using a sufficiently large air hole radius that causes the spots between the air holes to act like isolated islands of high index material connected by thin veins [18].

2.1.5.1 2D Photonic Crystal Slab

The fact that 2D photonic crystals are homogeneous in the z -direction limits their applications to photonic crystal fibers (2D photonic crystals with radial symmetry). In integrated optics, photonic crystal slabs are widely used. Here, confinement in the vertical direction is provided by total internal reflection while

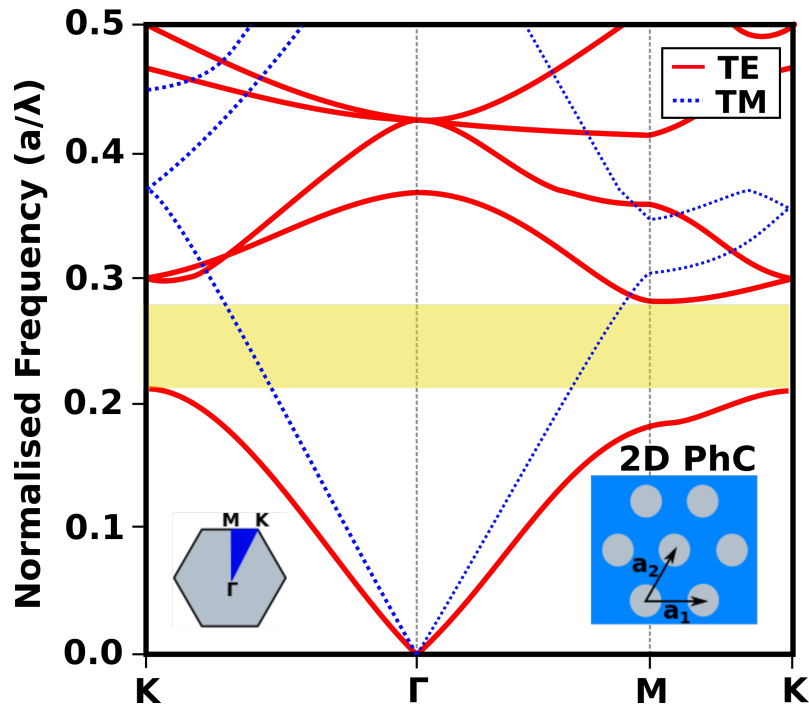


Figure 2.4: Band-diagram of a two-dimensional photonic crystal (infinite in z -direction) ($n_1 = 3.5$) with hexagonal array of air holes ($n_2 = 1, r/a = 0.35$), as shown in the right inset. The directions of the wavevector are shown in the left inset with specific points corresponding to the graph. The red lines show the bands with the electric field in-plane (TE modes). The dashed blue lines show the bands with the electric field out of plane (TM modes). Mode calculations performed by Dr Bryan J O'Regan.

confinement in-plane is provided by the photonic crystal lattice. Silicon-on-insulator (SOI) is the preferred substrate for silicon photonic crystal slabs. SOI consists of a 220 nm thick crystalline silicon "device" layer on top of thermally grown silica with a regular silicon carrier wafer underneath. SOI can yield a suspended membrane structure when the silica is under-etched.

Figure 2.5 shows the band diagram for a membraned photonic crystal slab in SOI. Comparing the band diagram to that of the 2D photonic crystal (Figure 2.4), the shape of the dispersion curves are similar. However, the curves of the photonic crystal slab are stretched in frequency due to the confinement of the mode in the vertical direction which lowers the average refractive index. All modes which lie above the light line experience high propagation losses as they are able to radiate out of plane. This leaky region is shaded in grey in Figure 2.5.

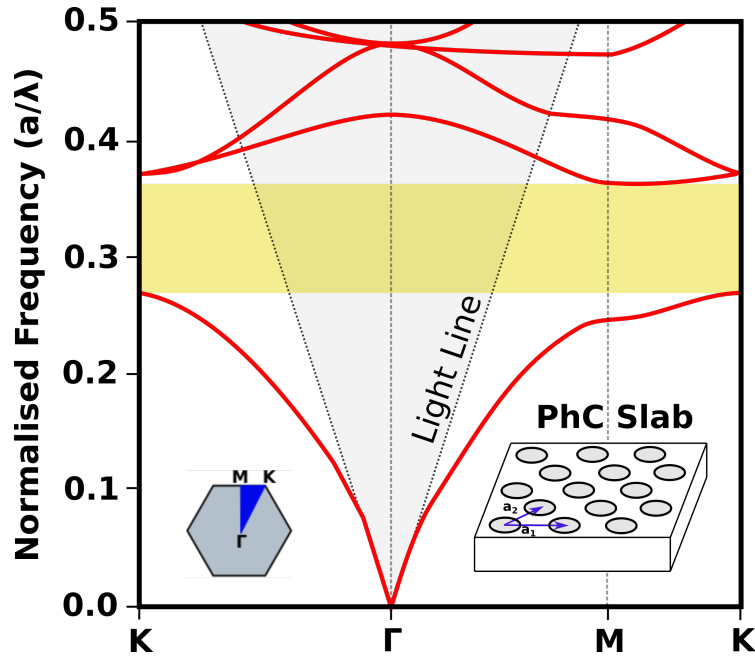


Figure 2.5: Band-diagram of a two-dimensional photonic crystal slab (220 nm z -direction) ($n_1 = 3.5$) with hexagonal array of air holes ($n_2 = 1, r/a = 0.35$), as shown in the right inset. The directions of wavevector are shown in the left inset with specific points corresponding to the graph. The red lines show the bands with the electric field in-plane (TE modes). The light lines are shown with dashed lines and the leaky region is highlighted in grey. Mode calculations performed by Dr Bryan J O'Regan.

2.1.6 Defects in 2D Photonic Crystal Slabs

The propagation of light in the photonic crystal slab can be affected by any irregularities in the crystal structure. Light can either be scattered or localized to any defects in the structure. In the case where light is localized, defect states are introduced into the band structure. If the defect state is found within the photonic band gap, the field remains localized to the defect location and exponentially decays into the bulk photonic crystal. Just as in solid-state physics, these defects can be classified by their dimensionality as 0-dimensional (point defects) or 1-dimensional (line defects). The confinement of light into small mode volumes (Q/V) increases light matter interaction and can lead to non-linear optical effects.

2.1.6.1 2D Photonic Crystal Cavities

The most common type of cavity is formed by a line defect whereby a line of n holes is removed from the lattice; this configuration is referred to as the L_n -type photonic crystal cavity. Typically, odd numbers are chosen, such that the L_3 cavity is formed by removing a line of 3 holes, the L_5 cavity by removing 5 holes and so on. These L_n -type cavities are illustrated in Figure 2.6. For cavities with a line of ≥ 3 holes removed, the nanocavity can be described by a simple Fabry-Perot resonator model in which the fundamental mode of a photonic crystal waveguide is confined by 2 photonic crystal mirrors [21]. The parameters that define the cavity are the reflectivity of the photonic crystal mirrors, the cavity length and the group index of the Bloch mode. For L_3 and larger cavities, more than one mode is supported, and the number of supported modes increases with cavity length. The lowest frequency mode supported by the cavity is the fundamental mode and usually possesses the highest quality factor (Q-factor). The quality factor of the

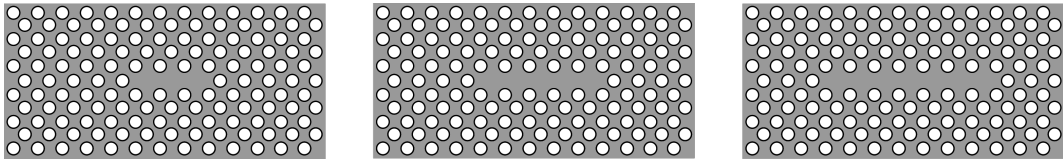


Figure 2.6: L_n -type photonic crystal cavities. Left to right: L_3 , L_5 , and L_7 photonic crystal cavities.

cavity is defined as:

$$Q = 2\pi \frac{\text{Energy stored}}{\text{Energy dissipated per cycle}} \quad (2.19)$$

however to experimentally measure the Q-factor we are interested in the lineshape and linewidth of the resonance spectrally. The cavity resonance has a Lorentzian lineshape centered at ω_0 with a linewidth $\Delta\omega$ which is the full-width at half-maximum of the Lorentzian [22]. These quantities are related to the Q-factor by:

$$Q = \frac{\omega_0}{\Delta\omega} \quad (2.20)$$

Light-matter interaction is enhanced in high-Q, low mode volume cavities by the Purcell factor (F_p) (Equation 2.21). The Purcell effect [23] is based upon Fermi's golden rule and it states that the transition rate between states is proportional to the density of final states. Due to the small volume of the L_3 cavity, the density of

these states is enhanced. By enclosing an emitter in a cavity, spontaneous emission can therefore be enhanced. Purcell enhancement is only possible when the emitter linewidth is comparable to or smaller than the linewidth of the cavity resonance [24]. For emitters with a larger linewidth than the cavity (the "bad emitter" regime), the enhancement of spontaneous emission is dominated by the emitter linewidth and a large spontaneous emission coupling factor, referred to as the β -factor, is not achievable [25]. The Purcell factor is given by:

$$F_p = \frac{3}{4\pi^2} \left(\frac{\lambda_{free}}{n} \right)^3 \left(\frac{Q}{V} \right) \quad (2.21)$$

where (λ_{free}/n) is the wavelength of light in material with refractive index n , Q is the Q-factor, and V is the mode volume.

2.1.7 Q-factor Optimization of 2D Photonic Crystal Cavities

In the process of trying to achieve high Q-factors in Ln-type photonic crystal cavities, the group of Prof. S. Noda [26] found that by altering the size and position of the holes adjacent to the cavity in the $\Gamma - K$ direction, a dramatic increase in Q-factor was observed. When investigating how to explain the phenomenon, they considered how the light was being confined in the cavity. With no adjustments, the light is confined in the cavity like a Fabry-Perot resonator with perfectly reflecting mirrors. However, with the shifted and reduced radius holes, the light was able to penetrate deeper into the photonic crystal mirrors, so experienced a gentler transition; they named this phenomenon "gentle confinement". One can also think of it as analogous to impedance matching in RF/AC circuits. The gentle confinement hole shifts are shown in Figure 2.7.

Considering a Fabry-Perot cavity, the electric field in the cavity is a standing wave within a top-hat envelope function as illustrated in Figure 2.8(a). For the case of gentle confinement, the envelope function is a Gaussian as illustrated in Figure 2.8(b).

We can now take the Fourier transform of the envelope functions, yielding a sinc function at $k = \pm 2\pi/\lambda$ for the top-hat and a delta function at $k = \pm 2\pi/\lambda$ for

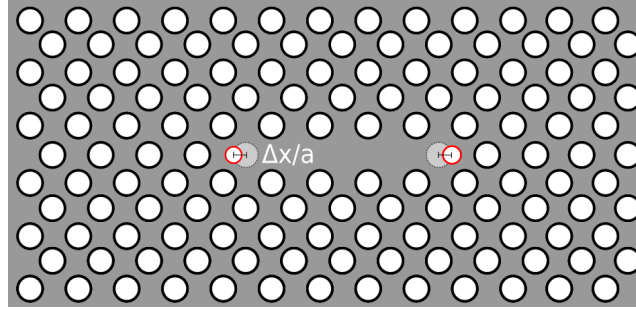


Figure 2.7: Schematic of the gentle confinement L3 cavity. The holes in red are shifted away from the cavity by $\Delta x/a$ and have radius r' .

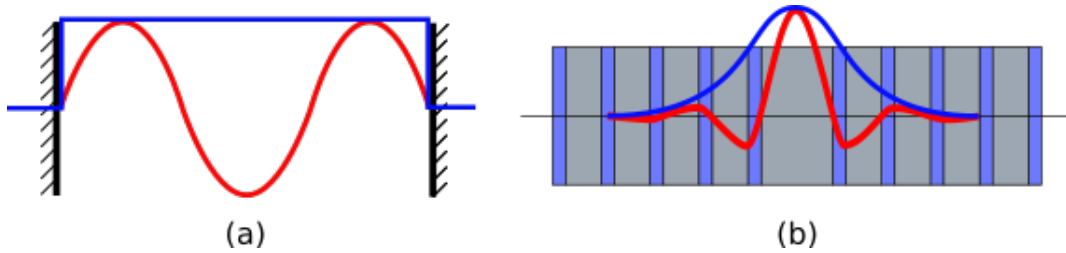


Figure 2.8: (a) Schematic diagram of a standing wave within a perfectly reflecting Fabry-Perot cavity, the square envelope function is in blue. (b) Schematic of a standing wave in a distributed Bragg reflector with a defect. This is similar to the gentle confinement case. The Gaussian envelope curve is in blue.

the Gaussian. The Fourier transforms are plotted in k -space, Figure 2.9(c) & (d), with the position of the leaky region highlighted in blue. We can see that there is a significant proportion of the electric field that overlaps with the leaky region for the top-hat case causing loss of energy from the cavity. Whereas, for the gentle confinement, the electric field overlap with the leaky region is minimized reducing energy loss and therefore increasing the Q -factor of the cavity.

We can now consider the L3 cavity as opposed to a simplified Fabry-Perot model and take the 2D Fourier transform of the electric field profile (E_y) for the fundamental mode, illustrated in Figure 2.10. We can see the electric field profiles in real space in subplots (a) & (c) and in k -space in subplots (b) & (d). The leaky region, i.e. the light cone, is plotted as a circle. As with the 1D case, there is significant overlap of the electric field with the light cone for the standard L3 cavity, while the overlap is minimized for the gentle confinement geometry. Further work from this Q -factor optimization realized photonic crystal nanocavities with Q -factors of up to 9,000,000 [27].

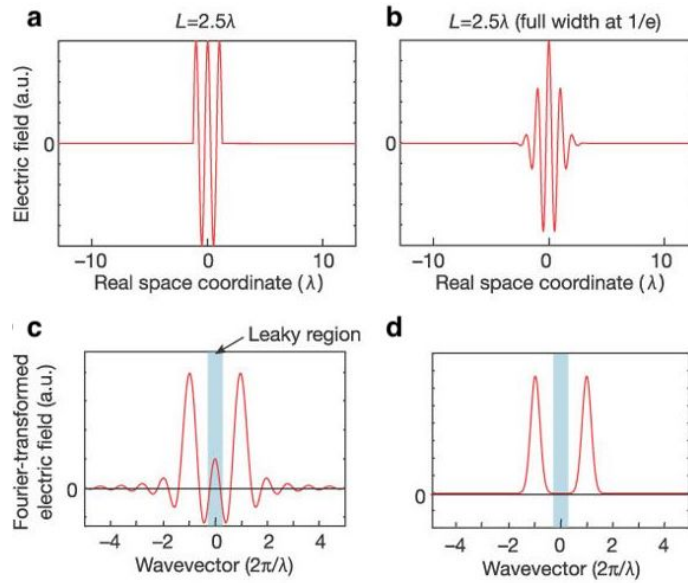


Figure 2.9: (a) & (b) The electric field profile inside a cavity with a very short (2.5λ) length, and the spatial FT spectra. The leaky region is indicated as a blue area. (c) & (d) The electric field profile with a gentle envelope function (Gaussian curve) and its spatial FT spectrum. Reproduced from [26].

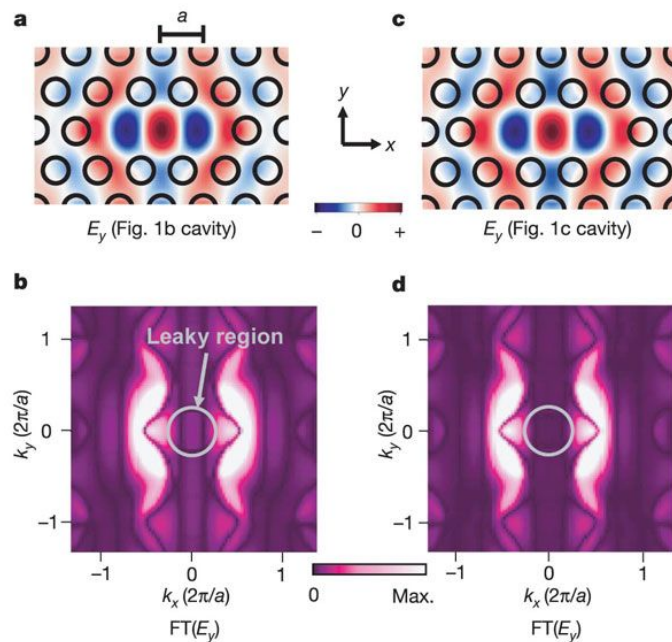


Figure 2.10: (a) The electric field profile (E_y) of the fundamental mode of photonic crystal cavity. (b) The FT spectra of (a). The region inside the grey circle corresponds to the leaky region. (c) & (d) The electric field profile and 2D FT spectrum, respectively, for the L3 cavity. Figure and caption reproduced from Ref. [26].

2.1.8 Farfield Optimization of 2D Photonic Crystal Cavities

In the previous section, we looked to optimize the light storage within the cavity to increase the Q-factor of the cavity. Not only is the Q-factor important for devices, but we need a mechanism to out-couple light vertically from the cavity whilst maintaining high Q-factors. This apparently conflicting requirement can be met by implementing the "far-field optimization" technique that was developed by Portalupi et al. [28]. The technique superimposes a second-order grating onto the photonic crystal cavity by enlarging/reducing the size of surrounding holes, see Figure 2.11(a).

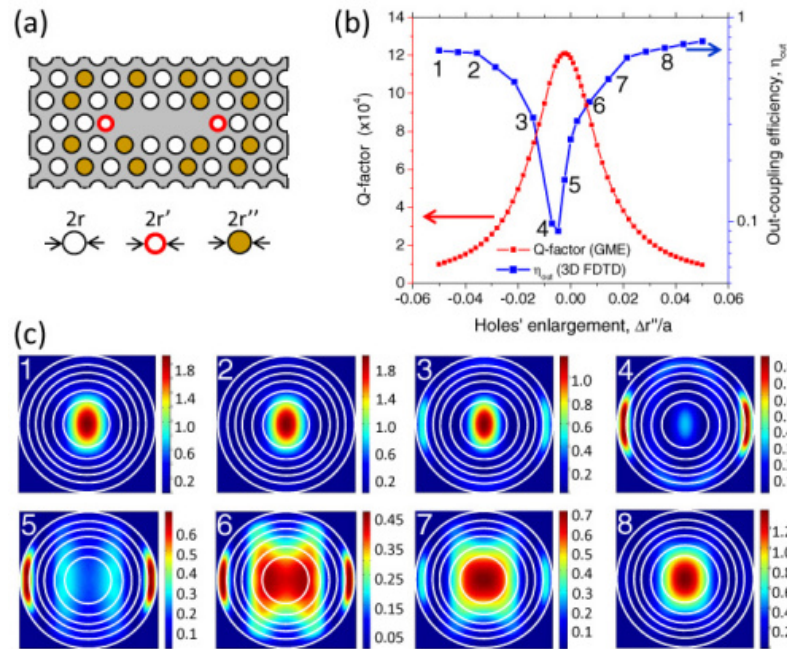


Figure 2.11: (a) Schematic of far-field optimized L3 PhCC. Holes with red edge are shrunk and shifted to optimize the Q-factor. Dark holes are modified to increase the vertical out-coupling. (b) Calculated Q-factor and out-coupling efficiency (η_{out}) as a function of radius variation of the alternating holes highlighted in yellow. (c) A selection of calculated far-field patterns (electric field intensity profile, $|E|^2$) corresponding to the labeled numbers on the efficiency plot (see numbers in panel (b)). Field intensities are normalized to the total emitted power in the vertical half-space. Concentric circles correspond to $\theta = 20^\circ, 30^\circ, 40^\circ, 50^\circ, 60^\circ, 90^\circ$ from the inner to the outer one, respectively. Figure and caption reproduced from Ref. [28].

The second-order grating acts to fold some of the k-vectors outside of the light cone back into the light cone for extraction. As the modified hole radius

is controllable, a compromise can be made to increase the out-coupling efficiency of the cavity whilst maintaining high Q-factors. The Q-factor and out-coupling efficiency are plotted as a function of hole enlargement in Figure 2.11(b). The figure highlights that a good compromise can be achieved, e.g. at points 3 and 6, where the light out-coupling efficiency can be increased by an order of magnitude while the Q-factor is reduced by $< 20\%$. Another practical consideration is the angular emission profile of the cavity. For applications where a long working distance objective is desirable, for example if the measurement is to be performed in a cryostat, emission profile 3 in Figure 2.11 may be preferable as the emission can be collected by a low NA objective.

2.2 2D Materials

Interest in atomically thin materials was sparked by the discovery of graphene by Novoselov and Geim in 2004 [29] and their 2010 Nobel prize. In the wake of this achievement, a number of techniques for producing monolayers, such as mechanical exfoliation [29] and CVD growth [30], were developed. These techniques then opened the door for research into materials 'beyond graphene' to explore what other functionalities may be realised, and transition metal dichalcogenides (TMDs) came to the fore. While graphene offers excellent mobility for electronic applications [31], the TMDs offer very high exciton binding energies [32] which is advantageous in photonics. TMDs have the general formula MX_2 , where M is a transition metal and X is a chalcogen. Typical transition metals forming TMDs are Mo or W with the chalcogens being S, Se or Te. It has been known for a while that thin layers of TMDs feature direct bandgaps in the visible and near-IR region of the optical spectrum [33] in contrast to their indirect bandgaps observed in bulk, yet it took the graphene revolution to awaken this interest on a larger scale.

These direct bandgaps are found at the K and K' valleys of the reciprocal lattice (see Figure 2.12). The reason for the existence of two valleys at the K-point is that the inversion symmetry in the 2D Brillouin zone is broken by the alternate positioning of the transition metal and the chalcogen; hence the K point in each direction is different. The valleys are energy degenerate in momentum space; therefore, the interband transitions exhibit circular dichroism meaning that

different transitions are coupled to right or left hand circularly polarized light. For an optically generated electron to change valley, it either has to flip its spin or it has to undergo an energetically unfavorable transition; hence the electron is both valley and spin-polarized. These valley-specific selection rules have given rise to a new area of research, "valleytronics" [34], meaning that data could be stored or manipulated via different discrete values of the crystal momentum. At the K points, the spin degeneracy is lifted in both the conduction band (CB) and the valence band (VB), which is in contrast to, e.g., GaAs QWs where both CB and VB are spin degenerate. This spin-splitting effect gives rise to spin-allowed optically 'bright' transitions as well as spin-forbidden optically 'dark' transitions [35].

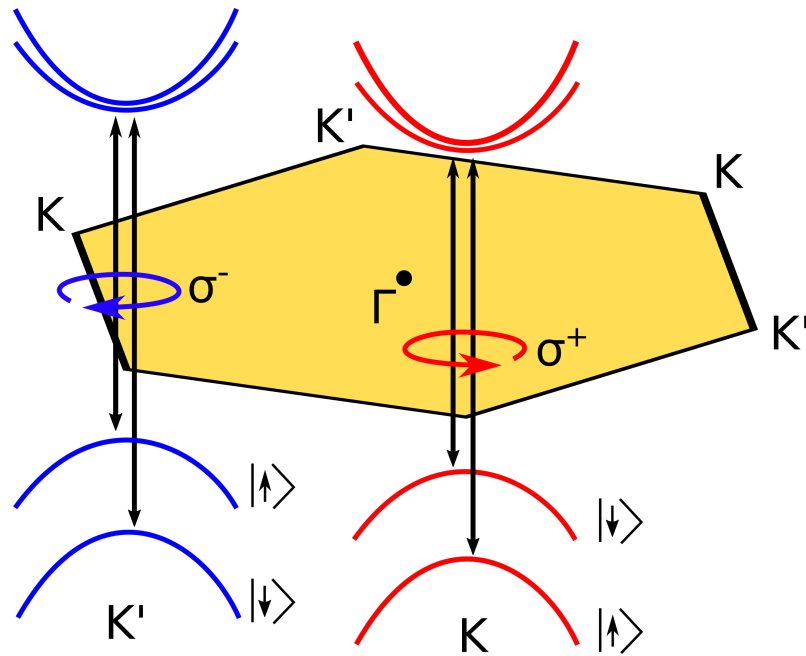


Figure 2.12: Schematic bandstructure of monolayer TMDs showing the circular dichroism and the K and K' valleys. The K and K' valleys are energy degenerate due to the inversion symmetry of the 2D Brillouin zone. The interband transitions at the K point are coupled to σ^+ circularly polarised light and at the K' point the interband transitions are coupled to σ^- circularly polarised light. These valley specific selection rules are the basis of valleytronics.

Light emission from TMDs is dominated by excitons and trions because of the strong Coulomb interactions inherent in the low dimensionality and the reduced dielectric screening compared to the bulk. These excitons (bound electron-hole pairs) have a very high binding energy (0.5-1 eV), which is one or two orders of magnitude higher than, e.g., that of GaAs quantum wells (QWs) [36]. The high

binding energy of the excitons leads to very short radiative decay rates on the order of 1 ps [37, 38], which is two orders of magnitude shorter than that of GaAs QWs. The transition metals and chalcogens can be combined almost arbitrarily within the MX_2 framework, and different combinations yield optical transitions of different energies, typically in the 1-2 eV range as illustrated in Figure 2.13.

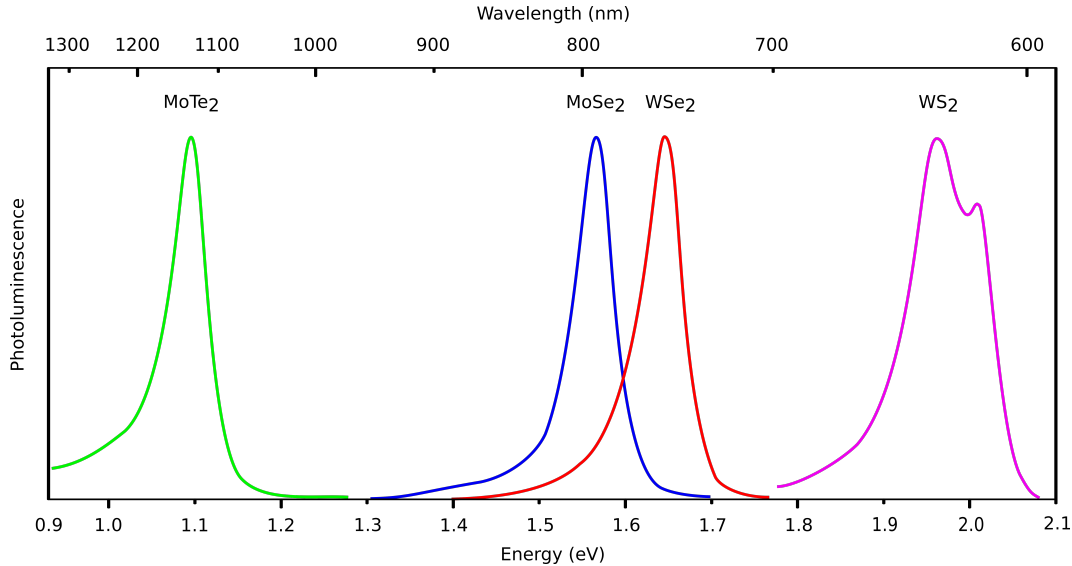


Figure 2.13: Photoluminescence (PL) spectra of a variety of monolayer TMDs at room temperature. The PL intensities are each normalized to unity for ease of comparison. Data is shown for MoTe₂ [14], MoS₂ [39], WSe₂ [39], and WS₂ [40].

2.3 Conditions for Lasing

Having reviewed four examples of TMD light emitting devices in Section 1.2, it is instructive to ask whether they actually meet the conditions for laser operation. To this end, we refer to the checklist of laser criteria published by Nature Photonics in 2017 [41]. The list refers to a common set of data including threshold behavior, linewidth narrowing, polarization, and/or coherence together with recommendations of how best to represent the data to aid transparency and reproducibility. The list is partially based on a paper by Samuel et al. [42], which was motivated by the same question ("How to recognize lasing") in organic semiconductor gain materials. Samuel et al. also highlighted threshold, linewidth narrowing, beamshape, and evidence of a cavity signature, together with coherence and polarization as lasing criteria. Through assessment of the four

previously reviewed examples using these criteria, we can make the key point that coherence, which should be the ultimate criterion for lasing, is difficult to measure and hence the other conditions are often used as proxies. We also make the point that the second-order correlation function, $g^{(2)}(t)$, underpins the other signatures.

It is clear from Table 2.1 that the four examples broadly meet the criteria outlined in References [41, 42], except for coherence, which at first sight supports their claims for lasing. These criteria are summarized in columns 2-6 of Table 2.1. Unfortunately, these conditions are not sufficient, especially for microcavity lasers.

Table 2.1: Comparison of the four TMD light emitters in light of the lasing conditions put forward [41, 42].

Device	Threshold	Linewidth Narrowing	Beam	Polarization	Coherence	Quantum Threshold	Linewidth narrowing by factor 2
WSe ₂ PhCC	Yes	Yes	Yes	Yes ¹	Not Shown	No	No
WS ₂ Microdisk	Yes	Yes	Not shown	Yes	Not Shown	No	No
MoS ₂ Microdisk	Yes	Yes	Not shown	Yes	Not Shown	No	No
MoTe ₂ Nanowire	Yes	Yes	Not shown	Not shown	Not Shown	No	Not clear ²

¹Details of directional emission from the PhC cavity is presented in Ref. [13].

²The authors claim linewidth narrowing by a factor 2, but this is not supported by the data shown.

2.3.1 Laser Fundamentals

The term laser is an acronym for Light Amplification by the Stimulated Emission of Radiation. Fundamentally, a laser requires 3 main parts; a laser gain medium to amplify light; a pump source that can excite the laser gain medium; and an optical resonator to allow light to travel through the laser gain medium repeatedly and stimulate the emission of light.

2.3.1.1 Semiconductor Laser Gain Medium

The electronic structure of a semiconductor consists of two bands, the valence band E_V and the conduction band E_C , separated by the band gap energy E_G where $E_G = E_C - E_V$. When a semiconductor is in thermal equilibrium, most electrons reside within the valence band. If a photon of sufficient energy, $h\nu \geq E_G$, impinges on the semiconductor, an electron can absorb the photon and be promoted to the conduction band leaving an absence of negative charge in the valence band, known as a hole. This electron will thermalize and fall to the conduction band edge by non-radiative relaxation and then can recombine with the hole in the valence band after the spontaneous carrier lifetime τ_{sp} . This can sometimes result in the emission of a photon with energy $h\nu = E_G$ which is observed as luminescence. This process is known as spontaneous emission and the phase of the emitted photon is random. Photons with energy $h\nu \geq E_G$ can also induce an electron in the conduction band to transition to the valence band producing a photon in a process called stimulated emission. The emitted photon has the same wavelength, phase, and polarization as the incident photon. Stimulated emission is the process that produces laser light when the gain medium is surrounded by a cavity. Spontaneous and stimulated emission are illustrated through Jablonski diagrams in Figure 2.14.

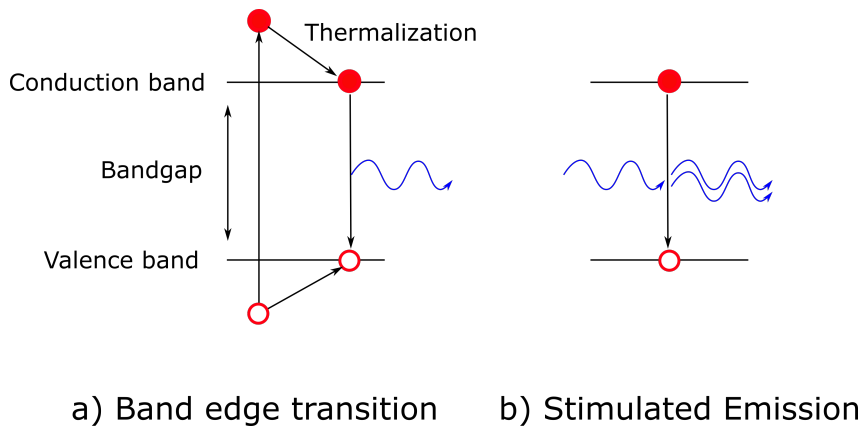


Figure 2.14: Jablonski diagram of (a) spontaneous emission and (b) stimulated emission.

2.3.1.2 Pump Source

The laser pump source can be either optical or electrical. The pump provides energy to the laser system, promoting electrons from the valence band to the

conduction band in the case of a semiconductor laser. A light source with photon energy $h\nu \geq E_G$ will be able to pump a laser gain medium. For semiconductor diode lasers, a $p-n$ junction can be formed which allows current to be injected into the depletion region. Electrons are injected via the n -doped semiconductor and holes injected via the p -doped semiconductor. The electrons and holes recombine in the depletion zone emitting photons.

2.3.1.3 Optical Resonators

The optical resonator is an integral part of a laser. The resonator provides a mechanism for light to take many round-trips through the gain medium, amplifying the signal. The simplest optical resonator would be two plane mirrors placed facing each other with the gain medium on the optical axis between the two mirrors. This configuration is often used in a gas laser such as the He-Ne laser. One mirror has high reflectivity $\sim 100\%$ and the other has a slightly lower reflectivity $\sim 99.5\%$. The low reflectivity mirror allows light to escape the resonator forming the laser beam. The optical resonator imposes resonant conditions on the light within the cavity. The allowed modes within the resonator are those which satisfy $\lambda = \frac{2L}{m}$ where L is the separation between the mirrors and m is the order of the mode. The modes are spaced in frequency by $\Delta\nu = \frac{c}{2nL}$ where c is the speed of light and n is the refractive index of the material within the resonator.

2.3.1.4 Lasing Threshold

The lasing threshold of a laser is the lowest excitation power where the laser output is dominated by stimulated emission. Below the laser threshold, emission is dominated by spontaneous emission and optical output power increases slowly with pump power. After the laser threshold is achieved, the laser output power increases dramatically with pump power, leading to a characteristic "kink" in the light-in-light-out (L-L) curve. At the laser threshold the optical gain of the lasing

medium equals the round-trip losses of the optical resonator. The threshold gain $g_{\text{threshold}}$ is given by:

$$g_{\text{threshold}} = \alpha_0 - \frac{1}{2L} \ln R_1 R_2 \quad (2.22)$$

where α_0 is the internal optical loss, and R_1, R_2 are the mirror reflectivities. Therefore to minimize the gain threshold, internal losses should be minimized and the highest possible mirror reflectivities should be used.

2.3.2 Quantum Threshold

Bjork et al. [43] highlight that the conventional definition of a laser threshold, taken as the pump power required to make the net gain of the optical mode equal to the cavity losses, may not be sufficient for a microcavity laser. Instead, they suggest a more general definition of the lasing threshold as the point where stimulated emission overtakes spontaneous emission. For a microcavity mode in an active gain medium, this will occur when the mean photon number in the mode is unity. Correspondingly, $P_{th} \equiv 1$ where P_{th} is the mean photon number in the lasing mode. This condition is also known as the quantum threshold condition since it better describes the microscopic emission processes than the conventional definition does. To illustrate the quantum condition, let us consider the case of a microcavity laser. The best-case scenario occurs when the laser has a spontaneous emission factor of $\beta = 1$ and the cavity is loss-less, so the photon lifetime is only limited by the cavity lifetime. In this case, and starting from the definition of the cavity Q-factor as the ratio of the energy stored over the energy dissipated per photon cycle, we can calculate the photon lifetime in a cavity as follows:

$$\tau = \frac{QT_{\text{cycle}}}{2\pi} \quad (2.23)$$

As a representative example for the four TMD devices discussed in Section 1.2, we choose an operating wavelength of $\lambda = 0.9 \mu\text{m}$ and a Q-factor of $Q = 5000$. From Equation 2.23 these values yield a cycle time of $T_{\text{cycle}} = 3 \text{ fs}$ and a cavity lifetime of $\tau = 2.4 \text{ ps}$. This means that the cavity must emit a photon every 2.4 ps in order to meet the quantum threshold condition. Emitting a photon of $0.9 \mu\text{m}$ wavelength

every 2.4 ps corresponds to an output power of approximately 100 nW. Typical measurements only collect a fraction of the emitted photons, characterized by the collection efficiency, so one should measure an output power of order 10s of nW from a microcavity laser of $Q = 5000$. Unfortunately, none of the devices in Table 2.1 meet this criterion.

2.3.3 Linewidth Narrowing

While the standard laser conditions [41] already stipulate linewidth narrowing, a laser should actually meet the more stringent condition of linewidth narrowing by a factor 2. This factor 2 follows on from the quantum threshold. For example, Chow et al. [44] have investigated the intensity correlation characteristics of different types of light classified by the Hanbury-Brown Twiss [45] experiment shown schematically in Figure 2.15(a). Chow shows that for coherent laser emission, the equal-time second-order photon correlation $g^{(2)}(0)$ goes to unity.

In fact, the connection between the second-order correlation function and coherence was first discussed by Mandel and Wolf in 1965 [46]. As an example, Figure 2.15(b) shows the injection current dependency on the mean photon number. For the blue and black curves, as the injection current increases, the mean photon number in the cavity exceeds unity at around 10^{-5} A. At the same point of 10^{-5} A, $g^{(2)}(0) \rightarrow 1$ signifying the onset of coherent emission (Figure 2.15(c)). This is further evidence for the quantum threshold, as at the point of quantum threshold coherent emission occurs. As the photon emission becomes more regular, and by considering the Fourier transform in the frequency domain, we can see that the linewidth of the emission must narrow as the emission pattern changes from "bunched" to "random".

The Schawlow-Townes equation then provides a quantitative assessment of the linewidth reduction on threshold [47]. A good description of this effect is also found in Chapter 11 of Siegman Lasers [48]. When a laser reaches threshold, it changes from an incoherent Gaussian noise source into a coherent sinusoidal oscillator. The Schawlow-Townes equation (Equation 2.24) then stipulates that the linewidth must be modified by a factor of 2 (Equation 2.25), as follows:

Above threshold:

$$\Delta\omega_{osc} = \frac{N_2}{N_2 - N_1} \times \frac{\pi\hbar\omega\Delta\omega_c^2}{P_{osc}} \quad (2.24)$$

Below threshold:

$$\Delta\omega_{osc} = 2 \times \frac{N_2}{N_2 - N_1} \times \frac{\pi\hbar\omega\Delta\omega_c^2}{P_{osc}} \quad (2.25)$$

where N_1 is the photon occupancy of the lower state, N_2 the photon occupancy of the upper state, the "cold cavity" linewidth $\Delta\omega_c = \omega/Q_c$, and P_{osc} the free running output power of the laser.

These considerations make it clear that the linewidth should narrow by a factor 2 on the lasing threshold. We note that while all of the four devices report a linewidth reduction, none of them provide the data to demonstrate a reduction by the full factor 2 or, preferably, a $g^{(2)}(0)$ measurement indicating coherent emission.

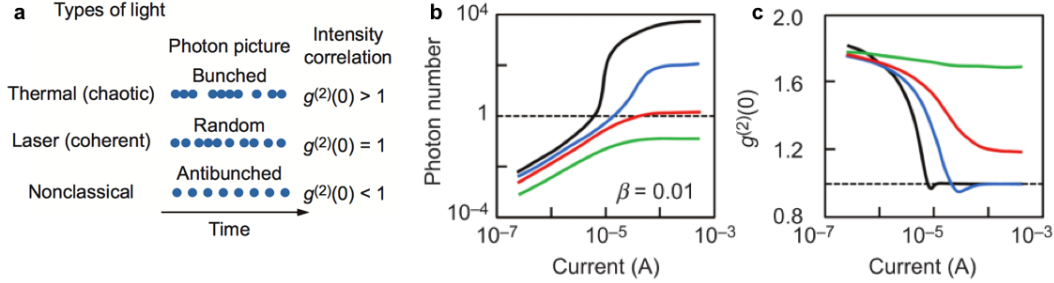


Figure 2.15: (a) Different types of light classified by a Hanbury-Brown-Twiss measurement. Injection current dependences of (b) photon number and (c) equal-time second-order photon correlation for an emitter consisting of 50 QDs in a cavity with a spontaneous emission factor $\beta = 0.01$. The different curves correspond to photon loss rates $\gamma_c = 10^{10} s^{-1}$, $5 \times 10^{10} s^{-1}$, $10^{11} s^{-1}$, and $5 \times 10^{11} s^{-1}$. QD, quantum dot. Figure reproduced from Ref. [44].

2.3.4 Hanbury-Brown and Twiss Experiment

The Hanbury-Brown and Twiss (HBT) experiment was conducted by R. Hanbury-Brown and R. Twiss in 1956 in their paper "A Test of a New Type of Stellar Interferometer on Sirius" [45]. They sought to measure the angular size of Sirius by using 2 photomultiplier tubes (PMTs) separated by 6 meters and a mirror from a search light to collect the starlight. They measured a correlation between the two intensities on the PMTs indicating a positive correlation between the two signals. Nowadays, the HBT effect is used to measure the nature of a photon emitter, be it either thermal, coherent, or quantum in nature. To achieve this, the incoming light from the emitter is split by a 50:50 beamsplitter and is coupled to 2 PMTs or avalanche photodiodes (APDs) detectors. When a photon is detected at detector 1, a start pulse is sent to a time correlating single photon counting module (TCSPC) which counts the number of photons detected in τ until a photon is detected at detector 2 which sends a stop pulse to the TCSPC. A histogram of the time delay τ is built up by the TCSPC. The second-order correlation function $g^{(2)}(\tau)$ is then given by:

$$g^{(2)}(\tau) = \frac{\langle n_1(t)n_2(t+\tau) \rangle}{\langle n_1(t) \rangle \langle n_2(t+\tau) \rangle} \quad (2.26)$$

where $n_{1,2}(t)$ are the number of detected counts at each detector at time t . The time $\tau = t_2 - t_1$ is the time delay between the photon arrival time at detector 1 (t_1) and the photon arrival time at detector 2 (t_2).

The second-order correlation function $g^{(2)}(\tau)$ relates to the nature of the light emitter. For thermal light sources such as a halogen light bulb, photons are emitted in bunches (see Figure 2.15(a)). The bunching of the emitted photons in time gives the correlation function at zero delay, i.e. $\tau = 0$, $g^{(2)}(0) > 1$ as if a photon is detected at detector 1 there is a high probability that another photon is detected simultaneously at detector 2. For coherent emission such as that from a laser, the photons are emitted randomly giving $g^{(2)}(0) = 1$ as the probability of detecting a photon at detector 2 is equal for all time delays τ . The third case is that of quantum emitters such as single photon sources. The photons that are emitted from single photon sources are antibunched meaning that the probability of detecting a second photon at detector 2 is low for small time delays so $g^{(2)}(0) < 1$.

Therefore, the HBT experiment allows for determination of whether a light source is coherent by measuring the second-order correlation function. This direct coherency measurement is the key to prove whether a microcavity emitter is lasing. The HBT experiment is fairly routine for emitters in the visible spectrum where fast single photon avalanche photodiodes (SPADs) are available, but becomes a more difficult measurement for near-IR sources where the measurement is limited by the slow response of InGaAs APDs.

2.3.5 Beta Factor

Another consideration is the spontaneous emission coupling β -factor of the laser. Kreinberg et al. [49] investigated emission from quantum-dot high- β microcavities. They investigated three classes of devices: LEDs, cavity-enhanced LEDs, and lasers with β -factors ranging from 0.37-0.72. It was easy to distinguish between LED emission and cavity-enhanced LED/lasing via the L-L curves where LED showed strong saturation at high pump powers as shown in Figure 2.16.

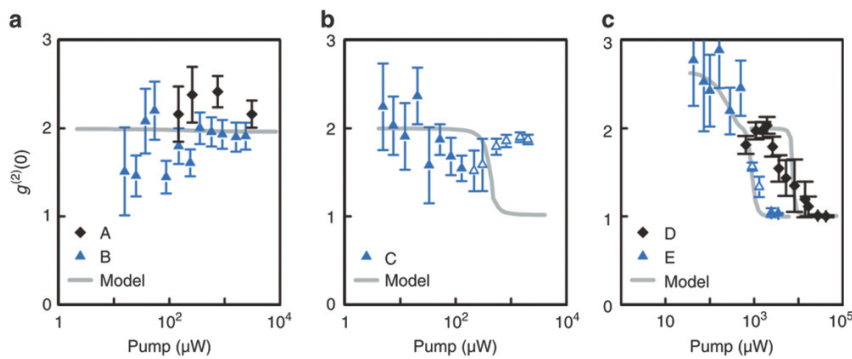


Figure 2.16: Equal-time intensity correlation versus pump power for a QD-micropillar (a) LED, (b) cavity-enhanced LED, and (c) laser. The gray curves represent theory. The data points are from experiment, where the solid symbols indicate $g^{(2)}(0)$ analysis by integration and the open symbols indicate fits considering the instrument impulse response of the setup. Figure and caption reproduced from Ref. [49].

To distinguish between the cavity-enhanced LED and the laser was more difficult, both showed an s-curve in the L-L plots and significant linewidth narrowing, which could be mistaken for lasing. However, it was not until the equal-time intensity correlation $g^{(2)}(0)$ was examined and then there was a clear

difference between cavity-enhanced LED and lasing. Figure 2.16 illustrates that for the cavity-enhanced LED (b), $g^{(2)}(0)$ remains around 2 indicating thermal emission, whereas, for the laser (c), $g^{(2)}(0)$ transitions to unity at the lasing threshold indicating coherent emission.

2.3.6 Explanation of Apparent Lasing

As we have now shown that none of the four examples from Section 1.2 meet the more stringent criteria for lasing of Table 2.1, we need to ask why the devices exhibit threshold behavior, polarization and beamshape. We believe that this question can be answered via condition 6 of the Nature Photonics list, which queries whether "alternative explanations", e.g., amplified spontaneous emission, directional scattering, and modification of fluorescence spectrum by cavity, have been ruled out as being responsible for the emission characteristics [41].

Regarding polarization and beamshape, these may well be imprinted onto the beam by the cavity mode without requiring lasing, as the example of a photonic crystal cavity clearly demonstrates. As shown by Lo Savio [50] a photonic crystal cavity readily provides laser-like emission through resonant enhancement of the cavity mode. This emission is linearly polarized (otherwise, the resonant scattering method [22] would not be possible) and the cavity can provide a directed beam, especially if suitable beamshaping techniques such as "farfield optimisation" are being employed [28]. Therefore, polarization and beamshape are not sufficient to explain laser operation.

Regarding the threshold condition and the observed linewidth reduction, the papers provide insufficient data, but we propose two possible explanations for this behavior, namely (1) that these effects may be caused by amplified spontaneous emission and/or (2) that the output of the laser may be pulsed:

1. Amplified spontaneous emission (ASE) is defined as spontaneously emitted photons amplified by stimulated emission in a single pass through the gain medium. ASE can easily be mistaken for laser emission, especially in a high-Q resonator, because resonator-scattered ASE and laser emission share many properties, including the characteristic nonlinear "kink" in the

L-L curve, the linewidth narrowing, and the polarization and directionality of the output beam. In fact, laser emission from a high-gain medium always starts with ASE in the presence of a resonator. The observations of the characteristic kink and linewidth narrowing are therefore not sufficient conditions, and only coherence measurements would provide the required clarity. Alternatively, and referring back to Figure 2.15, the Hanbury-Brown Twiss experiment [45] could be used to measure the second-order photon correlation and provide an alternative proof.

2. A different explanation is that the lasers may be self-pulsating, whereby the quantum threshold is met for a short duration only. This scenario would explain the low output power and mean the device would still exhibit laser-like characteristics, such as the characteristic "kink" in the L-L curve; the device may be operating as a passively mode-locked laser based on the well-known saturable absorption properties of TMDs [51]. To investigate the plausibility of this explanation, the emission of the laser could be measured using an ultrafast detector with picosecond time resolution, such as a streak camera; the time-dependent emission of the laser would then become evident. Since the output would be coherent if the quantum threshold condition was met for the duration of the pulse, second-order photon correlation, i.e. $g^{(2)}(0)$ measurements, should also be successful. For the linewidth narrowing at the lasing threshold, we would expect the linewidth of a pulsed laser to be wider than that of a cw laser as, according to Fourier analysis, a short pulse exhibits a wider range of frequencies than a long pulse. Hence, such broadening would screen the factor 2 narrowing at the lasing threshold observed.

2.3.7 Summary

In this chapter we built up the theory of photonic crystals, from Maxwell's equations to describing 2D photonic crystal slabs. The Ln-type photonic crystal cavity was discussed in detail, along with methods of optimising their Q -factor and out coupling efficiency in Section 2.1.7. The Ln-type photonic crystal cavity will be the basis for investigation in Chapter 3. Next, 2D materials were discussed with a focus on their attractive properties as light emitting materials for use with on-chip light sources. Finally, a detailed discussion on the conditions of lasing

for microcavity lasers was covered. The take home message from the conditions for lasing is that proof of coherent light emission is a key requirement to proving that an emitter is lasing. As mentioned in Section 2.3.3, a proxy for establishing coherence is to measure a narrowing of laser linewidth by a factor 2 at the laser threshold. This occurs due to the source changing from an incoherent Gaussian noise source into a coherent sinusoidal oscillator as defined by the Schawlow-Townes equation. However in situations where other factors may obscure the linewidth narrowing, such as pulsed operation, a direct measure of coherence is required to confirm such behaviour. In these cases, the use of a second-order correlation function is required to ensure all conditions of laser are met.

3 Photonic Crystal Cavities

In this chapter, the fabrication and characterisation of photonic crystal cavities (PhCCs) will be discussed. Silicon photonic crystal cavities will be the basis of our eventual MoTe₂ laser. Specifically "Ln" type PhCCs (as discussed in Section 2.1.6.1) are fabricated and characterised. The characterisation of the PhCCs required the development of a resonant scattering setup in York, the design of which is discussed.

3.1 Nanofabrication of Photonic Crystal Cavities

The nanofabrication of photonic crystal cavities will be discussed in this section. An overview of this fabrication procedure is schematically shown in Figure 3.1.

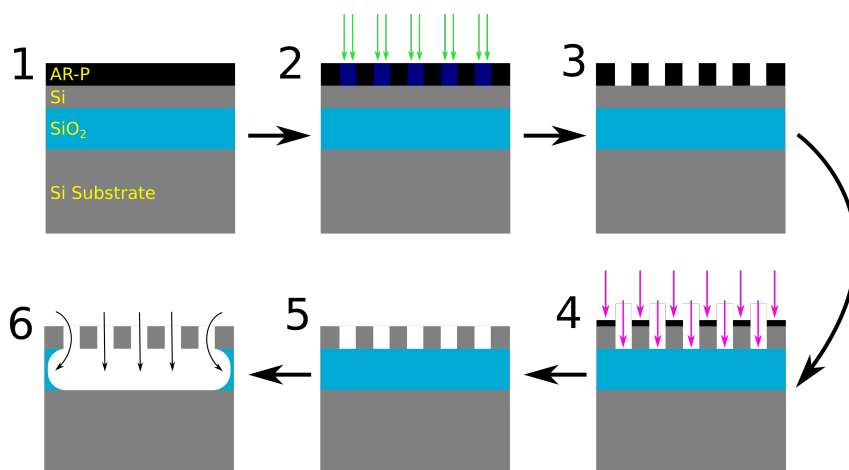


Figure 3.1: Overview of nanofabrication steps for photonic crystal cavities. (1) Sample cleaning and spin coating. (2) Electron beam lithography exposure. (3) Development. (4) Reactive-ion etching. (5) Resist removal. (6) Underetching.

There are six main steps to the fabrication; surface preparation and spin coating, patterning via electron beam lithography, development of the resist, etching of the crystals via reactive-ion etching, resist removal, and under etching.

3.1.1 Substrate Preparation

Fabrication of photonic crystal cavities begins with the preparation of the substrate. The Silicon-on-Insulator wafers from SOITEC are 8" in diameter with (100) crystal orientation, and so this wafer needs breaking down into smaller individual samples. The substrate is divided by mechanical cleaving whereby a diamond tipped scribe is used to create a defect in the direction of a crystal plane. Following the application of gentle pressure over the scribe mark using the scribe as a fulcrum, the wafer is cleaved along a crystal plane. This cleaving process is then repeated until the desired sample size is achieved. Once the sample is of the desired size, the sample is cleaned of any contamination, particulate matter or organic, before it can be coated with resist. The standard cleaning procedure is to submerge the sample in a clean beaker of acetone and sonicate it in an ultrasonic bath for 5 minutes. The acetone binds to organic contaminants and the cavitation produced by the ultrasonic bath acts to mechanically scrub them from the surface. The sample is removed from the acetone and transferred to a beaker of isopropanol. The sample is then sonicated for a further 5 minutes. The isopropanol removes the acetone residue and evaporates from the surface more cleanly than acetone. The drying process is accelerated with a jet of dry filtered nitrogen from a hand-held gun. For more heavily contaminated samples, a surprisingly effective initial cleaning step is to mechanically exfoliate the surface with low-adhesion wafer tape, which acts to remove larger particulate matter before the acetone/isopropanol cleaning steps.

Some substrates may be too delicate to be sonicated, such as membraned photonic crystals, or some contaminants may resist attack by acetone. In these cases, more involved cleaning steps are required as detailed in the following:

- For polymer resists, a proprietary mix of organic solvents ("1165") from Dow-Corning is used. The substrate is submerged in a beaker of 1165 then heated

up in a warm water bath. If the substrate is robust, then the sample can be sonicated to enhance the cleaning action.

- To remove very stubborn organic contaminants, piranha solution can be used. Piranha is a strong oxidizing agent formed of a mixture of sulphuric acid (H_2SO_4) and hydrogen peroxide (H_2O_2). When sulphuric acid and hydrogen peroxide react together Caro's acid (H_2SO_5) is formed ($\text{H}_2\text{SO}_4 + \text{H}_2\text{O}_2 \longrightarrow \text{H}_2\text{SO}_5 + \text{H}_2\text{O}$). Caro's acid is able to rapidly break down organic materials to elemental carbon. The other reaction that occurs is for the sulphuric acid to increase the oxidizing strength of the peroxide by forming a hydronium ion H_3O^+ and elemental oxygen ($\text{H}_2\text{SO}_4 + \text{H}_2\text{O}_2 \longrightarrow \text{H}_3\text{O}^+ + \text{HSO}_4^- + \text{O}\cdot$). The elemental oxygen is readily able to oxidize the carbon deposits. Treatment with piranha solution has the added benefit of modifying the surface energy of the sample allowing resists to better wet the surface.
- For samples too delicate for the vigorous piranha solution, the sample can be ashed in an oxygen asher. An asher is a plasma reactor at low pressure, typically using oxygen. Radio frequency energy is coupled into the chamber and ionizes the gas to form a plasma. Within the plasma, reactive oxygen species are produced which are able to oxidize the organic contaminants. The oxygen ashing modifies the surface energy of the sample and can be also used to promote wetting of spin coated resists.

3.1.2 Spin Coating

To prepare the sample for lithography, the surface must be coated with a resist that is sensitive to UV radiation or to electrons. To ensure that the resist is of uniform and deterministic thickness across the sample, the resist is spin coated. To spin coat, the sample is placed on a rotating vacuum chuck which secures the sample. The resist is filtered to remove any contaminants with a $0.22 \mu\text{m}$ pore filter. Next, a sufficient amount of resist is drop cast onto the sample ensuring the whole sample is covered. The sample is then rotated at high speed (500-5000 rpm) to evenly spread the resist to a thin film. The thickness of the thin film is a function of spin speed and viscosity. The uniformity of the resultant thin film depends on the spin duration, surface wetting, humidity, and temperature. The viscosity of the resist can often be changed by dilution with the correct solvent to achieve a

thinner layer. Following spin coating, the sample is "soft-baked" on a hotplate to boil off the solvent and to dry the film. It is important to bake the sample at a sufficiently high enough temperature to boil off the solvent yet at a temperature low enough not to damage the resist.

3.1.3 Electron-beam Lithography

To pattern photonic devices down at the hundreds of nanometer scale there are two main methods. Industrially deep-UV photolithography is used in semiconductor fabs such as Intel. This has the advantage of high throughput, however, very expensive photomasks are required to achieve such resolution. In a research setting electron beam lithography (EBL) is favoured. While the throughput of an EBL is very low, the flexibility of being able to quickly change designs is advantageous.

3.1.3.1 Resists

A resist is used in lithography to transfer a pattern into another layer. Resists should be sensitive to either light or charged particles so they can be patterned when exposed to either UV light or an electron beam (for electron sensitive e-beam resists). Resists can be either positive or negative tone. A positive-tone resist will be removed after development where it has been exposed, while a negative tone resist will remain after development where it has been exposed. The choice of positive or negative tone resists depends on the structures to be written; in particular, electron beam lithography being a serial process aims to minimize the exposure time. To produce a photonic crystal with air holes, a positive resist would be best as only the area of the holes need be exposed. However, to produce a photonic crystal consisting of dielectric rods, a negative tone resist would be best as only the area of the rods would need to be exposed. Another important feature of a resist is its resistance to the etchant. For the resist to be a successful etch mask, the resist must withstand the etching process for the time required to etch the underlying material. The etching of SOI, which we focus on here, is achieved by Reactive Ion Etching (RIE) which is a partially directional etching process. For

such a directional etch, the mask resistance can be improved by increasing the resist thickness.

We will now focus on positive-tone electron beam resists. The e-beam resist that was used to fabricate the photonic crystals within this work was AR-P 6200 (CSAR 62) from AllResist GmbH which from now on will be referred to as AR-P. AR-P is a highly sensitive, high resolution electron beam resist. The high sensitivity reduces the exposure dose required and hence shortens exposure time. The high resolution allows very small feature sizes to be patterned, with features as small as 10 nm having been achieved. The CSAR name stands for chemically semi-amplified resist, and was developed to be a "best of both worlds" solution combining the high sensitivity of a chemically amplified resist (CAR) and the high resolution but low sensitivity of a conventional e-beam resist such as PMMA. Chemically amplified resists are polymers which have acid sensitive groups attached (pendant) to the polymer chain [52]. Mixed into the resist is a compound that produces an acidic product when irradiated by electrons. The free acidic product catalyzes the removal of the pendant groups from the polymer chains in the resist (deprotection). Often this process is sped up using a post-exposure bake. Due to the catalytic nature of the process, one acidic product can deprotect a large number of polymer chains, hence amplifying the initial electron dose. This chemical amplification leads to high sensitivity but at the expense of resolution, as the process is diffusion limited. In conventional e-beam resists, the scission of the polymer chains is performed directly by the electron beam giving high resolution, but requires a high electron dose hence a longer dwell time to write an area.

3.1.3.2 Resist Development

Once the resist has been patterned by EBL, the resist contains a latent image of the exposure and needs to be developed to remove the exposed areas (for a positive-tone resist). This process is the same as developing photographic film using wet chemistry to reveal the image taken. For AR-P, our procedure is to submerge the sample in Xylene for 60 s. Xylene is able to selectively dissolve the now weakened polymers due to bond breaking in the exposed areas while minimally affecting the unexposed areas.

3.1.3.3 Design of Electron Beam Lithography Pattern

The design of the EBL patterns was assisted by a in-house MATLAB script for creating L3 photonic crystal cavities. This script was extended to produce Ln-type PhCCs from L3 to L9 during this PhD. The Ln-type PhCCs were modified for gentle confinement and far-field optimisation using parameters as discussed in Sections 2.1.7 and 2.1.8 respectively. The generated GDSII patterns consisted of arrays of PhCCs of varying period in the y -direction and dose factor in the x -direction. For Ln-type cavities to resonate around the 1100 nm MoTe₂ photoluminescence peak, cavities were fabricated with periods in the range $280 < a < 340$ and dose factors in the range $0.5 < df < 1.5$.

3.1.3.4 RAITH Voyager Electron Beam Lithography

While deep-UV photolithography is used industrially for the fabrication of microelectronic circuits where many copies of the same structure are required, the setup cost and inflexibility of producing high-resolution photomasks is not viable for research within a university. Electron beam lithography (EBL) then provides the flexibility to produce many different types of nanostructures and to rapidly iterate designs. At the heart of EBL is a scanning electron microscope which can accelerate and focus a narrow beam of electrons from an electron source onto a target. The specifications for the RAITH Voyager EBL employed in these studies are given below in Table 3.1.

Table 3.1: RAITH Voyager EBL specification.

Beam Acceleration	50 kV
Beam Current	50 pA-40 nA
Pattern Generator	50 MHz
Stage size	150 x 150 mm
Writefield size	500 x 500 μ m
Writefield stitching accuracy	≤ 20 nm
Overlay accuracy	≤ 20 nm
Writing speed	1 cm ² /hr (max)

The control software breaks down the design pattern into individual writefields and the pattern generator subdivides the pattern into individual 0.5 nm^2 pixels to be scanned by the electron beam. The electron beam is then vector-scanned across the writefield by a pair of electrostatic deflection plates. When the beam arrives at a pixel that should not be exposed, exposure is prevented by deflecting the beam from the beam axis using an electrostatic beam blanker located above the aperture. The writing speed is limited by the speed of the beam blanker and the beam deflection speed. Once a writefield has been completed, the beam is again blanked and the stage is moved to the next writefield by piezoelectric actuators whilst the position is monitored by a laser interferometer and the process repeats.

To produce a precise pattern, the electron beam must be tightly focused and should be circular in shape. Any non-circularity causes astigmatism, which is corrected by a quadrupole electromagnetic stigmator. Using a nanopillar calibration sample, the stigmation script iteratively corrects the astigmatism to ensure that the pillars are circular. Next, using a chess board sample, the field distortion is corrected to ensure that the beam is in focus when deflected across the writefield.

Our Raith Voyager EBL system has a $500 \times 500 \text{ }\mu\text{m}$ writefield size, which is sufficiently large to write many photonic crystal patterns without the need for writefield stitching. To produce structures that are larger than the writefield, precise writefield alignment procedures need to be executed to minimize stitching errors. First, a cross shaped pattern is made on the sample by burning spots into the resist using the beam. The software then moves the stage away from this point and attempts to scan the same image by deflecting the beam. The system then compares the initial image (produced with the beam centred under the column) and the final image (produced with the beam deflected) of the pattern and makes relevant corrections to the deflection optics. This process is iterated to minimize positioning errors until a threshold figure of merit is achieved.

To calculate the beam dwell time at every pixel, the beam current must be measured. The beam current is measured by aiming the electron beam into a Faraday cup and measuring the resulting current with a picoammeter. Once the beam current is known, the pixel dwell time can be calculated from the specified electron dose in $\mu\text{C}/\text{cm}^2$. A base dose of $130 \mu\text{C}/\text{cm}^2$ is typically used for exposure of photonic crystals with AR-P. To ensure that a sufficient dose is applied to the

resist for it to fully clear, a dose test is performed. Features of a similar size to the design features are written with varying dose factors, usually varying from 0.5-2 times the base dose. These are then developed for a fixed time and then the lowest dose where the resist has fully cleared is identified. The clearing dose can be found by inspection with optical microscopy, or more accurately, with a surface profilometer or an AFM.

When a high energy electron beam is incident on the sample, the electrons undergo collisions with atoms within the resist and within the substrate (these are represented schematically in Figure 3.2(a)). Collisions with atoms can cause electrons to be knocked off their atomic shell and produce lower energy secondary electrons (SE_I) that scatter. These secondary electrons have sufficient energy to expose the resist and broaden the exposure of a single point. Electrons that penetrate into the substrate can be backscattered at high angles and with energies similar to the incident beam. This backscattering effect is dependent on the charge of the atoms (δ) and it increases with atomic number (Z). These backscattered electrons can also produce secondary electrons along their path (SE_{II}) that cause long range broadening of the exposed area. This broadening of the initial point exposure is defined by the point spread function (PSF).

$$PSF(r) = \frac{1}{\pi(1+\eta)} \left[\frac{1}{\alpha^2} e^{-\frac{r^2}{\alpha^2}} + \frac{\eta}{\beta^2} e^{-\frac{r^2}{\beta^2}} \right] \quad (3.1)$$

where α is the range of the forward scattered electrons, β is the range of backscattered electrons and η is the backscattering coefficient determining the ratio of backscattered electrons to forward scattered electrons.

This point spread function has a double Gaussian shape, which is plotted in Figure 3.2(b). When two points are exposed next to one another, the point spread functions add and create an exposed area as shown in Figure 3.3.

This dependence is known as the proximity effect, which causes inhomogeneities in hole radii of the photonic crystal; holes that are closer together receive more dose from neighbours and turn out larger than holes that are further apart. Consequently, the proximity effect affects holes near the edge of the photonic crystal more as they receive less exposure. The proximity effect can be addressed by lithographic tuning, which means that holes near the edge are designed larger to account for the underexposure they receive.

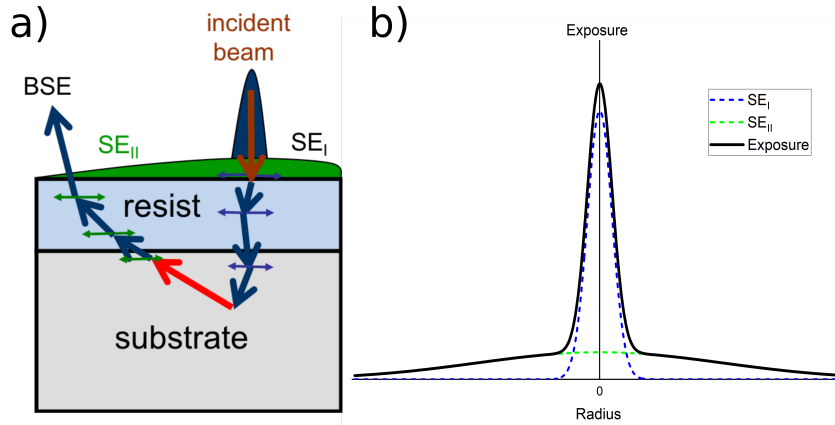


Figure 3.2: (a) Forward and backscattering effects for electrons entering a resist and a substrate. Secondary electrons SE_I are formed in the path of the beam after a forwards scattering event, SE_{II} are secondary electrons formed after a backscattering event. (b) Exposure of a single point due to the point spread function of the EBL process.

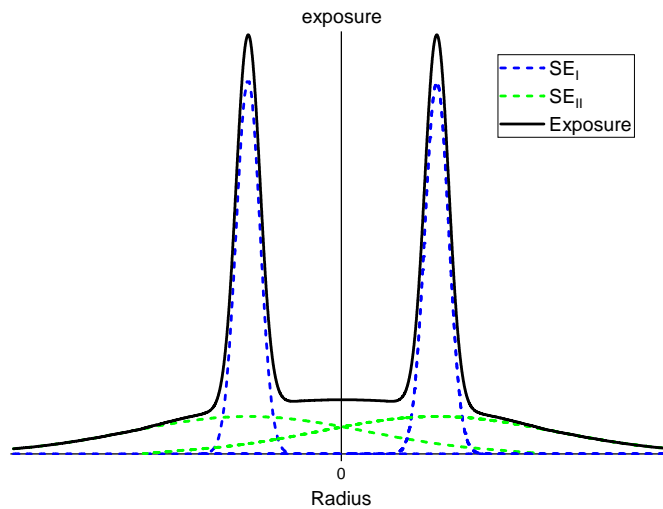


Figure 3.3: EBL exposure of two points closely placed together. The black line is the total exposure due to the combination of SE_I and SE_{II} electrons.

3.1.4 Reactive Ion Etching

Reactive-ion etching (RIE) is a plasma etching technique used in nanofabrication to transfer a pattern from a resist into a substrate. Our in-house built RIE system is a capacitively-coupled design in which the sample stage is driven by an RF power supply at 13.65 MHz and the remainder of the chamber is grounded. There is a tuning network which matches the impedance of the RF

source to that of the plasma to minimize the reflected RF power. The rapidly oscillating electric field ionizes the gas within the vacuum chamber producing electrons. These electrons are then accelerated by the RF field and undergo collisions with other atoms in the chamber. These collisions ionize other atoms and produce secondary electrons. If the field is sufficiently strong, this process produces an electron avalanche breakdown, after which the plasma becomes conductive. The electron mobility within the plasma is much greater than that of the ions in the plasma, hence the electrons are driven by the alternating RF field and hit the driving electrode every half RF cycle. The resulting buildup of electrons at the electrode creates a DC self-bias voltage between the bulk plasma and the electrode known as the plasma sheath. In the tuning network there is a blocking capacitor which acts as a conductor for the RF field but insulates the circuit from the DC self-bias voltage. [53].

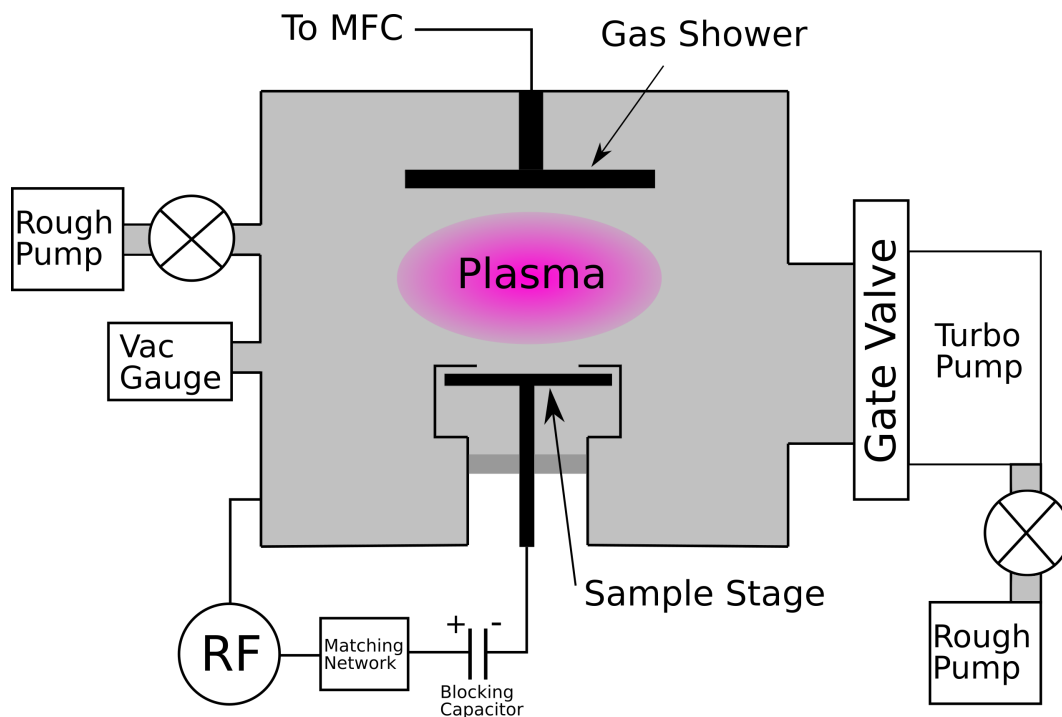


Figure 3.4: Schematic diagram of the reactive-ion etching system used in this PhD project.

The chamber is pumped with a turbomolecular pump which can achieve a base pressure of 10^{-7} mBar or better. The turbopump is throttled by an actively controlled gate valve in order to control the pressure in the chamber. The flow of the reactive gasses into the reaction chamber is controlled by a mass-flow controller (MFC). A mass flow controller is set for a specific gas flow to enter the chamber, usually measured in standard cubic centimeters per minute (SCCM).

The mass flow of gas is measured in the MFC by heating the gas and measuring the temperature difference between two positions. The MFC has a throttle valve that is actuated by a control circuit to maintain a steady gas flow.

Table 3.2: Silicon RIE etch chemistry.

Process gas	$\text{CHF}_3, \text{SF}_6$
Radicals	$\text{SF}_5\cdot, \text{F}\cdot, \text{CF}_2\cdot$
Products	SiF_4, HF
Passivation layer	$\text{Si}_x\text{C}_y\text{F}_z$

Within the plasma, many species are formed by the electron-induced ionization of the process gas and these have been summarised in Table 3.2. These species include neutrals, electrons, photons, radicals ($\text{F}\cdot$), positive ions (SF_5^+) and negative ions (F^-) [54]. Conversely, the transport of charged particles within the plasma is controlled by electric fields. Positive ions produced in the bulk plasma are accelerated towards the negatively charged substrate by the DC self-bias voltage. Transport of neutrals and radicals is diffusion driven. There are two main components to reactive ion etching, namely physical etching and chemical etching.

Physical etching of silicon is due to the acceleration of heavy ions in the plasma sheath region. These heavy ions bombard the surface, transferring momentum and sputtering off material. As the DC self-bias voltage in the plasma sheath is perpendicular to the substrate, the ion bombardment is directional. This directionality gives an anisotropic etch as the etch rate perpendicular to the surface is greater than that in the parallel direction. The rate of sputtering is largely controlled by the DC self-bias voltage. The DC self-bias is inversely proportional to the chamber pressure and directly proportional to the RF forward power. These parameters can be used to tune the rate of sputtering. Physical etching is as material selective as chemical etching, so a balance must be found. If the DC self-bias is too high, then the resist may be etched faster than the silicon and the mask may be consumed before the required etch depth is achieved. The optimised parameters that were used in this project are stated within Table 3.3.

Table 3.3: Silicon RIE recipe.

CHF ₃ Flow	14.5 SCCM
SF ₆ Flow	12.5 SCCM
Pressure	4.0x10 ⁻² mBar
DC self-bias	180 V
RF Power	23-26 W

Chemical etching is the second type of etch mechanism. While physical etching is anisotropic, chemical etching is isotropic as the etch rate is the same in all directions. Fluorine radicals F· are created within the plasma by the dissociation of fluorine from SF₆ and CHF₃. The fluorine radicals diffuse to the silicon surface and adsorb onto the surface. When the fluorine radicals come into contact with silicon, they can form bonds with the silicon and they spontaneously liberate silicon from the surface by forming volatile SiF₄ ($4\text{F}\cdot(\text{g}) + \text{Si} \longrightarrow \text{SiF}_4(\text{g})$) or by forming a precursor SiF_x. To allow the reaction products to desorb from the surface, they need to be volatile at the substrate temperature and the vacuum pressure. The reaction products can then diffuse into the chamber and are eventually pumped away by the pumping system.

The rate of chemical etching is influenced by the population of fluorine radicals and the number of active sites where F· can bind to Si. To increase fluorine radical population, a higher concentration of SF₆ is added, whereas increasing CHF₃ flow can deplete the fluorine radical population by forming HF which is comparatively inert in this context. Increasing the RF power leads to an increase of the DC self-bias voltage, giving the ions more energy; on the contrary, a higher DC bias also increases the formation rate of F·. Increased sputtering rates also create more surface area for the chemical reactions to etch, and the physical sputtering can break away reaction byproducts that may inhibit the etching process. Therefore, the chemical and physical etching rates are synergistically linked without the ability to independently tune each component. With modifications to the RF power supply, it is possible to independently control the ionization rates and the ion bombardment within a RF driven capacitively coupled plasma, by using two RF frequencies to drive the plasma. The electrons are driven by the 13.56 MHz RF frequency controlling the ionization of the plasma and a low frequency RF signal (~100 kHz) can be used to independently drive the ions within the plasma. Tuning

these two RF frequencies can allow independent control of ion bombardment and ion production [55].

A third process occurs during RIE etching, which is the formation of a passivation layer and this has been illustrated in Figure 3.5. This layer is formed of $\text{Si}_x\text{C}_y\text{F}_z$ growing on the substrate and it inhibits the chemical etching process. This passivation layer is broken down by ion bombardment on the bottom of the etch profile while it remains on the sidewall, which is not directly exposed to the ion bombardment. The passivation layer on the sidewall therefore prevents the chemical etch laterally and leads to an anisotropic etch direction. However, if the rate of formation of the passivation layer is faster than that of its erosion, then the etch will stop.

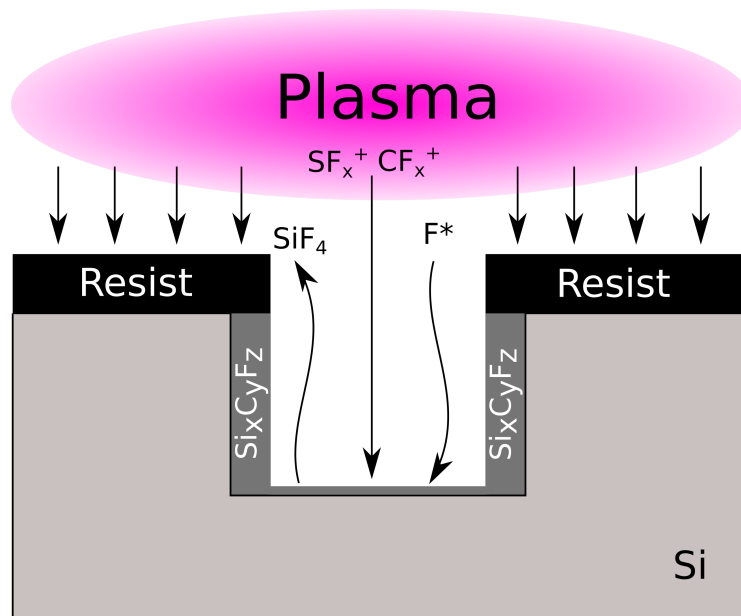


Figure 3.5: Schematic of etching processes of silicon within the RIE system.

The etch rate is dependent on the size of the features to be etched. High aspect ratio features, i.e. those for which the depth is greater than the width, etch slower than low aspect ratio features. This is schematically shown in Figure 3.6. The lower etch rate occurs due to the depletion of ions by collisions with sidewalls of the etch [56]. This effect is termed "RIE lag" and it needs to be considered for photonic crystal cavities with non-uniform hole radii, typically requiring a slightly longer etch time to ensure that the smallest features are fully etched. This has the consequence of changing the radii of other holes, so it requires lithographic tuning to achieve the target resonant wavelength. The resonance can be lithographically tuned by varying the dose factor of the holes to reduce or enlarge their size.

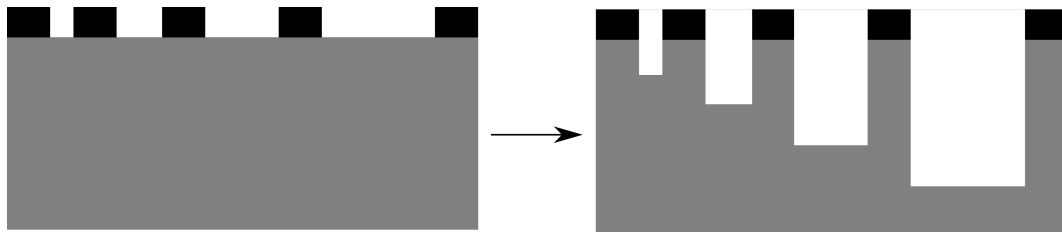


Figure 3.6: Schematic diagram showing the RIE etch depth dependence with feature size.

3.1.5 Resist Removal

After the etching process, some resist remains covering the photonic crystal. To remove the remaining resist and leave a clean silicon surface, the sample is submerged in a beaker of warm resist stripper (DOW Microposit Remover 1165) for 10 minutes. If the resist residue is particularly stubborn to remove, the sample can be placed in the ultrasonic bath at low power to assist resist removal. The sample is rinsed in acetone, IPA and then DI water to remove any remaining organic materials. A final cleaning step in piranha solution is required to produce the cleanest sample possible.

3.1.6 Underetching the Cavity

The photonic crystal can now be underetched to remove the SiO_2 layer below the crystal. A buffered HF solution is used to dissolve the SiO_2 through the etched holes in the PhCC. The etch solution is buffered with ammonium fluoride (NH_4F) to reduce the etch rate of SiO_2 in HF and to allow for a more controllable process. A 1:10 mixture of buffered HF:DI water is used and the sample is allowed to etch for 30 minutes. The sample is removed from the HF etch solution, rinsed with DI water and inspected with an optical microscope to ensure that the cavity is fully underetched. A border around the photonic crystal is visible under the microscope that indicates the PhCC has been fully etched. An SEM micrograph of an underetched PhCC is shown in Figure 3.7.

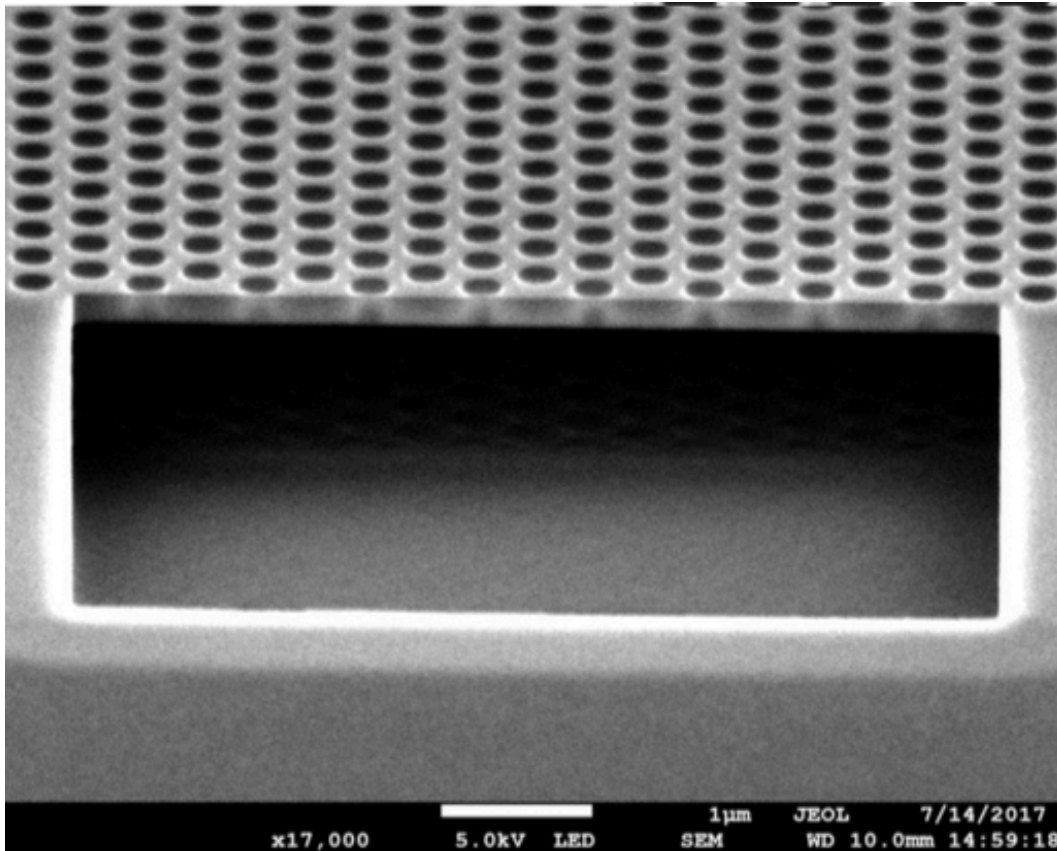


Figure 3.7: SEM micrograph of undercut photonic crystal membrane fabricated and imaged as a part of this PhD project. The etched area next to the photonic crystal shows that none of the thermal oxide layer remains. The light area surrounding the undercut marks the extent of the etch laterally.

3.1.7 Summary

In this section an in-depth discussion of the nanofabrication steps of the photonic crystal cavities that I used to produce photonic crystal cavities were covered. The SOI wafers were cleaned and spin coated with AR-P EBL resist. The photonic crystal cavity GDSII pattern was generated for a range of periods and dose factors. The coated SOI was patterned with Ln PhCCs via electron beam lithography. The patterned substrates were developed to clear the exposed areas. Then the PhCCs were etched using our reactive-ion etcher. The PhCCs were finally cleaned and underetched using HF to produce a membraned structure.

3.2 Optical Characterization

To characterize the optical properties of the photonic crystal cavities, light must first be coupled into the cavity and the transmitted light needs to be measured spectroscopically. This can be achieved by several methods depending on the wavelength of the cavity resonance and the Q -factor of the cavity. For lower Q -factor cavities, a broad light source can be coupled to the cavity via a microscope objective and the scattered light measured by a spectrometer. This method is limited by the spectrometer resolution. For high Q -factor cavities, a tunable laser can be scanned across the cavity resonance and the scattered power measured with a photodiode. The resolution of this method is limited by the wavelength step size and linewidth of the tunable laser source. Finally, for cavities with resonances between 1025 nm and 1200 nm, the photoluminescence of silicon can be used to excite the cavity resonance and this can be measured with the spectrometer.

Figure 3.8 shows the broadband light sources we have available within the lab. For resonances around 1100 nm in silicon photonic crystal cavities, the band edge emission from silicon can be used to produce light within the cavity itself by pumping the silicon with a 532 nm DPSS laser. For resonances around 1300 nm, a superluminescent diode source is available. For resonances in the C+L telecom band (1530-1625 nm), an amplified spontaneous emission (ASE) source based upon an erbium-doped fiber amplifier (EDFA) is available.

3.2.1 Resonant Scattering

In order to characterize the optical properties of the photonic crystal cavities, the cavity resonance must first be excited and then measured spectrally. To excite the cavity resonance there are two possible methods: 1) to use a broad band light source such as a superluminescent diode (SLD) and obtain spectral resolution with a spectrometer and linear detector array, or 2) use a spectrally narrow tuneable laser and scan across the cavity resonance measuring the reflected power using an InGaAs photodetector. We will consider both of these options.

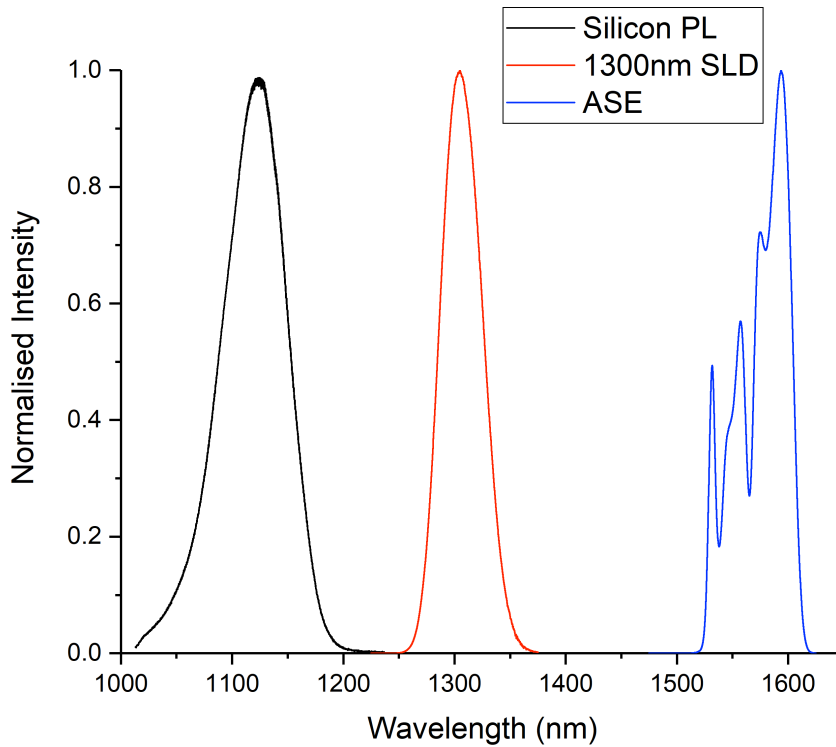


Figure 3.8: Broadband light sources for examining photonic crystal cavity resonances. Spectra measured using an Ando AQ6317B optical spectrum analyser (OSA) and plotted with normalised intensity.

3.2.1.1 Theory of Resonant Scattering

The resonant scattering (RS) method was developed by Portalupi et al. [28] at the University of Pavia, Italy. The RS method seeks to improve the signal-to-noise ratio (SNR) of the farfield coupled cavity resonance to the background reflection of the photonic crystal. The increase in SNR is achieved by using crossed polarizers to filter the background reflections. The reflected light off-resonance preserves its x -polarization and is filtered by the y -orientated analyzer. By placing the photonic crystal cavity at 45° with respect to the crossed polarizers, the x -polarized light that interacts with the xy -polarized cavity mode produces a y -polarized component which passes through the analyzer. This yields a spectrum with a reduced and flattened background and a strong resonance peak.

3.2.1.2 Resonant Scattering Setup

The resonant scattering setup that I built in York (Figure 3.9) as a part of this PhD project consists of a broadband light source such as a 1300 nm superluminescent diode (SLD) or a C+L band amplified spontaneous emission (ASE) source. The light source is collimated from the single mode fiber with a fiber collimation package (Thorlabs F810FC-1550) and then linearly polarized in the x -direction with a nanoparticle linear film polarizer with extinction ratio $>100000:1$ for 850-1650 nm (Thorlabs LPNIR100). The light then passes through a 50:50 plate beamsplitter (Thorlabs BSW29R) and into a Mitutoyo 50x infinity corrected long working distance objective, which focuses the light onto the sample in a tight spot (approximately $2\ \mu\text{m}$).

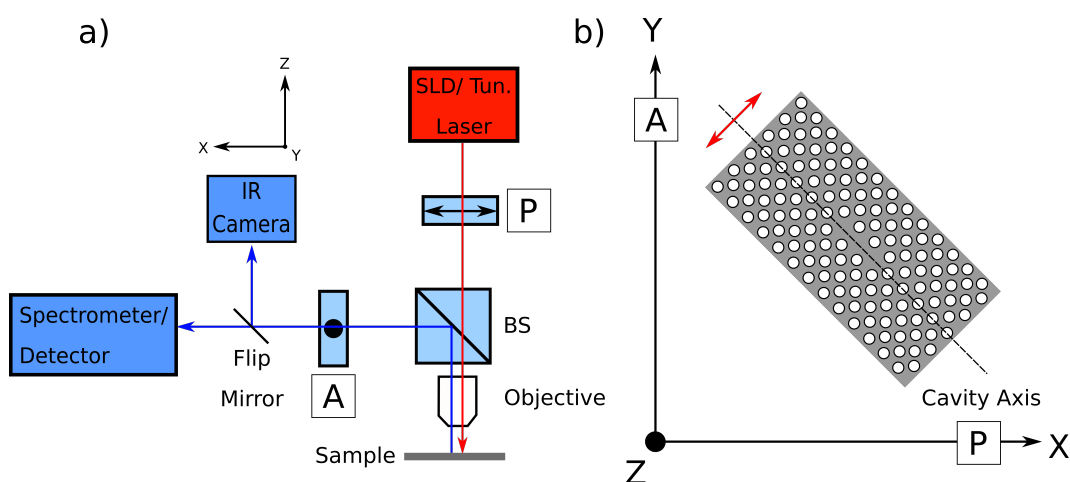


Figure 3.9: Schematic diagram of the resonant scattering setup built at York (a) used to characterize the fabricated photonic crystal cavities. Either a broadband SLD or a tunable laser is linearly polarized [P] and focused onto the cavity by a microscope objective. The cavity emission is collected by the objective and directed to the spectrometer/detector via a beamsplitter and an analyzer [A]. (b) A L3 PhCC is mounted at 45° with respect to the polarizer and analyzer. The cavity polarization is illustrated by the red arrow.

The photonic crystal cavity is mounted at 45° with respect to the linear polarizer on a 3-axis piezoelectric nanopositioning stage (Thorlabs MAX312D/M). The piezoelectric stage has positioning resolution of 20 nm in an open loop configuration. The ability to move the cavity with such a small stepsize is crucial to maximize the resonant scattering signal. The reflected light from the cavity along with the farfield cavity mode is collected by the same objective and directed

towards the spectrometer with the beamsplitter. Between the beamsplitter and the spectrometer, another nanoparticle linear film polarizer is placed as the analyzer. The analyzer is orientated in the y -direction, at 90° to the polarizer.

An infrared InGaAs imaging camera is used to align the cavity and the focused spot. It is useful to position the camera after the analyzer as this can be used to check that the polarizer and analyzer are crossed. When the polarizers are crossed, the spot will change from a Gaussian spot to one that has a clover leaf pattern with a dark spot in the middle illustrated in Figure 3.10(a). This cloverleaf pattern occurs as we only image the polarization that is perpendicular to the incident polarization [57]. If we imaged through aligned polarizers we would see the complementary pattern.

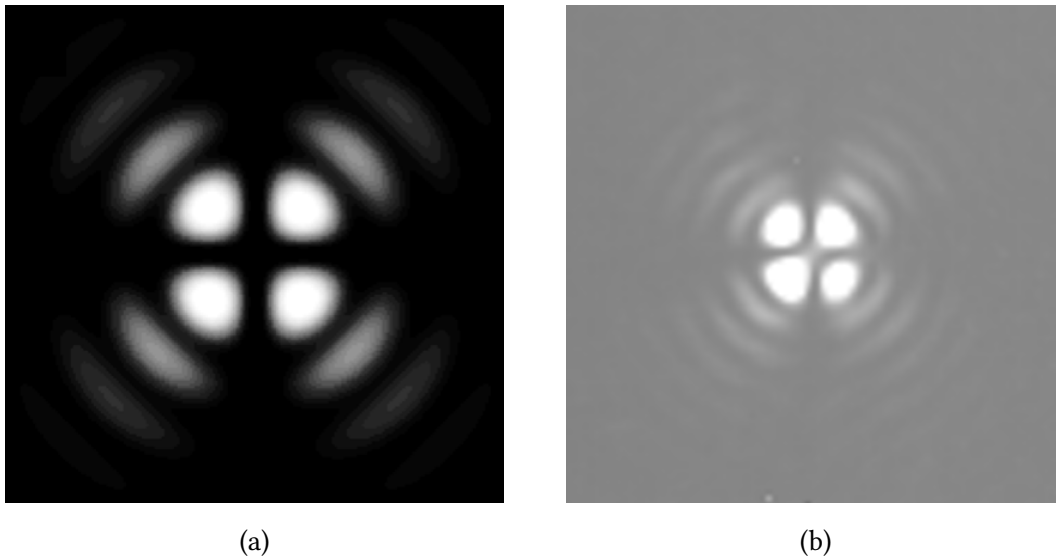


Figure 3.10: Clover leaf spot pattern when the analyzer is perpendicular to polarizer. (a) Simulation from Ref. [57]. (b) Image of cloverleaf pattern obtained from the resonant scattering setup built in York.

The resonant scattering signal is focused onto the input slit of the 750 mm spectrometer (Acton Research SpectraPro-2750) with a $f = 45$ mm aspheric lens to match the f-number of the spectrometer ($f/9.7$) and maximize the collected light. The spectrometer has 3 gratings installed with 150, 600 and 1200 grooves/mm. An InGaAs linear array detector (Andor iDus DU490A) is placed at the focal plane of the spectrometer to record the resonance spectrum. The detector is thermoelectrically cooled to -70°C to reduce background noise and the integration time is set to maximize the dynamic range of the analogue to digital converter (ADC). The measurement of resonance linewidth is limited by

the resolution of the spectrometer. With individual pixel resolution of 35pm/px, the upper limit on Q -factors that can be resolved are of order of 15000, assuming 3 data points across the peak and a wavelength of 1500 nm.

3.2.1.3 Results

The lineshape of the resonance depends on how tightly the excitation spot is focused. When the spot is tightly focused, an asymmetric peak is observed, however, when the spot is slightly defocused, a symmetric lineshape is observed. This behaviour can be explained by Fano quantum interference [22] which is described by Equation 3.2.

$$F(\omega) = A_0 + F_0 \frac{[q + 2(\omega - \omega_0)/\Gamma]^2}{1 + 2[(\omega - \omega_0)/\Gamma]^2} \quad (3.2)$$

where ω_0 is the frequency of the cavity mode, Γ is the resonance linewidth, and A_0 and F_0 are constant factors. From Fano's work [58], q is a dimensionless parameter which describes the ratio of resonant scattering amplitude to background scattering amplitude. When the resonant scattering amplitude is similar to the background scattering amplitude, $|q| \sim 1$, an asymmetric resonance is observed (Figure 3.11(c)). When background scattering dominates over

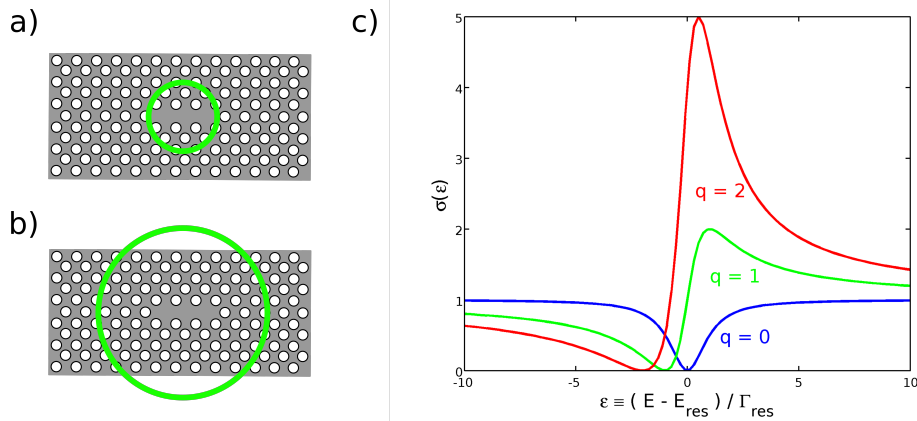
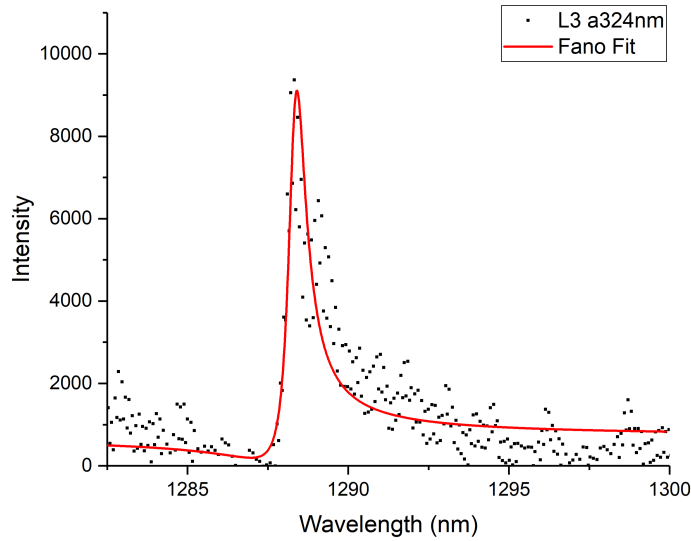


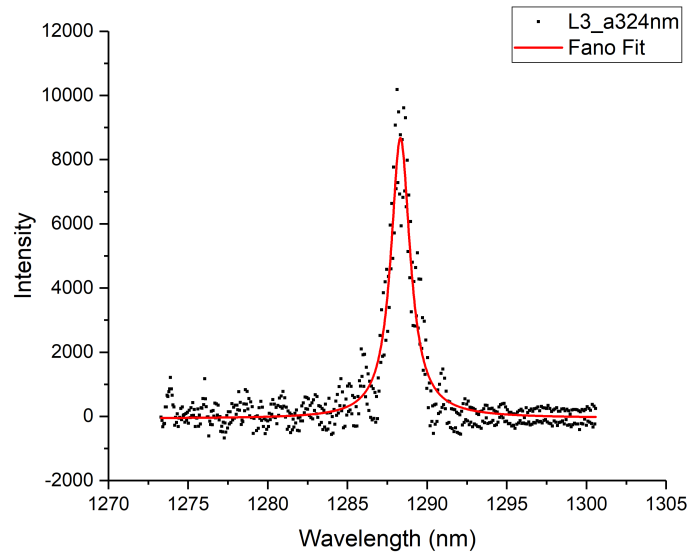
Figure 3.11: (a) L3 PhCC with tightly focused excitation spot. (b) L3 PhCC with slightly defocused excitation spot. (c) Fano lineshape plotted as a function of q from Equation 3.2.

resonant scattering, i.e $|q|$ is small, a symmetrical negative Lorentzian lineshape is observed (Figure 3.11(c)). When the excitation spot is tightly focused (see

Figure 3.11(a), the resonant scattering amplitude is similar to that of the background scattering and an asymmetric peak is observed. When the spot is defocused and a larger area is excited (Figure 3.11(b)), the amplitude of the background scattering begins to dominate over the resonant scattering and $|q|$ decreases leading to a symmetric negative Lorentzian lineshape. The negative Lorentzian peak is observed as a positive peak due to the crossed polarized measurement.



(a)



(b)

Figure 3.12: (a) L3 PhCC with period $a = 324$ nm with tightly focused excitation producing asymmetric lineshape. (b) L3 PhCC with period $a = 324$ nm with tightly focused excitation producing asymmetric lineshape.

Measurements of L3 photonic crystal cavities were taken and their spectra were fitted using the Fano function (Equation 3.2). For the case where the excitation spot was tightly focused on to the cavity (Figure 3.12(a)) an asymmetric peak is found with $q = -4.06$. When the spot was slightly defocused (Figure 3.12(b)), a symmetric peak is measured with $q = -0.01$.

Measurements of Ln-type photonic crystal cavities were taken using the resonant scattering method to verify resonant wavelengths and Q -factors. L3, L5 and L7 PhCCs with period $a = 320$ nm are shown in Figure 3.13 with resonant wavelengths between 1267 nm and 1275 nm.

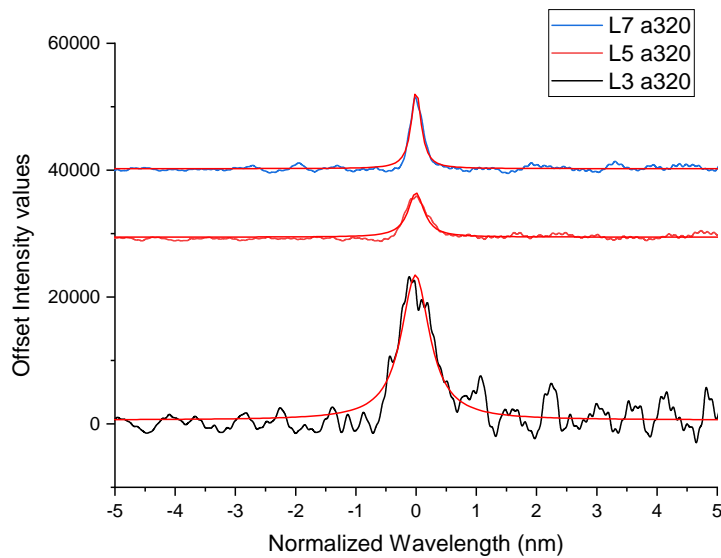


Figure 3.13: Resonant scattering spectra of L3, L5 and L7 PhCC with period $a = 320$ nm. Resonant wavelength (1270 nm) normalized to compare each cavity length.

The RS spectrum for the L3-7 cavities was plotted in normalised wavelength to aid the comparison of the fundamental cavity resonance. As the peaks were symmetric, meaning the excitation spot was slightly defocused, a Lorentzian fit was used. The low SNR of the L3 cavity was due to positioning of the cavity axis away from 45° and low Q -factor. The Ln-type cavities fabricated in this project do not possess a high Q -factor (2-7000), however, they are sufficiently high- Q to act as a resonator for a light source with 2D-TMDs. This is due to the coupling of the broad PL emission of TMDs such as MoTe_2 (see Section 4.4.3) to the narrow linewidth of PhCCs in the "bad emitter" regime as discussed in Section 2.1.6.1. Microrings are another kind of silicon photonic resonators that can achieve Q -factors up to 7×10^5 [59], but their footprint is far larger than a Ln-type PhCC

as they require large bending radii ($>5 \mu\text{m}$) to achieve high- Q . This requirement makes microring resonators much too large for integration with 2D-TMD flakes and so unsuitable for use in this project.

Q -factors were determined from the Lorentzian fit and plotted against the cavity length (Figure 3.14).

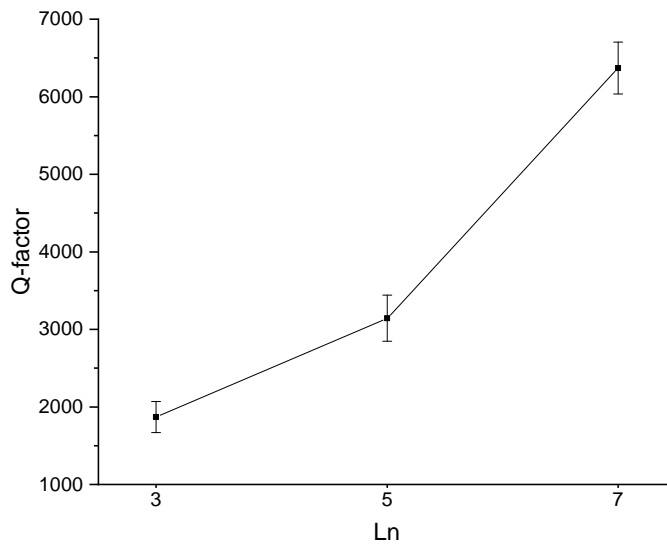


Figure 3.14: Q -factors of L3, L5 and L7 PhCC with period $a = 320 \text{ nm}$.

The Q -factor of the cavity increases with the cavity length. The main loss mechanism in a PhCC occur upon reflection at the ends of the cavity, as opposed to propagation loss. The Q -factor is defined as the energy stored divided by the energy lost per optical cycle, and so the longer the cavity, the more optical cycles can fit between loss events which increases the Q -factor.

3.2.2 Tunable Laser

To obtain measurements of cavities with Q -factors higher than 15000, a tunable laser can be used. A tunable laser such as the Santec TSL-510, which was used in Pavia, has a wavelength step size of 1 pm allowing for Q -factors of up to 5×10^5 to be resolved. The setup for the tunable laser remains broadly the same as

that for the broadband resonant scattering, however, the spectrometer is swapped for an InGaAs photodiode which measures the intensity of the resonant scattering signal as the laser is swept across the resonance. This process is controlled by LabView and the photodetector voltage is plotted against the wavelength of the tunable laser. As the spectrum can take a while to acquire at high resolution, the broadband resonant scattering technique is first used to identify the cavity resonant wavelength and to optimize the excitation spot position, then the spectrometer is swapped for the photodiode and the broadband source swapped for the tunable laser. Figure 3.12(b) shows a tunable laser spectrum of a 45000 Q -factor PhCC at 1554.5 nm.

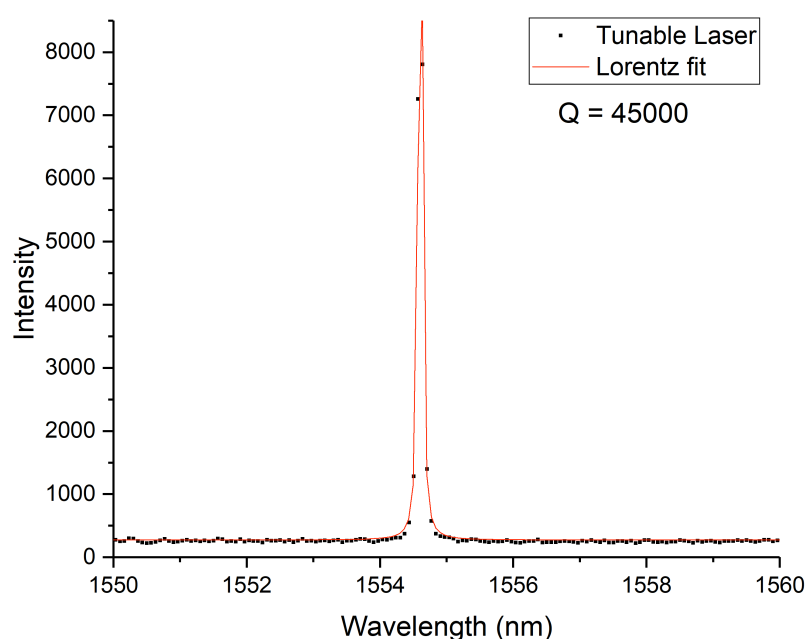


Figure 3.15: Tunable laser resonant scattering spectrum of PhCC with resonance at 1554.5 nm and Q -factor of 45000.

3.2.3 Emission from Silicon

For cavities with resonances between 1025-1200 nm where no tunable laser source was available in our laboratory, the resonance can be probed by generating light within the cavity itself. This scheme is simpler than the resonant scattering method, as no polarisers are required. By pumping the SOI using a powerful single mode 532 nm laser (Laser Quantum GEM 532), photoluminescence from the silicon band edge within the cavity is stored in the cavity and radiates out due to the farfield emission optimisation. The emission from the cavity is then measured

with the spectrometer. Due to the weak emission from silicon, high pump powers of 30 mW are required, e.g. several orders higher than that required to pump other materials such as MoTe_2 which requires $30 \mu\text{W}$.

3.2.3.1 Optical Setup

The measurement setup Figure 3.16 is modified from that for the RS measurement setup by removing the polarizer and analyzer and by changing the light source. A Quantum Gem 532 nm diode pumped solid state (DPSS) laser capable of producing 500 mW of power with 28 pm linewidth is used to pump the silicon. The laser passes through a variable beam expander (LINOS 2x-8x 532 nm) to adjust the beam diameter such that it fills the back aperture of the 20x Mitutoyo infinity corrected objective to obtain spot size close to the diffraction limit ($d = \frac{\lambda}{2NA} = \frac{532}{2 \times 0.42} = 633 \text{ nm}$). The laser passes through a 1000 nm dichroic beamsplitter and is focused onto the sample mounted in a liquid nitrogen cryostat (Linkam HFS350EV-PB4) with thermal grease (Apiezon-N) to ensure good thermal contact. The PL emission is collected by the objective and the reflected pump light (<1000 nm) is filtered off by the dichroic beamsplitter. The PL signal passes through a Raman ultrasteep long-pass edge filter (Semrock LP03 532RE 25) to further reduce the 532 nm pump signal and is focused onto the input slit of the spectrometer. The detector integration time is set to 1 second to allow the signal to be optimized, then it is increased to 10 s to take the spectrum.

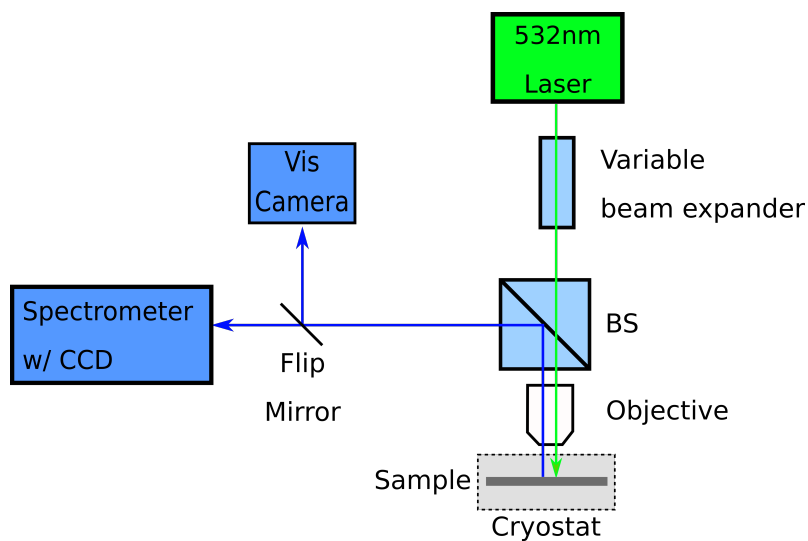


Figure 3.16: Schematic diagram of silicon photoluminescence setup.

3.2.3.2 Measurements

Measurements of Ln-type photonic crystal cavities were made in the 1050-1200 nm window where silicon emits. The 532 nm laser was set to produce 20 mW of power on the sample and the laser spot focused to the center of the cavity. A 10 second integration of the spectrum was captured using the 150g/mm grating for L3, L5, L7 and L9 cavities with period $a = 310$ nm (Figure 3.17).

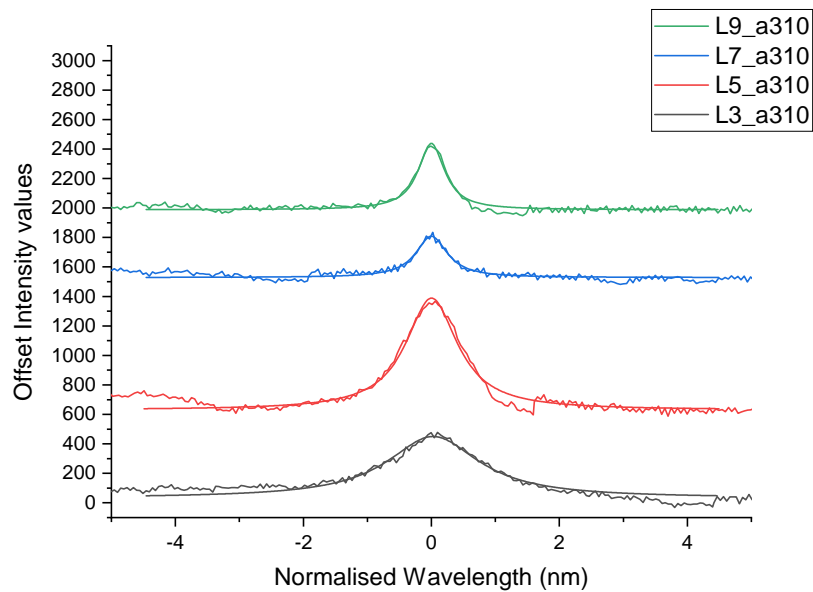


Figure 3.17: Stacked spectra of L3, L5, L7 and L9 cavities with period $a = 310$ nm plotted on a normalised wavelength scale. Lorentzian lineshapes are fitted to the cavity peaks.

Due to the high power density of the excitation laser spot of 500 MW/cm^2 , sample heating and free carrier generation can occur. As refractive index is a function of both temperature and carrier density [60, 61], small shifts in resonant wavelength of the cavities can be expected at high pump powers.

The strong cavity peak between 1120-1130 nm was analyzed by fitting a Lorentzian lineshape for each of the cavity lengths and Q -factors calculated from $Q = \lambda_0/\Delta\lambda$. Figure 3.18 shows an increase in Q -factor with cavity length. The Q -factor increases with cavity length as the main loss mechanism is the reflections at either end of the cavity. The longer the propagation length in the

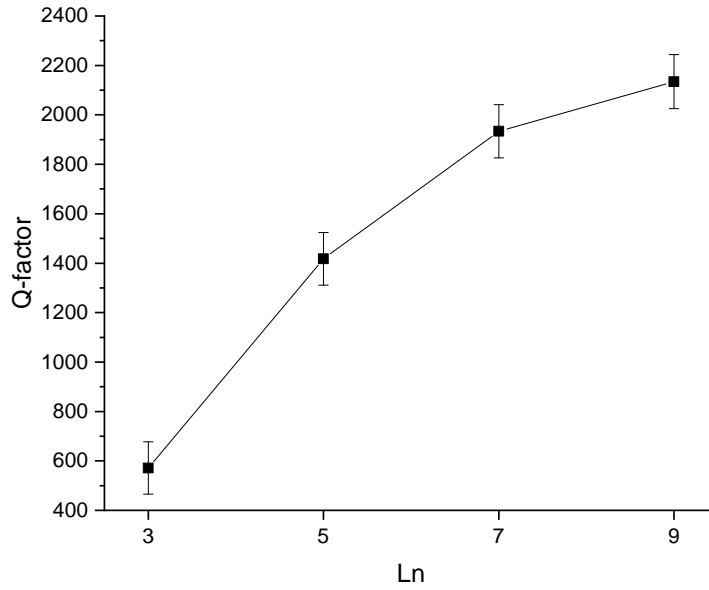


Figure 3.18: Plot of the quality factor of the resonance with respect to cavity length L_n for L3, L5, L7 and L9 cavities.

cavity, the more optical cycles can be fit between loss events. Remembering that Q -factor is defined as energy stored divided by energy lost per optical cycle, Q must increase. However, the Q -factor increase begins to reduce for the L9 cavity, this is due to the propagation loss beginning to become a significant loss mechanism. The propagation loss is due to fabrication imperfections such as sidewall roughness in the etched holes and variation in hole radii.

3.2.4 Summary

The photonic crystal cavities that were fabricated by myself in Section 3.2 were characterised optically in this section. The cavity resonances were measured in several different ways, resonant scattering with broadband light sources, a tunable laser, and using the photoluminescence of silicon generated within the cavity itself. While the fabricated cavities did not have a high Q -factor, they are sufficient for integration with 2D TMD gain material.

4 2D Materials

This chapter details the work carried out to produce few-layer MoTe₂ flakes to act as a gain layer in an eventual MoTe₂ PhCC laser. To yield thin layers of 2D materials such as MoTe₂ there are two main approaches. One can start with a bulk single crystal and exfoliate flakes in a top-down methodology or grow thin layers of 2D material in a bottom-up approach. These two methodologies are discussed in this chapter. The structures of both exfoliated and CVD MoTe₂ are investigated by a range of structural characterisation techniques. The optical properties of these materials are characterised by photoluminescence at room temperature and at cryogenic temperatures.

4.1 Exfoliation of Molybdenum Ditelluride

The bulk MoTe₂ single crystal was supplied by HQ Graphene in the 2H phase. In the 2H phase MoTe₂ is semiconducting with an indirect bandgap. As the number of layers approaches a monolayer, however, 2H-MoTe₂ undergoes a transition to a direct bandgap and the photoluminescence dramatically increases [62]. To produce few-layer flakes and areas of monolayer MoTe₂, flakes are exfoliated from the bulk crystal using the "scotch tape" method pioneered by Geim and Novosolov [63] in the production of graphene. The initial thick flake is exfoliated from the crystal by placing the crystal on a strip of scotch tape and peeling the tape off of the crystal. The flake is then thinned by placing another strip of scotch tape on the initial flake and peeling it off. This procedure is repeated 6-8 times to produce few-layer MoTe₂ flakes. The final strip of tape is inspected under an optical microscope to identify possible few layer MoTe₂ flakes. Once a target flake is identified, it is transferred to a square of PDMS (Gel-Pak Gel-Film) where the flake preferentially adheres to the

PDMS and is then peeled off the original scotch tape. The viscoelastic properties of PDMS prevent tearing of the flake during the transfer [64].

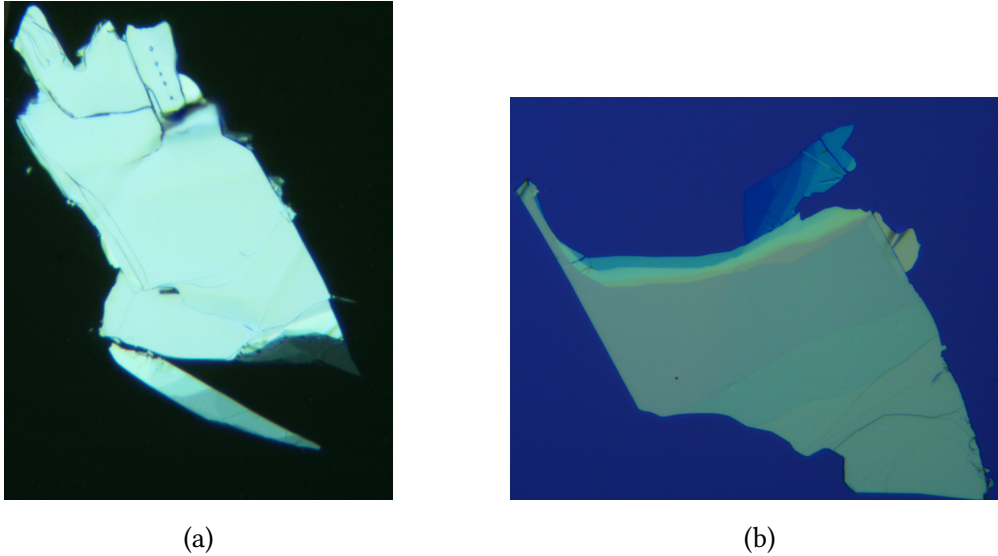


Figure 4.1: Optical microscope images at 50x magnification of (a) MoTe₂ flake on PDMS substrate and (b) MoTe₂ flake on 300 nm SiO₂-on-Si substrate.

The flake on PDMS is inspected under an optical microscope and a PL spectrum taken to ascertain the number of layers. The PL procedure will be explained in more depth in Section 4.4. The optical contrast of the flake with respect to the substrate can be enhanced by transferring the flake to a SiO₂-on-Si substrate with a 300 nm SiO₂ layer. The thin film interference of white light from the microscope illumination causes the SiO₂-on-Si substrate to have a deep purple colour which makes identification of thin areas of the flake easier (see Figure 4.1). While this can be a useful technique to characterize a flake, it is preferred to leave the flake on the PDMS stamp if it is to be subsequently transferred onto a device. Figure 4.2 shows a linescan through the few layer MoTe₂ flake from Figure 4.1. Fitted red lines show the average green channel pixel value for each layer in the sample. The numbers of layers of MoTe₂ are determined from the contrast between the substrate and each layer [65, 66].

To transfer a flake from the PDMS stamp onto a device, a home built 2D flake transfer system is used. This was designed by Dr Yue Wang with assistance from myself. A schematic of the dry transfer method is presented in Figure 4.3. The microscope has a 20x Mitutoyo long working distance objective fitted to a zoom lens with an illumination port. The illumination is provided by a tungsten halogen lamp connected to the microscope with a liquid light guide to reject unwanted heat.

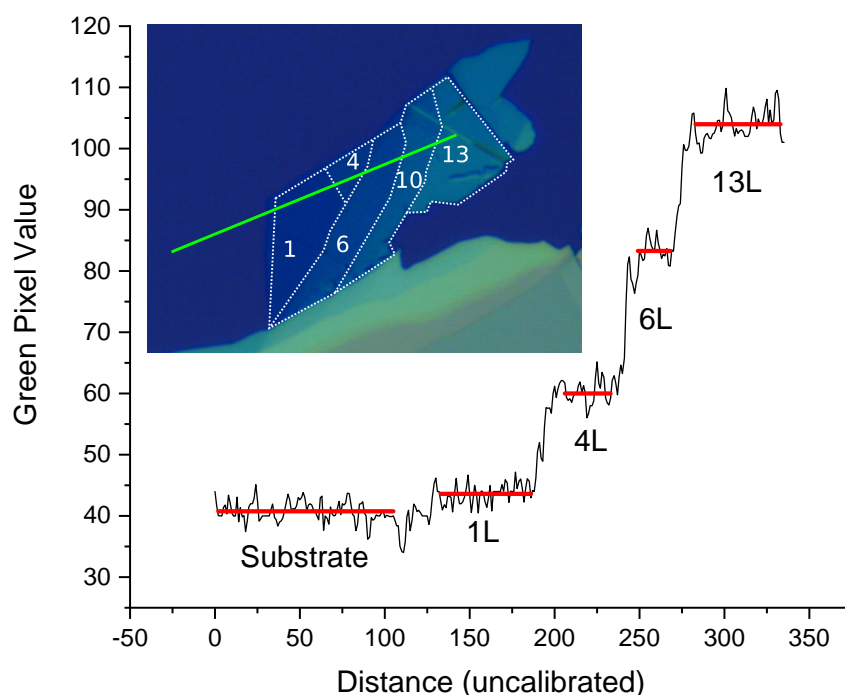


Figure 4.2: Inset: Optical contrast image of MoTe₂ flake from Figure 4.1(b). The layers of flake are outlined using a dashed line with number of layers annotated. Graph: Linescan (green line in inset) of green pixel values. Linear fits to pixel value with associated number of layers determined by a linear fit to average pixel values for each step.

Above the zoom lens a colour CCD camera with eyepiece lens is used to form the image. A zoom lens is particularly useful as the relatively low magnification of the 20x objective allows for the flake/device to be found, then the image can be optically zoomed to provide higher positioning accuracy. Using a zoom lens rather than several objectives on a rotating turret removes the position error of the flakes due to the tolerance on concentricity associated with a moving turret. Turret concentricity would cause the flake to appear in different positions on the monitor when changing between objectives, which can be a challenge particularly when using high magnification objectives as the flake may not be visible in the field of view. The flake transfer procedure is as follows. The substrate which the flake is to be transferred to is mounted on a 3-axis microblock stage with a heat pad below it. The PDMS stamp is stuck to a glass slide ensuring there are no bubbles under the stamp. The glass slide is fitted to a holder on a flip stage that is connected to a vertical translation stage mounted on another 3-axis microblock.

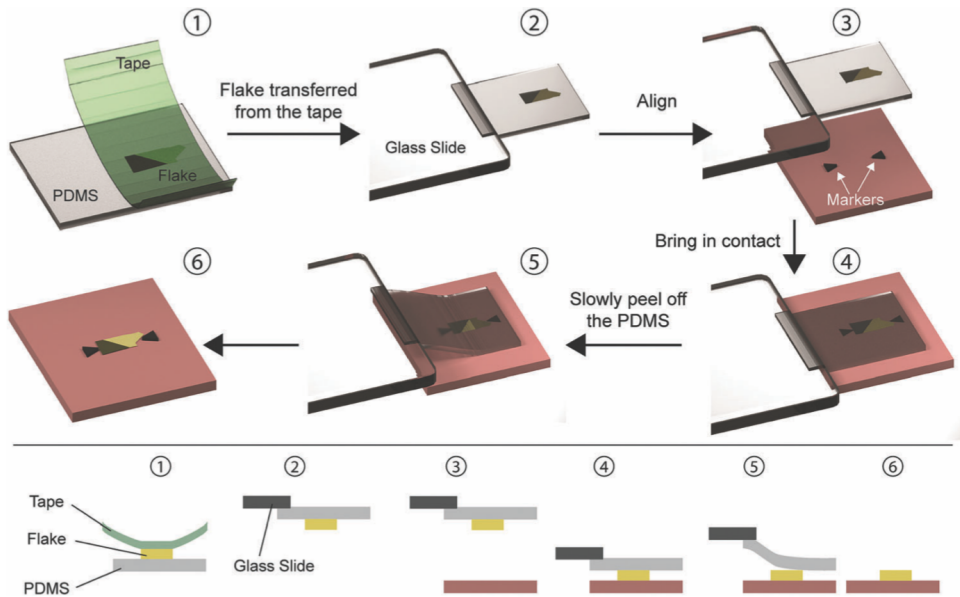


Figure 4.3: The PDMS dry transfer method. The flake to be transferred is exfoliated onto a PDMS stamp (1) and the stamp is then attached to a glass slide connected to a micromanipulator (2). Using a microscope, the flake can be aligned with the final substrate (3) and brought in contact (4). By slowly peeling of the PDMS stamp (5), the flake can be deposited on the substrate (6). Figure reproduced from Ref. [67].

The microscope is mounted on a coarse 2-axis stage to be able to translate the field of view of the microscope. The whole objective, zoom lens and camera assembly is mounted to the microscope post with a z-axis linear stage to control the focus of the microscope. See Figure 4.4 for an image of the 2D material transfer system.

To be able to transfer the flake precisely onto a device it is necessary to ensure that both the flake and the device lie on the same axis. First the device is found using the microscope xy-axis translators and its position marked on the monitor. The microscope is moved upwards and the flake flipped in under it. The microscope is focused through the slide and the PDMS stamp to image the flakes and the target flake identified. Note that the flake will appear reversed as we are imaging from the other side. The flake is brought inline with the marker on the monitor. The z height of the flake is lowered until it is close to the surface of the device whilst maintaining the microscope in focus with the flake. When the flake is close to making contact, the microscope is focused through the flake to bring the device in focus. The flake is then very slowly lowered into contact with the device. The stamp will have a slight angle to the device so that one side makes contact before the other. This will appear as a contact line moving across the

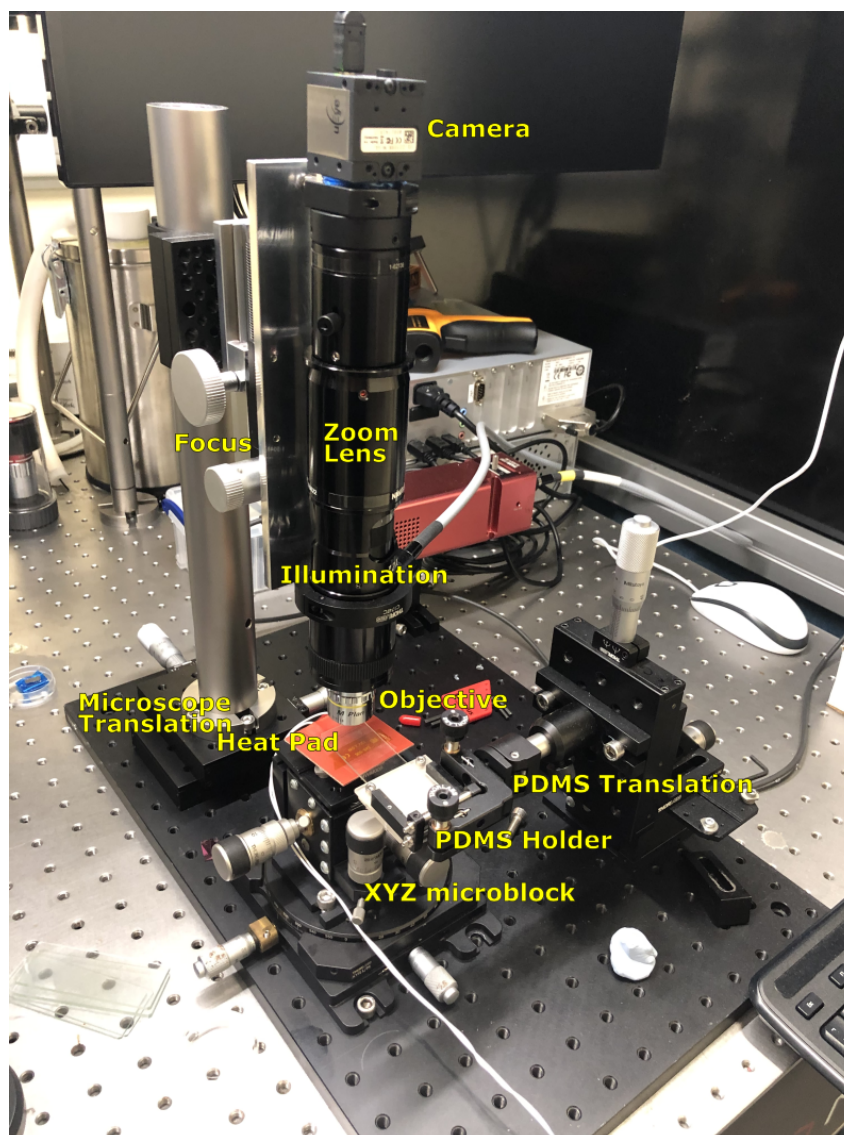


Figure 4.4: Photograph of the York 2D material transfer system designed by Dr Yue Wang.

monitor screen as more of the PDMS stamp makes contact with the substrate. As the contact line approaches the device it is imperative that the stamp is lowered very slowly so that any air bubbles below the flake are pushed out and the flake makes full contact with the substrate. The stamp is then lowered further to apply slight pressure to the flake to ensure adhesion. The sample stage is heated to $\sim 80^{\circ}\text{C}$ which helps release the flake from the PDMS stamp [68]. The PDMS stamp is then slowly peeled off of the substrate with the microblock and after the contact line clears the device the substrate is checked to see that the transfer was successful. Typical exfoliated flakes are 10-20 μm with areas of mono/bilayer of 2-5 μm .

4.2 CVD growth of Molybdenum Ditelluride

CVD growth of MoTe_2 was performed by the group of Alexey Ganin at the University of Glasgow. Their group investigates the use of 2D tellurides as catalysts to liberate H_2 [69, 70]. We partnered with them to see if it was possible to grow large area optical quality 2H- MoTe_2 films by chemical vapor deposition (CVD). Large areas of exfoliated 2D material are difficult to produce and are not (yet) viable for technological use. Another benefit of a CVD process is that it may be possible to grow the MoTe_2 directly on the device which is an attractive prospect for industrial applications. Ganin's group is interested in the properties of the 1T polymorph of MoTe_2 that has an octahedral structure, or disordered octahedral structure for the 1T' phase, and is semimetallic [71]. The semimetallic properties of the 1T phase allows electrochemical reactions to be performed. Whereas, the 2H polymorph of MoTe_2 has a trigonal prismatic structure and is semiconducting and optically active. The 2H and 1T' polymorphs are illustrated in Figure 4.5.

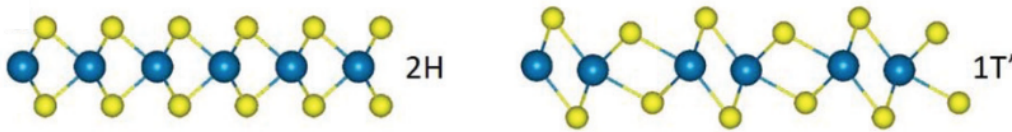


Figure 4.5: 2H and 1T' polymorphs of MoTe_2 . Circles in blue represent molybdenum atoms and circles in yellow represent tellurium atoms. Figure reproduced from Ref. [72].

4.2.1 Molybdenum Ditelluride CVD Procedure

The substrates were diced using a diamond tipped scribe from a wafer of 300 nm SiO_2/Si (100) (Inseto) to a size of $10 \times 10 \text{ mm}^2$. The substrates were cleaned via ultrasonication in acetone and isopropyl alcohol, for 10 minutes in each solvent before being dried by a stream of dry nitrogen gas.

A layer of molybdenum (99.95%) was deposited on to the cleaned substrates via electron beam evaporation using a Plassys MEB550s. The deposition occurred at a pressure of 1×10^{-6} mbar with a deposition rate of 0.07 nm/s. The electron

beam gun emission current was 220 mA. The end point of the deposition of the molybdenum films was controlled by a quartz crystal microbalance to determine the layer thickness.

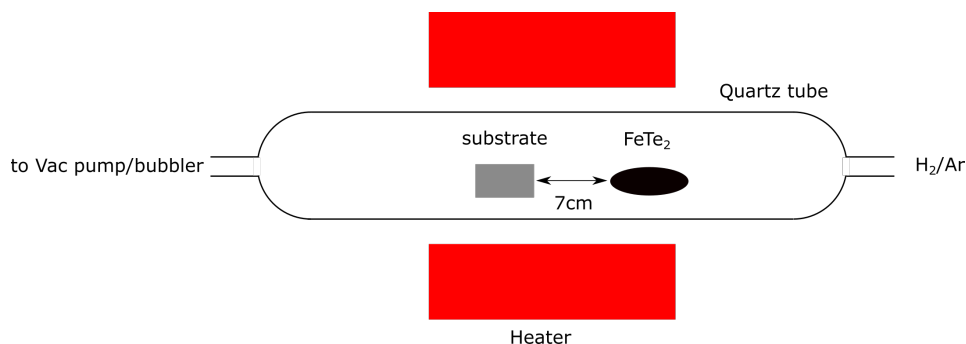


Figure 4.6: Diagram of CVD growth furnace.

The Mo/SiO₂/Si substrate was placed into the hot zone of a tube furnace with the FeTe₂ precursor placed 7 cm upstream in a quartz ampoule (this setup is shown in Figure 4.6). Before the beginning of the CVD process the furnace tube was evacuated to a pressure of 3×10^{-2} mbar before being flushed with the 5% H₂/Ar carrier gas. This process was carried out three times to ensure an oxygen-free environment for the deposition. The tube furnace was then set to 650 °C, ramping at 5 °C/min with a dwell time of 4 hours, before being allowed to cool to room temperature naturally. The flow rate of the 5% H₂/Ar carrier gas was set to 0.3 sL/min during the process.

A FeTe₂ precursor is used rather than a Te source as it allows for phase selectivity in the growth of MoTe₂. Other CVD procedures in the literature [73] use a Te precursor and then can select the phase of MoTe₂ by tuning the heating and cooling rates of their furnace. However this methodology can be difficult to repeat with different furnaces as the energy difference between the 1T and 2H phases is small. For 1T-MoTe₂, a MoO₃ layer is first grown then processed in the furnace. For 2H-MoTe₂ a Mo layer is first grown then converted to MoTe₂ with a FeTe₂ precursor.

4.3 Structural Characterisation

To determine the structure of the exfoliated and CVD grown MoTe₂ a variety of structural characterisation techniques were performed. The inert Raman spectroscopy and XRD were conducted by James Fraser from Dr Alexey Ganin's group at University of Glasgow. TEM imaging was performed by Dr Jon Bernard at the York JEOL Nanocenter with sample preparation of TEM grids by Dr Yue Wang. Analysis of structural characterisation results was performed by Lewis Reeves.

4.3.1 Raman Spectroscopy

Raman spectroscopy is a technique that uses a monochromatic light source, such as a narrow band laser, to determine the vibrational modes of molecules within a material. The photons elastically (Rayleigh) and inelastically (Raman) scatter from the molecules within the sample either gaining or losing energy for the case of Raman scattering. If the scattered photon wavelength is longer than that of the excitation photon, the corresponding wavelength shift is referred to as a "Stokes" shift. Conversely, if the scattered photon has a shorter wavelength, the frequency shift is referred to as an "anti-Stokes" shift. The energy transitions for Raman scattering are shown as a Jablonski diagram in Figure 4.7.

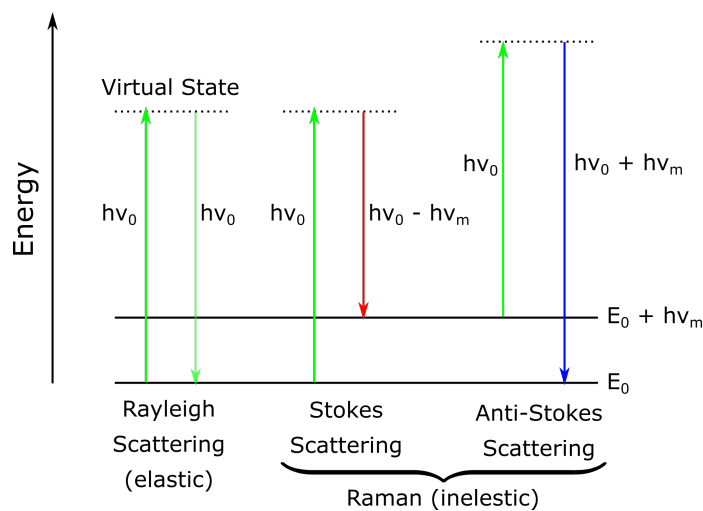


Figure 4.7: Jablonski diagram representing energy transitions for Rayleigh and Raman scattering.

The scattered light is analysed using a spectrometer with a narrow notch filter at the excitation wavelength to filter out the laser and the Rayleigh scattered light as the Raman scattered signal is very weak, typically $10^{-5}\%$ of the scattered light. The inelastically scattered photons are characteristic of the molecular bonds, making this a useful technique to determine the bonding of molecules which can allow for the determination of the phase of 2D materials.

Raman spectra of the CVD grown 2H-MoTe₂ were obtained in an inert atmosphere to prevent oxidation of the MoTe₂ flakes with a Renishaw inVia confocal Raman microscope and a 532 nm excitation laser. The characteristic Si Raman peak at 520 cm^{-1} was used to calibrate the system. The strong E_{2g}^1 peak at 235 cm^{-1} shown within Figure 4.8 is characteristic of the 2H phase of MoTe₂.

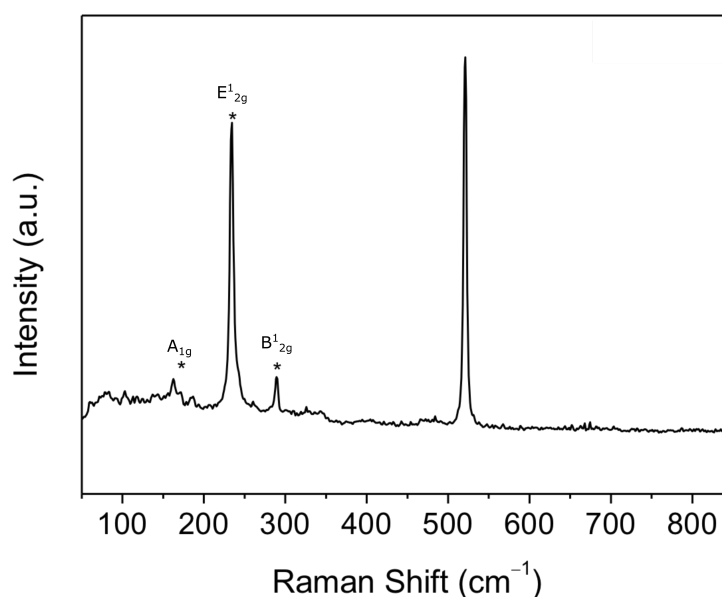


Figure 4.8: Raman spectrum performed under inert atmosphere of unoxidized CVD 2H-MoTe₂. Figure courtesy of James Fraser University of Glasgow.

Comparing the Raman spectrum in Figure 4.8 to work by Tan et al. [72], who investigated the 2H-1T' phase transition in MoTe₂, we can see that the characteristic Raman peak of 1T'-MoTe₂ is at 125 cm^{-1} (see Figure 4.9). The 1T' phase peak is absent in the Raman spectrum of the CVD grown material. In the point measurements that were taken only the 2H phase exists.

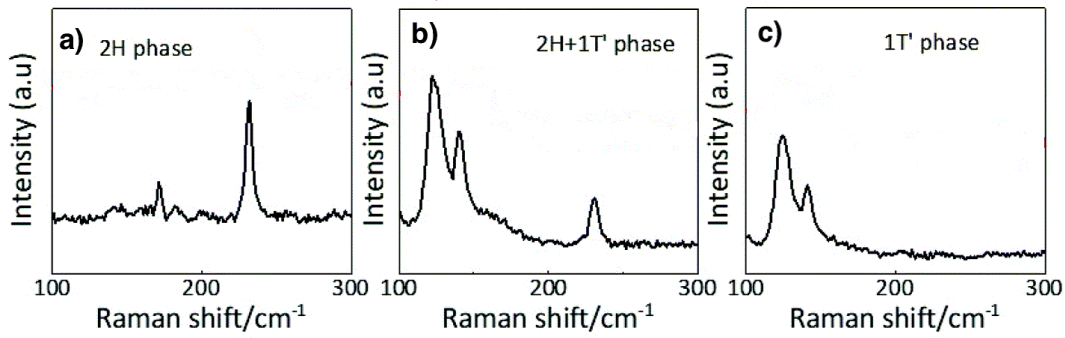


Figure 4.9: Raman spectra of (a) 2H-MoTe₂ (b) 2H+1T'-MoTe₂ (c) 1T'-MoTe₂. Figure reproduced from Ref. [72].

Another use of Raman spectroscopy with MoTe₂ is the identification of monolayers. Ruppert et al. [14] show that the B_{2g} Raman peak at 289 cm⁻¹ appears in few-layer MoTe₂ flakes but is absent in monolayer MoTe₂.

4.3.2 X-Ray Diffraction

Another method for determining the structure of a crystal is to use X-Ray Diffraction (XRD) [74]. XRD uses monochromatic X-rays such as Cu-K_{α1} X-rays with a wavelength of 0.154 nm. To produce the X-rays, a tungsten cathode generates an electron beam that is accelerated to bombard a copper anode. The electrons interact with the copper anode causing the emission of X-rays. The X-rays that are generated are not monochromatic with Cu-K_β, W-L_{α1}, W-L_{α2}, Cu-K_{α1} and Cu-K_{α2}. A nickel filter can be used to remove Cu-K_β, W-L_{α1} and W-L_{α2}. To isolate the Cu-K_{α1} X-rays, a germanium monochromator is used in a 2-bounce configuration. The monochromator is aligned such that only Cu-K_{α1} passes. A $\theta - 2\theta$ measurement (see Figure 4.10) is used to determine structures where the planes are parallel to the sample, such as with 2D materials.

The incident X-ray beam at angle θ and the detector at angle 2θ are scanned symmetrically maintaining the scattering vector \mathbf{K} perpendicular to the sample surface. The diffraction of X-rays off of the crystal's planes is governed by Bragg's Law $n\lambda = 2d \sin\theta_B$ where n is the diffraction order, λ is the X-ray wavelength, d is the lattice plane spacing and θ_B is the angle where diffraction occurs. By maintaining \mathbf{K} perpendicular to the sample surface, the Bragg condition is met for

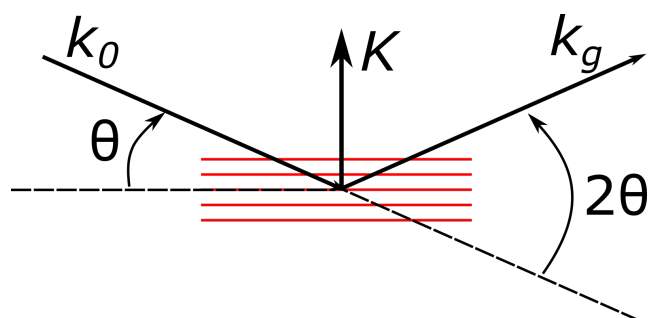


Figure 4.10: The $\theta - 2\theta$ XRD measurement geometry. Crystal planes are shown in red. The x-ray beam k_0 and detector k_g are scanned simultaneously maintaining \mathbf{K} perpendicular to the crystal planes.

planes parallel to the surface. It is then possible to determine the crystallographic orientation and the lattice constant from such a $\theta - 2\theta$ measurement.

Figure 4.11 is a $\theta - 2\theta$ XRD spectrum of a bulk 2H-MoTe₂ single crystal orientated along the (001) plane using a Bruker D8 Venture provided by HQ Graphene. The four XRD peaks correspond to (00i) with $i = 2, 4, 6, 8$.

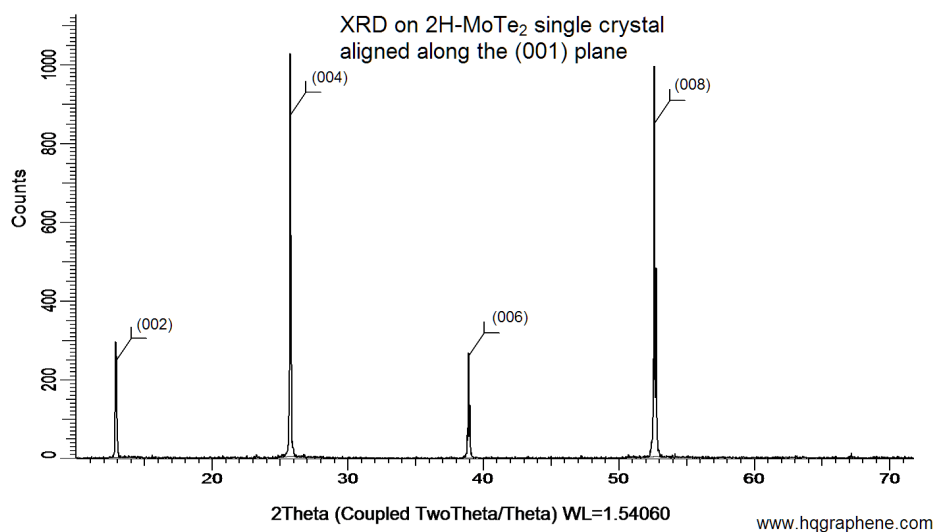


Figure 4.11: $\theta - 2\theta$ XRD spectrum of 2H-MoTe₂ bulk crystal provided by HQ Graphene.

Figure 4.12 is a $\theta - 2\theta$ XRD spectrum of CVD grown 3.5 nm 2H-MoTe₂ orientated along the (001) plane. The four XRD peaks correspond to (00i) with $i = 2, 4, 6, 8$ at angles $2\theta^\circ = 12.9, 25.7, 38.9, 52.5$. The narrow XRD peak at 34° is likely to be from the (100) orientated silicon SOI wafer the MoTe₂ was grown on. The CVD MoTe₂ peaks are broadened compared to that of the bulk single crystal

(see Figure 4.11). The broadening of an XRD peak occurs with a decrease in crystallite size as the destructive interference that occurs either side of the Bragg angle is a summation of all of the diffracted beams, and close to the Bragg angle a large number of crystal planes are required to produce destructive interference. This effect is equivalent to reducing the number of periods in a distributed Bragg reflector which broadens the spectral response. Three conclusions can be drawn from this, namely a) the crystallites are small and we have a polycrystalline film, b) the film is very thin and there are few planes available to diffract from, or c) a combination of both of these effects. Therefore, further characterisation is required to resolve this question.

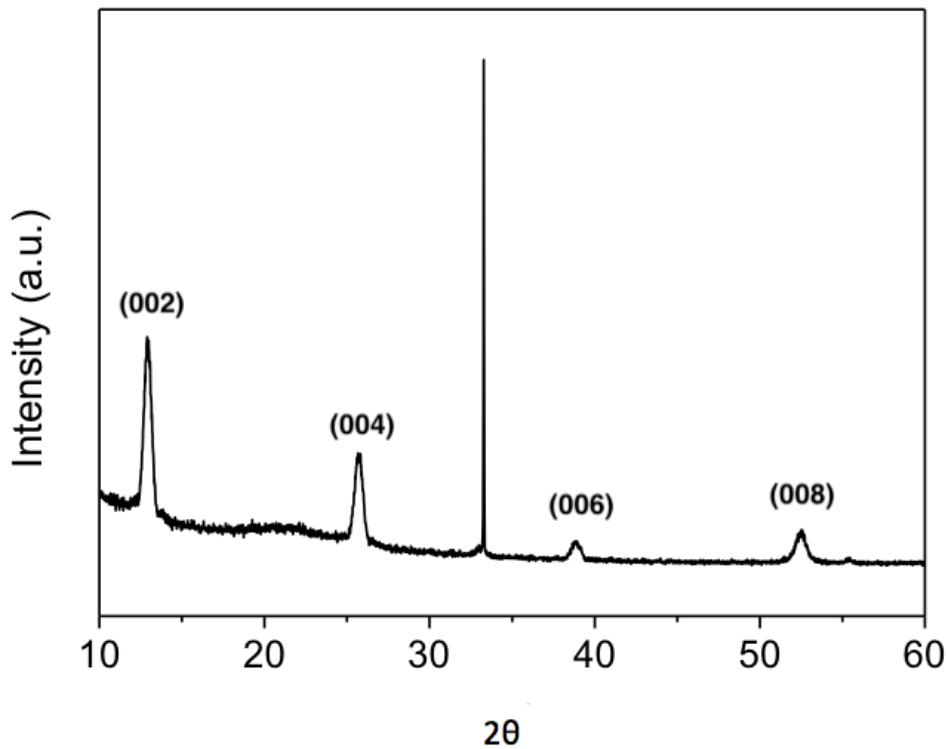


Figure 4.12: $\theta - 2\theta$ XRD spectrum of 3.5 nm CVD 2H-MoTe₂ on (100) cut SOI. XRD conducted by of James Fraser at University of Glasgow.

4.3.3 Transmission Electron Microscopy

A Transmission Electron Microscope (TEM) is a powerful instrument to examine materials at the atomic scale. A high energy beam of electrons of the order of 200 kV is accelerated towards a thin sample where the electrons interact with the sample. To image with a TEM, there are two main modes depending on

how the electrons interact with the sample. The electrons can either travel through the sample and be directly detected or be diffracted off crystal planes within the sample analogously to XRD. Then either a real-space image of the sample can be formed, or by placing the selected-area diffraction (SAD) aperture into the TEM column, a diffraction pattern in reciprocal space can be formed. A diagram of the two imaging modalities of a TEM is presented in Figure 4.13.

4.3.3.1 Imaging

Real space images of the sample can be formed by placing the objective aperture at the back focal plane of the objective lens. The objective aperture can either select the directly transmitted electrons (bright-field) or the diffracted electrons (dark-field). In bright-field imaging, the contrast in the image is due to the absorption of electrons by the sample. Areas will appear darker where the sample is thicker or contains elements with high atomic numbers Z . A dark-field image is formed when the direct electron beam is blocked and the diffracted electrons are imaged. Areas where there is no diffraction appear dark and areas where electrons are diffracted appear bright. Dark-field imaging is useful for imaging the crystallinity of a sample.

4.3.3.2 Selected-area Diffraction

A TEM can produce a diffraction pattern by removing the objective aperture and replacing it with the SAD aperture at the back focal plane. The SAD aperture allows the area of interest in the image to be selected and the diffraction pattern to be projected onto the screen. In the SAD pattern, there is always a bright central spot due to the undiffracted electrons that travel straight through the sample. The diffraction pattern that surrounds the central spot is similar to the diffraction pattern of an XRD as both represent the angles where the Bragg condition is met; the intensity decreases as θ increases. The sample is able to be $x - y$ positioned and tilted to select different areas and different diffraction planes. Exemplar SAD patterns from Ref. [75] are shown in Figure 4.14. Diffraction from an amorphous material such as amorphous carbon (see Figure 4.14(a)) leads to a blurred diffraction pattern. Diffraction from a single crystal,

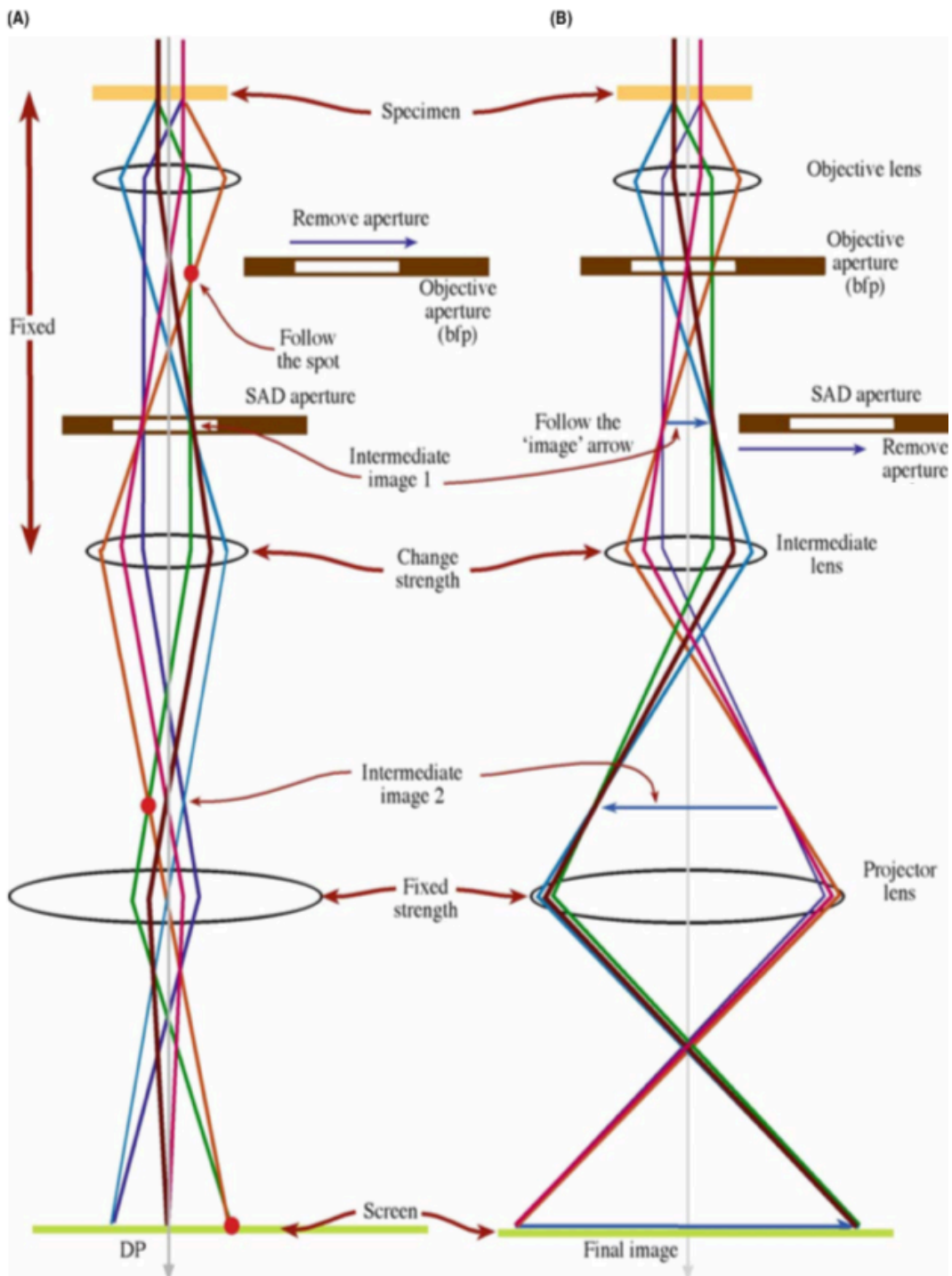


Figure 4.13: The two basic operations of the TEM imaging system involve (A) diffraction mode: projecting the diffraction pattern (DP) onto the viewing screen and (B) image mode: projecting the image onto the screen. In each case the intermediate lens selects either the back focal plane (BFP) (A) or the image plane (B) of the objective lens as its object. Figure reproduced from Ref. [75].

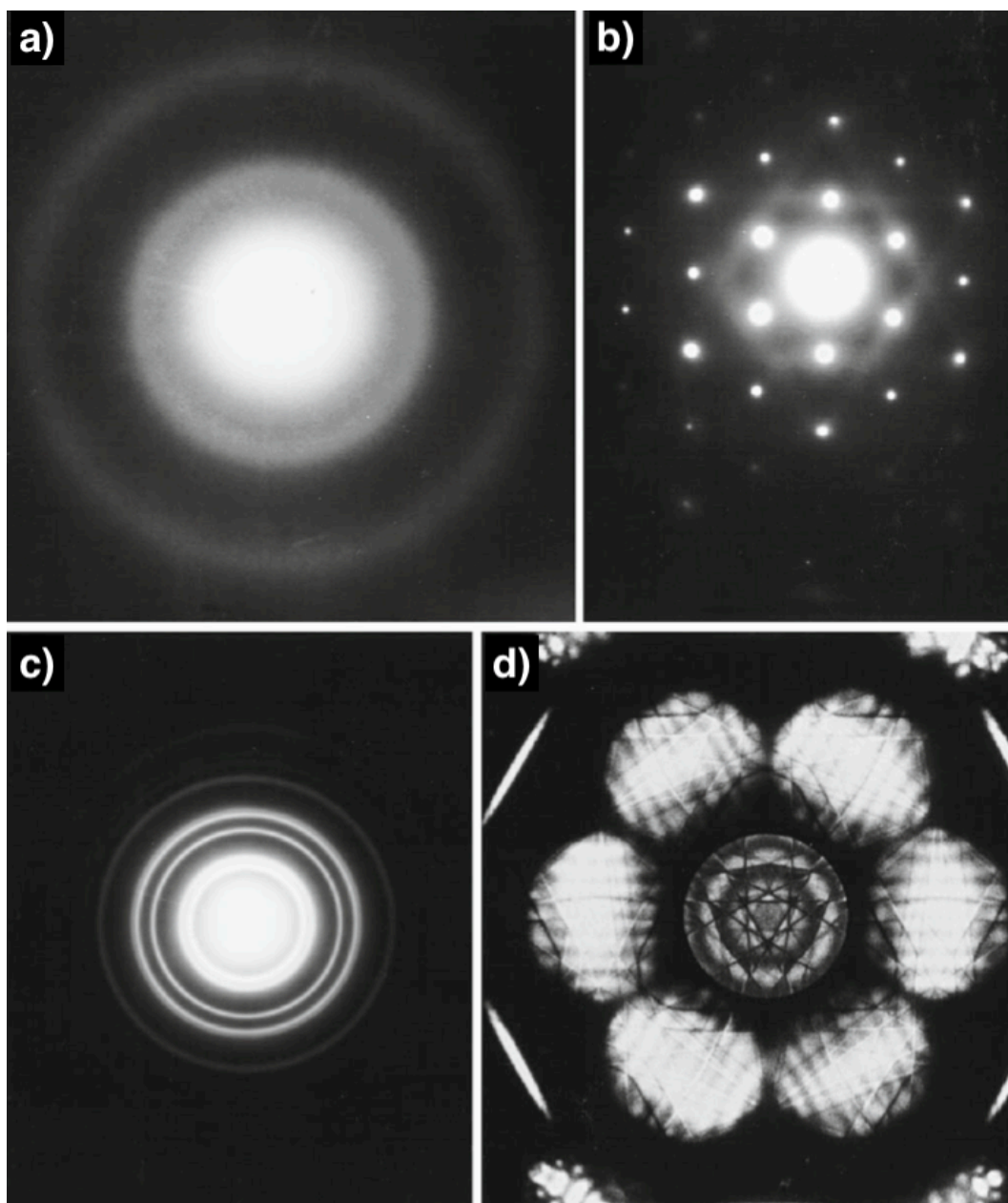


Figure 4.14: Several kinds of DPs obtained from a range of materials in a conventional 100-kV TEM: (a) amorphous carbon, (b) an Al single crystal, (c) polycrystalline Au, (d) Si illuminated with a convergent beam of electrons. In all cases the direct beam of electrons is responsible for the bright intensity at the center of the pattern and the scattered beams account for the spots or rings that appear around the direct beam. Figure reproduced from Ref. [75].

such as an Al single crystal (see Figure 4.14(b)) produces a diffraction pattern with discrete spots corresponding to each satisfied Bragg condition. Diffraction from a polycrystalline material such as polycrystalline Au (see Figure 4.14(c)) produces discrete rings in the diffraction pattern if the grains are randomly orientated. This can be thought of as a rotation of the single crystal diffraction smearing the spots into rings due to the many crystal orientations.

As the electrons are accelerated to 200 kV in the JEOL TEM 2011 system, it is important to note that they need to be considered relativistically when calculating their wavelength. For a 200 kV electron beam, the classical wavelength ($\lambda_e = \frac{h}{\sqrt{2eVm_e}}$) is 2.73 pm and the relativistically corrected wavelength ($\lambda_e = \frac{hc}{\sqrt{(eV)^2 + 2eVm_e c^2}}$) is 2.51 pm.

4.3.3.3 Exfoliated Molybdenum Ditelluride

Flakes of 2H-MoTe₂ were mechanically exfoliated from a bulk crystal and transferred to a TEM sample grid with a carbon support film. The flake was then imaged in bright-field (see Figure 4.15(a)) and dark-field (see Figure 4.15(b)) modes. The ripples seen in the dark-field image are due to the flake not sitting perfectly flat on the carbon film after transfer.

A SAD diffraction pattern was obtained from the exfoliated 2H-MoTe₂ (see Figure 4.16(a)). The hexagonal pattern of spots indicates a trigonal prismatic structure, i.e the 2H phase, that is a single crystal. A 1T phase sample would consist of the same hexagonal diffraction spots with extra spots at 30° angular spacing with respect to the hexagonal spots [76].

High Resolution TEM (HR-TEM) images were also taken of the exfoliated 2H-MoTe₂ to examine the lattice structure of the sample (see Figure 4.16(b)). The lattice constant a was found to be 3.0 Å which is in agreement with HR-TEM measurements present within relevant literature [65, 77].

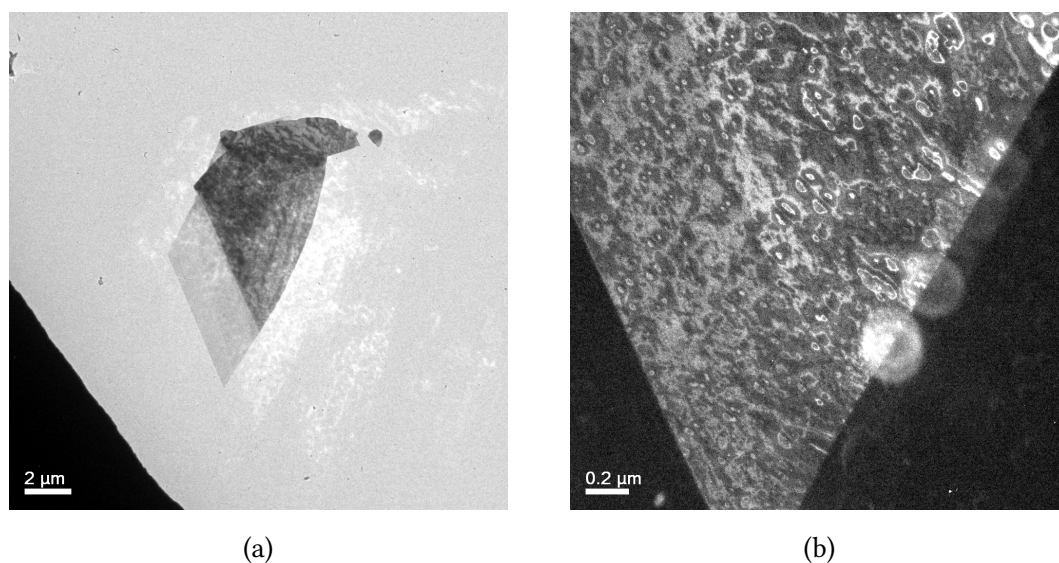


Figure 4.15: (a) Bright-field TEM image of a 2H-MoTe₂ flake. (b) Dark-field TEM image of the same 2H-MoTe₂ flake at higher magnification. TEM by Dr Jon Barnard.

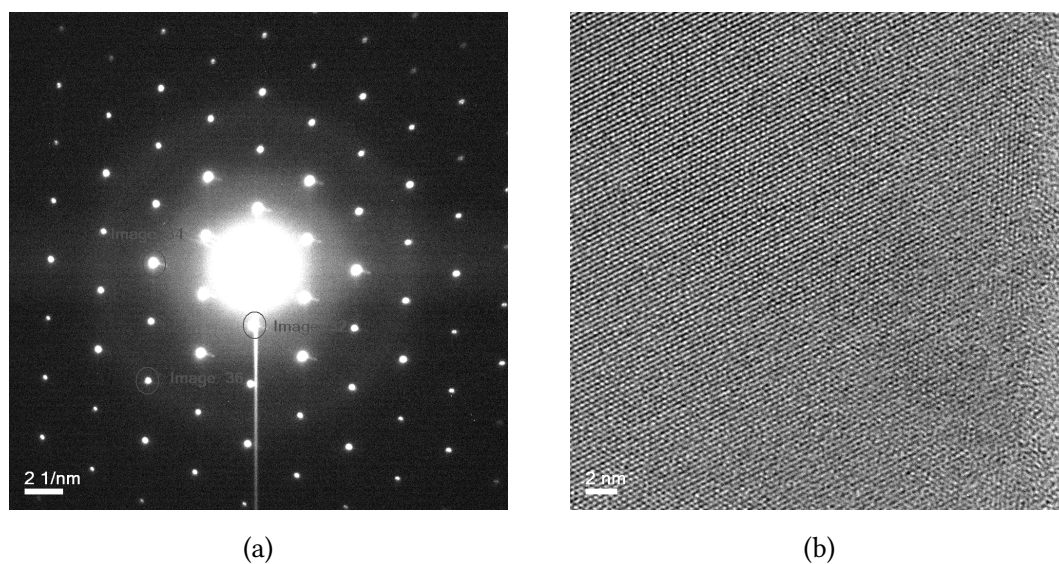


Figure 4.16: (a) SAD diffraction pattern of a 2H-MoTe₂ flake. (b) HR-TEM of a 2H-MoTe₂ flake. TEM by Dr Jon Barnard.

4.3.3.4 CVD Molybdenum Ditelluride

To prepare the CVD MoTe₂ sample, flakes were mechanically exfoliated from a 3.5 nm thick CVD grown 2H-MoTe₂ and transferred to a TEM grid with a holey carbon film. The carbon film supports the small MoTe₂ flakes and the holes allows for just the MoTe₂ flake to be characterised.

The bright-field images (see Figure 4.17(a)) show the transferred CVD MoTe₂ flake on the left hand side of the holey carbon TEM grid. The dark areas are where the flake is folded over on itself. The magnified bright-field image (Figure 4.17(b)) shows the flake suspended over one of the holes. The grain structure of the CVD grown MoTe₂ is visible as not all of the uppermost layer was transferred upon exfoliation. Therefore the CVD 2H-MoTe₂ is clearly polycrystalline.

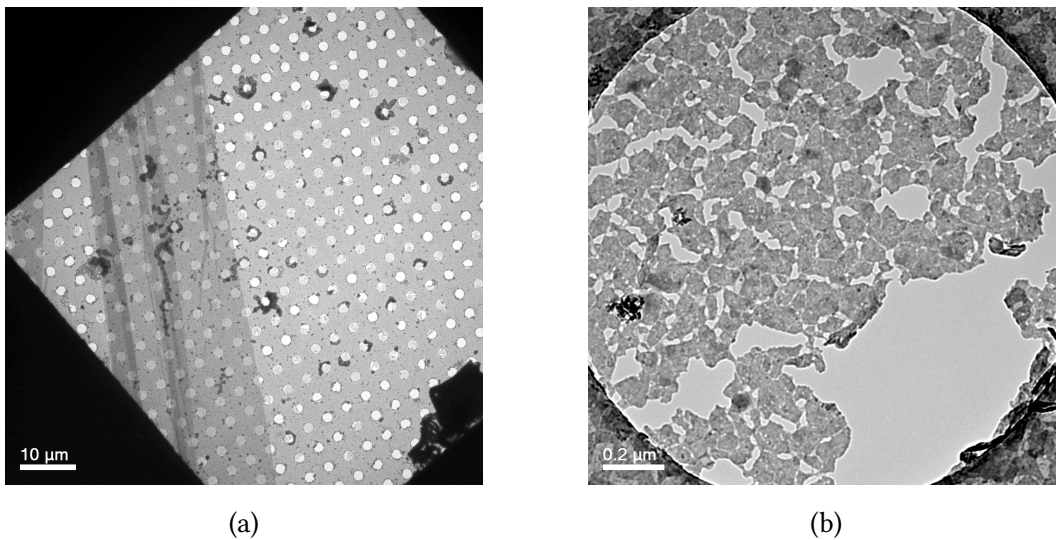


Figure 4.17: (a) Bright-field TEM image of CVD 2H-MoTe₂ flake. (b) Magnified bright-field TEM image of CVD 2H-MoTe₂ flake. TEM by Dr Jon Barnard.

A SAD diffraction pattern (Figure 4.18(a)) of the CVD sample was taken. Compared to diffraction spots observed from the single crystal MoTe₂ (Figure 4.16(a)) the diffraction rings from the CVD sample indicate that it is polycrystalline. As the diffraction rings are speckled the grain size is relatively large [75].

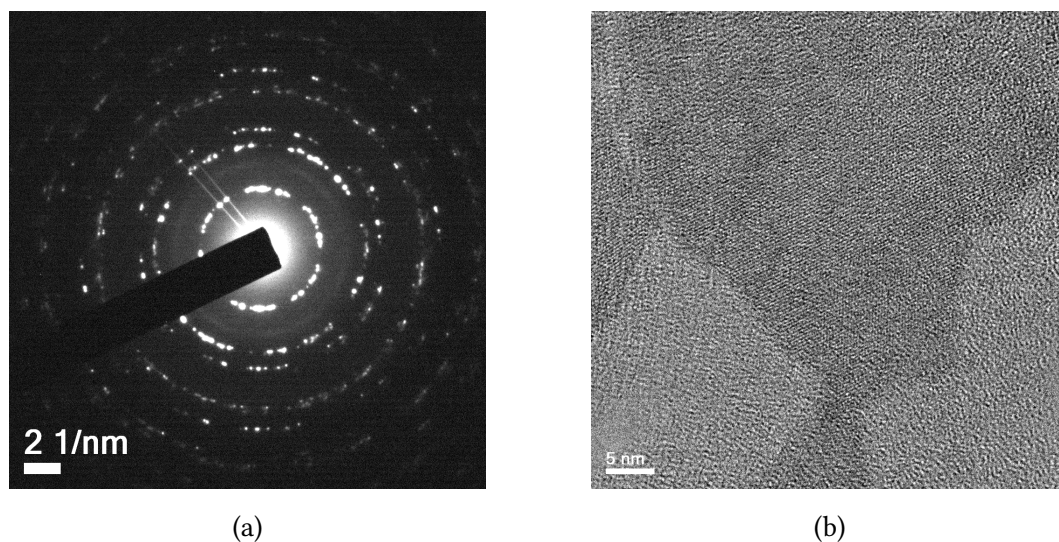


Figure 4.18: (a) SAD diffraction pattern of CVD 2H-MoTe₂ flake. (b) HR-TEM of CVD 2H-MoTe₂ flake. TEM by Dr Jon Barnard.

High Resolution TEM (HR-TEM) images were also taken of the CVD grown 2H-MoTe₂ to examine the lattice structure of the sample (see Figure 4.18(b)(b)). The lattice constant a was found to be 3.1 Å, which is in agreement with HR-TEM measurements in the literature [65, 77]. Grain boundaries are visible within the HR-TEM which further indicates the polycrystalline structure of the CVD MoTe₂.

4.3.4 Summary of Structural Characterisation Measurements

From the Raman spectroscopy, XRD and TEM analyses we can say that both the bulk exfoliated sample and the CVD grown sample are in the 2H phase. Although the Raman and TEM are point measurements, the large spot size of the XRD suggest that the 1T' phase does not exist in these samples. The exfoliated sample is single crystal as shown by XRD and TEM. The CVD sample is polycrystalline which was indicated as a possibility by XRD and confirmed by TEM.

4.4 Optical Characterisation

In addition to the structural characterisation of both the exfoliated 2H-MoTe₂ and CVD 2H-MoTe₂, optical characterisation is also required to identify viable monolayer and bilayer MoTe₂ flakes. Microphotoluminescence can characterise the number of MoTe₂ layers in a flake due to the stark difference in the PL spectrum between monolayer and bilayer flakes. To achieve this, it was necessary to design and build a microphotoluminescence setup and then optimize its performance to obtain PL spectra of MoTe₂. This process will be discussed in detail within this section.

4.4.1 Microphotoluminescence

Photoluminescence is the emission of light from a material following the absorption of photons. A photon with energy $h\nu > E_g$ is able to promote an electron from the valence band of a semiconductor to the conduction band, leaving a hole in the valence band. After the electron thermalizes to the conduction band edge it may recombine with the hole emitting a photon with energy close to $h\nu = E_g$. If a phonon is involved with the recombination, the emitted photon energy will be reduced by the phonon energy.

4.4.2 Design and Optimisation of Optical Setup

For a microphotoluminescence (μ PL) setup, an excitation source (laser), microscope and spectrometer are required. The laser needs to be able to provide a high quality single-mode beam to achieve a diffraction limited excitation spot. Clean-up optics such as a spatial filter can be used to provide a Gaussian beam from a multimode laser. The excitation laser should fill the back aperture of the microscope objective lens again to produce a diffraction limited spot. A Keplarian telescope can be constructed to expand the laser beam, or a variable beam expander can be used (particularly useful when several different microscope objectives are employed). To deliver the laser beam to the microscope, at least two mirrors should be used in a z-fold configuration to allow the beam to be

steered, centered and on the optic axis of the microscope. In this system, a dichroic mirror is used to deliver the excitation beam into the microscope.

A Thorlabs (DMLP1000R) longpass dichroic mirror with a 1000 nm cut-on wavelength is used as we are interested in spectroscopy $>1 \mu\text{m}$. The dichroic mirror provides $>90\%$ transmission for 1020-1550 nm and $>95\%$ reflection for 520-985 nm. The longpass dichroic mirror is mounted in a kinematic filter cube to allow easy modification for different wavelengths of interest. Infinity corrected objectives are used rather than finite conjugate objectives, as the infinity space behind the objective allows a parallel laser beam to be focused by the objective. Tube lenses are then used to form images from the objective at the camera and spectrometer. The spectrometer should have sufficient resolution to resolve the spectral features of interest and this feature will be discussed in more detail in this section. A diagram of our microphotoluminescence setup is shown in Figure 4.19.

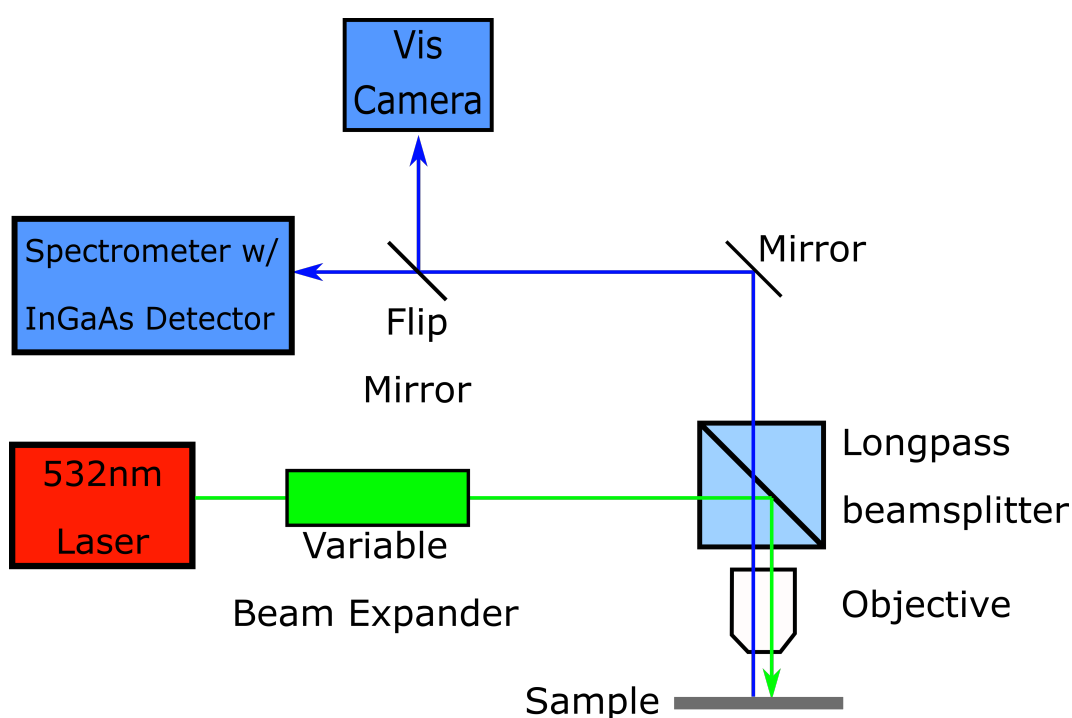


Figure 4.19: Diagram of microphotoluminescence setup built as a part of this PhD. A 532 nm laser is expanded by a beam expander then is focussed onto the sample using a long working distance objective. The photoluminescence is captured by the objective and the excitation laser is filtered by a longpass beamsplitter. The photoluminescence is analysed using a spectrometer with an InGaAs array detector.

4.4.2.1 Czerny-Turner Spectrometers

A Czerny-Turner spectrometer consists of two concave mirrors and a plane diffraction grating. Light is focused onto the input slit of the spectrometer. The input polychromatic light is then collimated by the input mirror and directed to fill the diffraction grating. The polychromatic light diffracts off of the grating as described by Bragg's law and is focused on the output slit or array detector of the spectrometer. The diffraction grating is mounted on a rotating turret that is used to vary θ allowing for selection of the wavelength that is centered on the output slit. Therefore, the Czerny-Turner spectrometer acts as a 1:1 imaging system. Figure 4.20 shows a schematic diagram of our Acton Research (now Teledyne Princeton Instruments) SpectraPro 2750 spectrometer.

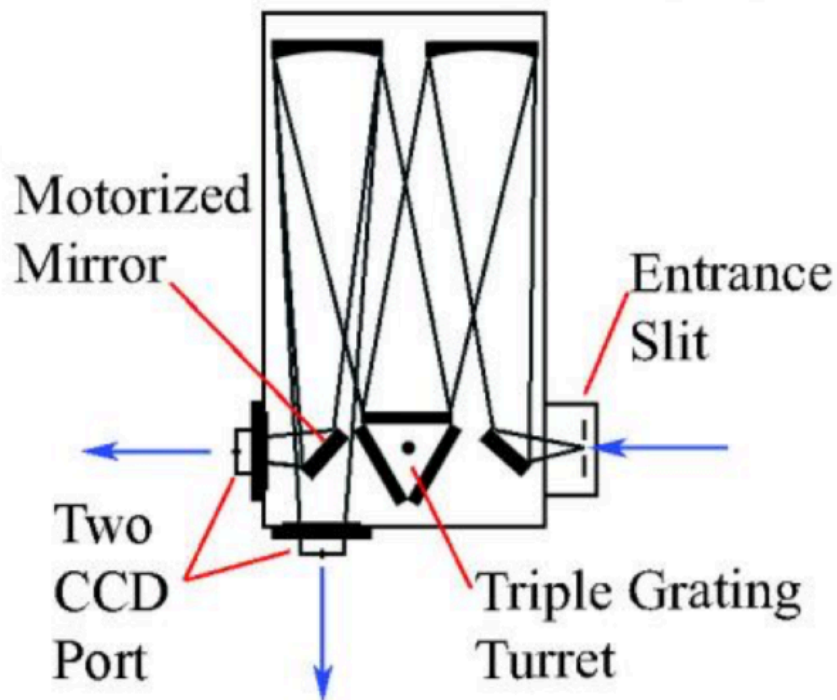


Figure 4.20: Diagram of Acton Spectrapro 2750 with dual CCD ports. Figure reproduced from Ref. [78].

4.4.2.2 Dispersion and Bandpass

The dispersion of a spectrometer is governed by the linespacing d of the grooves in the diffraction grating. Diffraction gratings for spectrometers are available with grooves/mm ranging from 50 g/mm to 3600 g/mm. The larger the number of grooves per mm a grating has, the higher the dispersion the grating will have. The bandpass of a spectrometer is a function of both the dispersion from the diffraction grating and the focal length f of the spectrometer. As the focal length increases, the bandpass of the spectrometer (for a given input slit size) decreases which leads to higher spectral resolution. The calculated resolution of spectrometers with varying focal lengths with 150, 600 and 1200 g/mm gratings are shown in Table 4.1. The resolution values are calculated assuming an input slit size of 25 μm and an output slit size/pixel size of 25 μm .

Table 4.1: Spectrometer resolution (nm) for C-T spectrometers with $f= 150, 300, 500, 750$ mm.

Grating grooves/mm	Spectrometer focal length f (mm)			
	150	300	500	750
150	2.52	1.27	0.52	0.31
600	0.57	0.3	0.13	0.08
1200	0.23	0.13	0.06	0.04

The triple grating turret allows 3 gratings to be installed. For this system, 150 g/mm, 600 g/mm and 1200 g/mm gratings were installed. The 150 g/mm grating allows for the greatest bandpass to be imaged onto the array detector. This is particularly useful for PL measurements where spectral features can be broad (100-200 nm). The 600 g/mm grating provides higher resolution but lower bandpass and so this grating is generally used for measuring spectral response of photonic crystals with low Q -factors. The 1200 g/mm grating provides the highest resolution and is used for Raman spectroscopy where the Raman peaks are spectrally close.

Another consideration when choosing a diffraction grating is the blaze angle. A blazed grating is designed to produce maximum diffraction efficiency in a specific diffraction order, minimizing the power lost to other orders that would decrease the throughput of the spectrometer. Rather than being ruled with symmetrical

grooves, a blazed grating is ruled at an angle γ with respect to the surface normal producing a sawtooth profile. A blazed grating is illustrated in Figure 4.21.

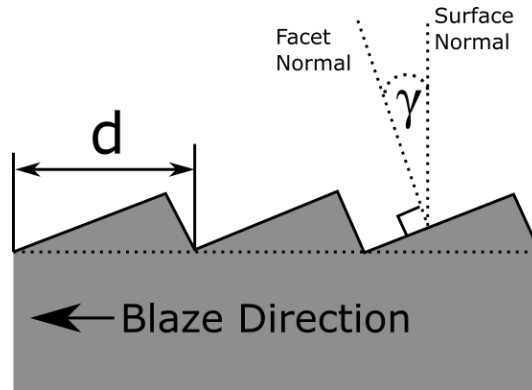


Figure 4.21: Schematic of blazed grating geometry.

By changing the blaze angle, the diffraction efficiency for different wavelengths can be tuned. The 150 g/mm grating was blazed at 1200 nm for maximum efficiency in the wavelength range of MoTe₂ photoluminescence. The 600 g/mm grating was blazed at 1600 nm for maximum performance at telecom C&L bands. Finally, the 1200 g/mm was blazed at 500 nm for maximum efficiency for Raman spectroscopy with 532 nm excitation.

4.4.2.3 Coupling Light to Spectrometers

A Czerny-Turner spectrometer accepts light in the solid angle defined by the f-number of the spectrometer. The f-number of the spectrometer is dependant on the focal length of the spectrometer and the grating size. The longer the focal length of the spectrometer, the higher the f-number will be. As a result of this, the acceptance angle will be smaller and so the light gathering power of the spectrometer will be reduced. For Princeton Instruments line of SpectraPro spectrometers the f-numbers are as follows: $f=150$ mm F/4.0 , $f=300$ mm F/3.9 , $f=500$ mm F/6.5 and $f=750$ mm F/9.7. Therefore, the choice of the focal length for a spectrometer is a trade off between the necessary resolution and the optical throughput.

To obtain the highest optical throughput of a spectrometer, it is necessary to "f-match" the input beam to the f-number of the spectrometer. The f-number

is defined as the ratio of the focal length of a lens to the diameter of the beam (equation 4.1).

$$N = \frac{f}{D} \quad (4.1)$$

Therefore, for a 750 mm spectrometer with F/9.7 and a 5 mm input beam, a $f=48.5$ mm lens would be required. A 25 mm diameter $f=45$ mm lens was implemented to f-match the spectrometer. This was selected rather than an $f=50$ mm lens which would overfill the diffraction grating as this could result in loss of light and the production of stray light that can adversely affect the spectra.

4.4.2.4 Array Detectors

To record the spectra with a Czerny-Turner spectrometer, either an output slit with a photodiode or photomultiplier tube detector is added (which will record the intensity as the spectrometer is scanned) or an array detector is used. A linear InGaAs array detector multiplexes the measurement by recording a wide bandwidth of the spectrum with the grating static and this greatly reduces the acquisition time of the spectrum. These InGaAs array detectors are commonly used for near-IR spectroscopy between 900-1700 nm. For these detectors, spectral resolution is dictated by the grating dispersion and the pixel width while the spectral range is dictated by the number of pixels. During detection, the spectrometer is set to the desired central wavelength and the array detector acquires spectra with the specified integration time. After the integration time, the charge on each pixel is read out by the register. When reading each pixel, the charge on the pixel is converted to a voltage and then converted to a digital signal by an analogue-to-digital converter which adds read out noise to the signal. The level of noise is reduced by the cooling of the InGaAs sensor either by a dewar of liquid nitrogen or by a thermoelectric cooler to reduce dark current. Dark current is the noise due to current buildup in the pixel by thermally generated electrons (which can occur even when the pixel is not illuminated), and so by cooling the detector the thermal energy can be reduced and the dark current minimized.

When designing the microphotoluminescence system, both the Andor iDus DU490A and Princeton Instruments PyLon-IR:1024-1.7 linear InGaAs array detectors were considered. To compare the specifications of both detectors, the noise power of each detector was calculated. Noise power was calculated by finding the input signal power required to achieve a signal-to-noise ratio (SNR) of 1. The SNR of a CCD detector is given by:

$$SNR = \frac{PQE t}{\sqrt{PQE t + Dt + N_r^2}} \quad (4.2)$$

where P is the incident photon flux (photons/px/s), QE represents the CCD quantum efficiency, t is the integration time (s), D is the dark current value (e^{-1} /px/s), and $N(r)$ represents read noise (e^{-1} rms/px). The quantum efficiency curves for both array detectors are very similar which is expected as they are both manufactured by Teledyne e2v. To compare both the Princeton Instruments PyLon-IR:1024-1.7 and Andor iDus DU490A detectors (specifications detailed in Table 4.2), the input optical power on one pixel to achieve an SNR of 1 for a 1100 nm signal and 1 second integration time was calculated. This calculation yielded 9.1×10^{-19} W for the PyLon and 13×10^{-19} W for the iDus. These noise power values are directly comparable as the pixel areas are equal. Furthering this, for a room temperature PL of monolayer MoTe_2 with a FWHM of approximately 40 nm and the 150 g/mm grating we would divide by the input signal power over 130 px and so 0.12 fW is required for the signal to equal the noise for the PyLon detector and 0.17 fW is required for the iDus detector. For a given input power, the SNR can be increased by increasing the integration time as, while this will increase the dark current, the readout noise is constant and is a squared term in the SNR equation (4.2).

Table 4.2: Specification comparison between Andor iDus DU490A [79] and Princeton Instruments PyLon-IR:1024-1.7 [80].

	PyLon-IR:1024-1.7	iDus DU490A
Number of pixels	1024	512
Pixel size (μm)	25 x 500	25 x 500
Dark current $\text{ke}^-/\text{px}/\text{s}$	3.2	10.5
Pixel well depth (Me^-)	4.5	5
Read noise (e^-)	400	580
Sensitivity (e^-/count)	75	90
Digitization (bit)	16	16
Max spectra/s	6600	193
Max cooling ($^{\circ}\text{C}$)	-100	-90

In light of the similarity in the noise calculations and the significantly lower cost, the Andor iDus was selected. Upon building the microphotoluminescence setup with the Andor iDus detector, we began benchmarking the system against a collaborator's system with a PyLon detector which can detect room temperature photoluminescence of monolayer MoTe_2 . A GaAs quantum well sample with photoluminescence at 1280 nm from the same wafer was used to directly compare between the two systems. With both systems using 30 μW of excitation power, 180 ct/s was measured with the Andor iDus and 1750 ct/s was measured with the PyLon detector. Not expecting there to be a 10 fold difference between the two systems, great efforts were made to improve the efficiency of the μPL system. Initially, the PL was coupled from the microscope into a 400 μm multimode fiber and then it would fiber couple into the spectrometer. Coupling into a fiber carries significant inherent losses and so mirrors were used to couple to the spectrometer via free-space. A further adaptation was to use Ag coated mirrors rather than Al coated mirrors as the former have higher reflectivity in the near-IR. The protected Al mirrors have 90-95% reflectivity between 1-2 μm and the Ag mirrors have reflectivity between 97-98% reflectivity in this wavelength range.

4.4.2.5 Objectives

The numerical aperture (NA) of a microscope objective describes the angle at which the objective can collect light. As photoluminescence and Raman scattering emit light in all directions, the light to be gathered originates from a diffuse source. The NA of an objective is given by $NA = n \cdot \sin\theta$ where n is the refractive index of the medium surrounding the objective and θ is the collection half-angle. For air objectives, the maximum NA possible is 0.95 which allows the objective to collect from 144° while an oil immersion objective with 1.42 NA and immersion oil with refractive index of 1.51 can collect from 140° . Oil objectives are not suitable for use with 2D materials as the flakes will be contaminated by the oil and cannot be further processed. To perform cryogenic temperature measurements, a long working distance objective is required so the objective can remain outside the cryostat. Therefore, the maximum NA for this system is limited to 0.65 from using an Olympus LCPLN50XIR 50x with sufficient working distance for the cryostat and sufficient field of view to work with MoTe₂ flakes. Details of our objectives are presented in Table 4.3.

Table 4.3: Microscope objective specifications.

Objective	Magnification	NA	Working Distance (mm)
Mitutoyo M Plan Apo	20	0.42	20.0
Mitutoyo M Plan Apo	50	0.5	13.0
Mitutoyo M Plan Apo	100	0.7	6.0
Mitutoyo M Plan Apo NIR	100	0.5	10.0
Olympus LCPLN50XIR	50	0.65	5.1

To experimentally compare the light gathering power of different microscope objectives, the intensity of the 520 cm^{-1} Si Raman peak was measured with objectives that have varying NA values. This was measured using an Andor iDus 416 CCD and 15 mW 532 nm excitation power, see Figure 4.22.

From Figure 4.22, it is clear that a high NA objective is necessary to collect the maximum possible light from a diffuse source. This finding is attributed to the $\sin\theta$ dependence of NA. It is noteworthy that the Si Raman peak is broadened by a factor 2, this is likely due to heating of the sample as the oil immersion objective has a much smaller spot size therefore a higher pump power density. The pump

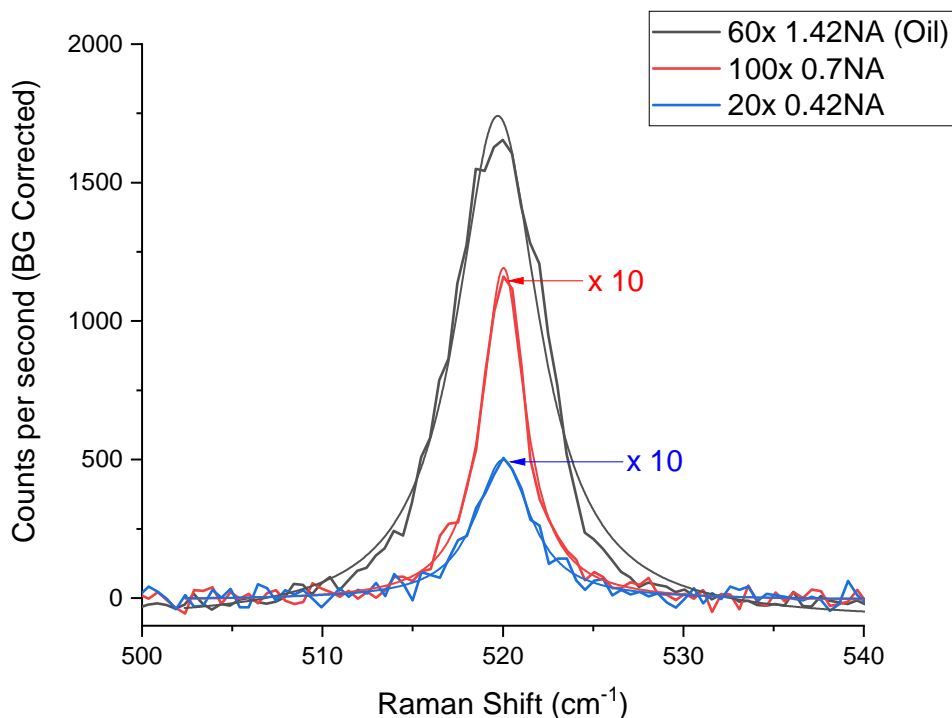


Figure 4.22: 520 cm^{-1} silicon Raman peak measured with objectives with varying numerical aperture. N.B. the 1.42NA objective uses an immersion oil with $n = 1.52$. 100x objective and 20x objective have been magnified by 10 times to be visible on the same scale.

power densities for the different objectives are as follows; 60x (Oil) = 6 MW/cm^{-2} , 100x = 3 MW/cm^{-2} , and 20x = 1.2 MW/cm^{-2} . Narayanaswamy [81] shows that an increase in temperature can cause significant peak broadening in Raman spectra of crystalline materials. More recently, the broadening of the silicon Raman peak has been used as a non-contact thermometer for MEMS applications [82] and as a sub-wavelength thermometer of nanoparticles [82].

4.4.2.6 Array Detector Performance

To investigate the relative performance of the Andor iDus DU490 and the Princeton Instruments PyLon-IR linear array detectors, a demo model of the PyLon-IR was requested. The two CCD ports on the spectrometer within the system meant that it was possible to perform a side-by-side comparison of the

two detectors. A comparison of the dark current of both detectors was obtained by blocking the input slit and performing a 100 second exposure. Figure 4.23 shows the two measured dark current spectra. The PyLon detector averages 10600 counts over the detector with a flat profile. The Andor iDus averages 52500 counts over the detector, however, it is not as consistent over the same wavelength range. The dark current measured on the Andor iDus is $\sim 5x$ higher than the PI PyLon-IR, which is consistent with a dark current of $16 \text{ ke}^-/\text{px}/\text{s}$. From the dark current measurement in the iDus manual [79], this value is within specification for a sensor temperature of -75°C and a ambient temperature of 25°C .

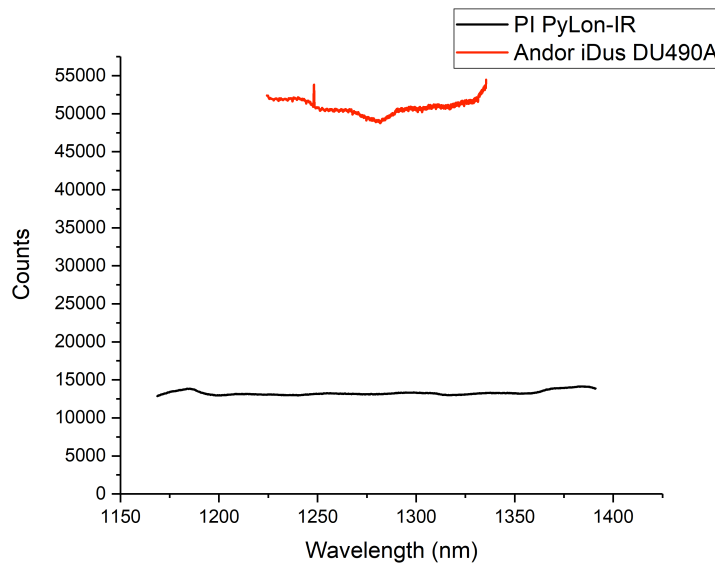


Figure 4.23: Dark noise comparison between the Princeton Instruments PyLon detector cooled to -100°C and the Andor iDus cooled to -75°C .

To compare the sensitivity of the Andor iDus DU490 and the Princeton Instruments PyLon-IR linear array detectors, the photoluminescence spectrum of a GaAs quantum dot sample was measured with $200 \mu\text{W}$ 532 nm excitation and a 10 second integration time. Figure 4.24 shows the two PL spectra. The PL spectrum taken by the Andor iDus has a peak at 2500 counts and the PyLon spectrum has a peak at 26000 counts. This 10 fold increase in PL counts was surprising as the sensitivity of the PyLon-IR is only 20% higher. In light of the far superior performance of the Princeton Instruments PyLon-IR and its ability to measure room temperature PL of MoTe_2 , an order for one was placed.

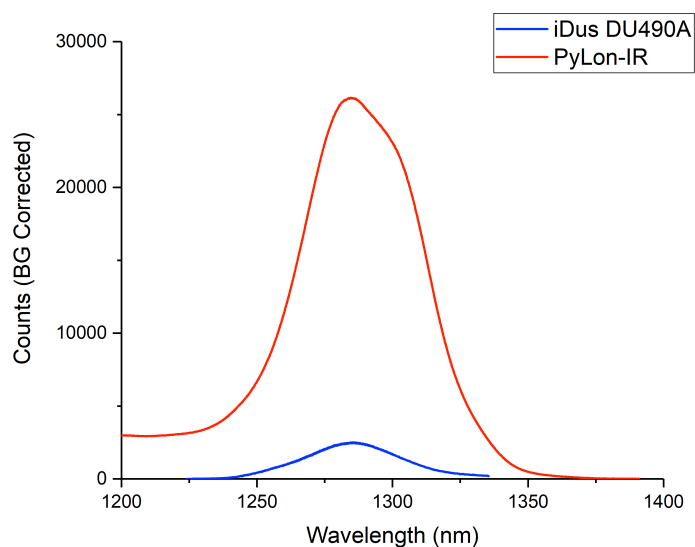


Figure 4.24: PL count rate comparison between the Princeton Instruments PyLon-IR and the Andor iDus using a GaAs quantum dot sample with identical excitation conditions.

The SpectraPro spectrometer was wavelength calibrated in our lab using an Argon lamp. This was performed for both the PI PyLon-IR and the Andor iDus. This calibration ensures that the wavelength axis is linear and accurate. Ideally one would also need to correct for the spectrometer's system transfer function. The system transfer function accounts for the diffraction efficiency of the grating and the quantum efficiency of the detector and if illuminated from the microscope can account for all optical coatings. To do an intensity calibration a broadband light source with a known spectrum illuminates the spectrometer then the difference between the measured and known spectra is used to correct further measurements [83, 84]. This is fairly simple with for a spectrometer with a slit and single detector, but becomes more complex when an array detector is involved where different grating positions and aberrations such as coma need to be accounted for. We were not able to carry out an intensity calibration of the spectrometer due to a lack of a calibrated broadband light source.

4.4.3 Temperature Dependent Microphotoluminescence of Silicon

Optical transitions readily occur in a direct bandgap semiconductor such as GaAs because only a change in energy is required for an electron and a hole to recombine. For indirect bandgap semiconductors such as Si, however, optical transitions require both a change in energy and in momentum as the conduction band (CB) and valence band (VB) are not aligned in k -space. Phonons are needed to provide the additional momentum in indirect bandgap semiconductors, which reduces the probability of the transition to occur; nevertheless, optical emission does occur in silicon, yet with much lower efficiency than in GaAs, for example. The wavelength of the emitted photon is dependent on both the bandgap (E_g) and the energy of the phonon $h\omega_0$. Therefore, when a phonon is emitted, the photon energy will be E_g reduced by the phonon energy $h\omega_0$ and when a phonon is absorbed the photon energy will be the sum of E_g and the phonon energy $h\omega_0$ [85] as illustrated in Figure 4.25(a).

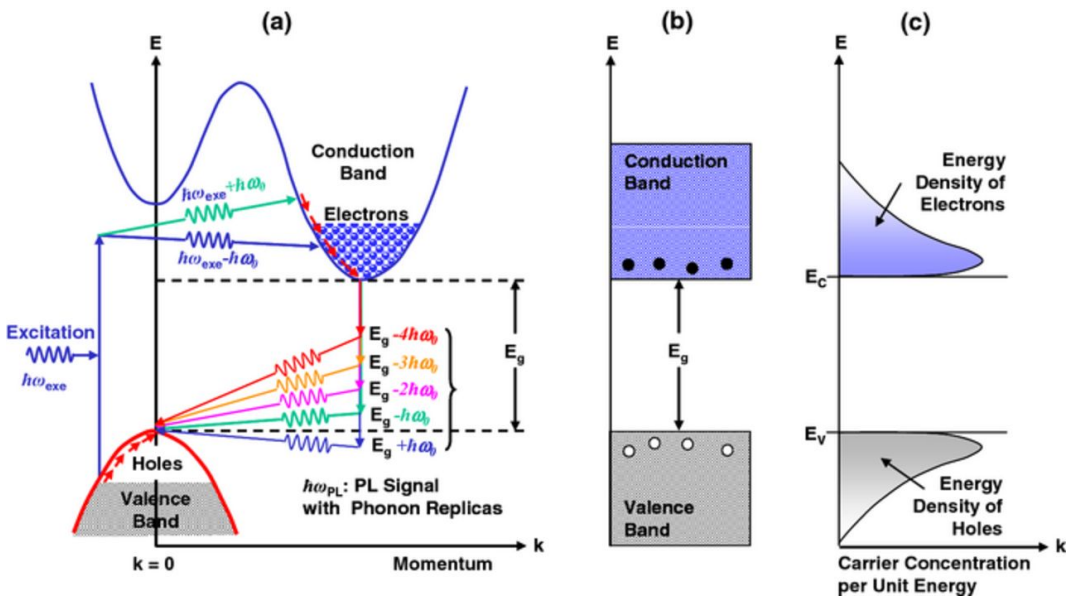


Figure 4.25: Schematic illustrations of (a) radiative recombination processes in Si, (b) energy band diagram and (c) density distribution of electrons in conduction band and holes in valence band. Figure reproduced from Ref. [85].

To obtain temperature dependant measurements of photoluminescence with temperatures down to that of liquid nitrogen (77 K), a nitrogen flow cryostat (Linkam HFS 350EV - PB4) was used. The cryostat was pumped by a

turbomolecular pump down to 10^{-5} mBar to ensure water would not condense onto the sample. Cryogenic vacuum grease (Apiezon-N) was used to ensure good thermal contact was achieved between the sample and the cold finger of the cryostat. Without the cryogenic grease, the sample may not cool to the set temperature due to the thermal insulation of the vacuum. To ensure our cryostat was functional we measured photoluminescence from a silicon-on-insulator (SOI) wafer from room temperature down to 77 K. The sample was left for 5 minutes between each cool down step to thermally equilibrate. The silicon sample was pumped by the 532 nm laser at 30 mW of power. Figure 4.26 shows the photoluminescence of SOI from bandedge emission as a function of temperature. As the silicon is cooled the PL peak narrows and slightly red-shifts indicating that the sample is being cooled.

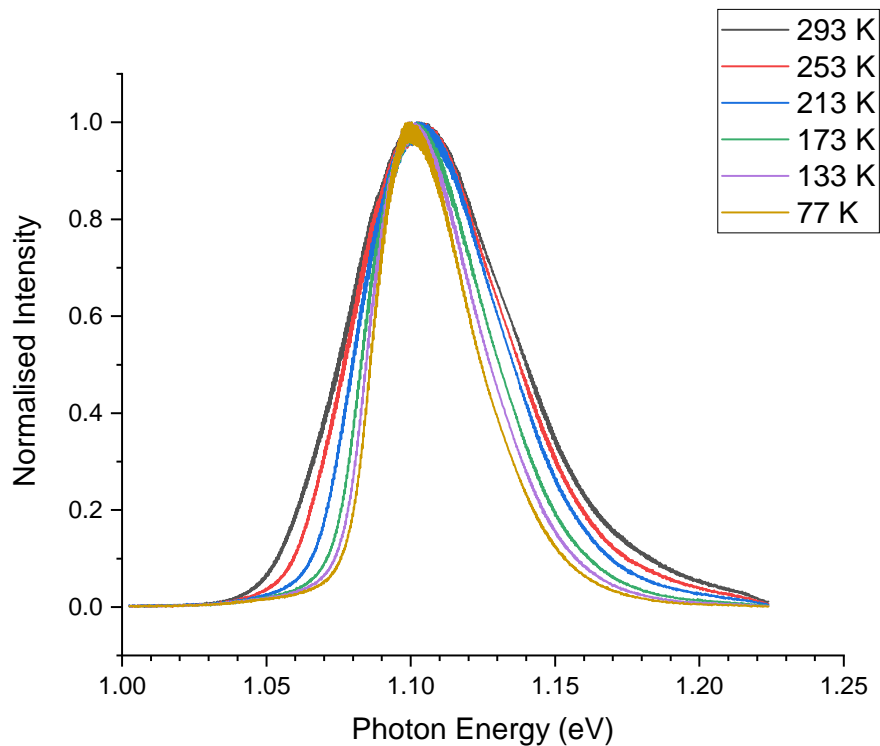


Figure 4.26: Silicon photoluminescence from SOI at varying temperatures.

The PL peak narrowing is expected and is consistent with literature [85] however the PL peak would be expected to slightly blue-shift upon cooling from the Varshni temperature dependence. Figure 4.27 shows the measured PL peak energy temperature dependence and the expected bandgap $E_g(T)$ dependence from the Varshni relation (Equation 4.3). The Varshni semi-empirical function describes the change in bandgap energy of all semiconductors with temperature

and is as follows:

$$E_g(T) = E_g(0) - \frac{\alpha T^2}{T + \beta} \quad (4.3)$$

where $E_g(0)$ is the exciton peak energy at at 0 K, T is the temperature and α and β are material constants, where β is related to the Debye temperature of the material. The parameters used for the Varshni relation are $E_g(0) = 1.166$ eV, $\alpha = 4.73 \times 10^{-4}$ eV K⁻¹ and $\beta = 636$ K [85]. There is clearly a discrepancy between the measured temperature dependent PL spectra and what is expected from theoretical considerations and the literature.

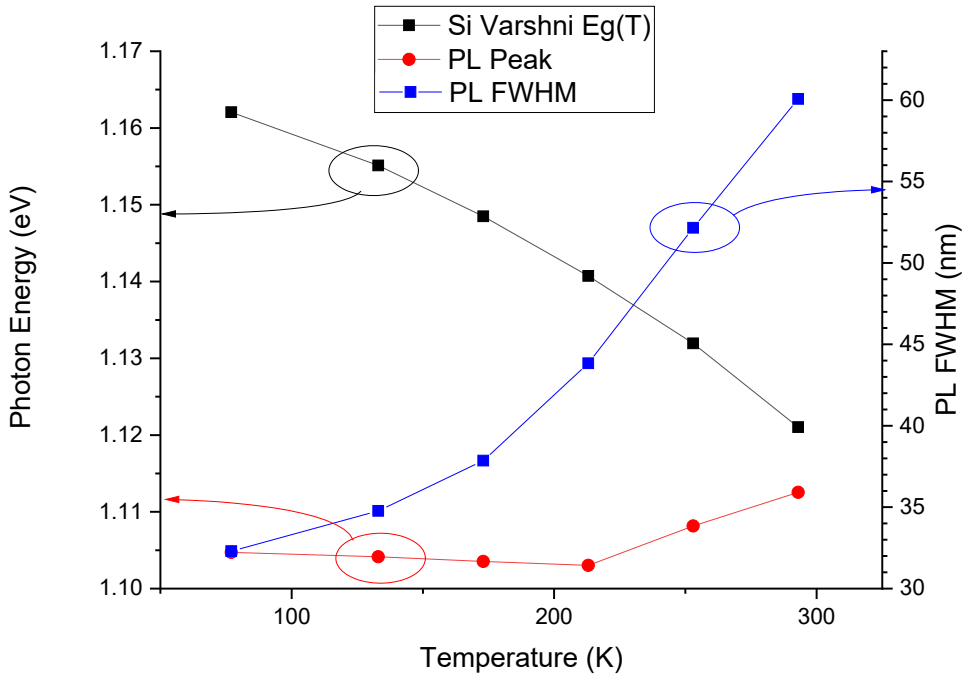


Figure 4.27: Plot of silicon temperature dependant bandgap from the Varshni relation (black). Measured photoluminescence peak energy (red). Full-width half-maximum of photoluminescence (blue).

To investigate this discrepancy the free-exciton emission from silicon was modeled using a Maxwell Boltzmann distribution as follows:

$$I_{FE}(h\nu) \approx \sqrt{h\nu - E_g(T) + E_x + h\omega} \times \exp\left(\frac{-(h\nu - E_g(T) + E_x + h\omega)}{K_B T}\right) \quad (4.4)$$

where $I_{FE}(h\nu)$ is the measured intensity of the free-exciton as a function of energy, $E_g(T)$ is the true band gap energy at temperature T , E_x is the exciton binding energy and $h\omega$ is the phonon energy. A literature value for the silicon

exciton binding energy of $E_x = 15.01$ meV [86] was used. The simulated spectra were normalised and the phonon energy fitted such that the peak matched the photoluminescence peak (Figure 4.28). The fitted phonon energy values are shown in the inset of Figure 4.28. It is plausible the anomalous photoluminescence peak shift with temperature is caused by this small shift in phonon energy.

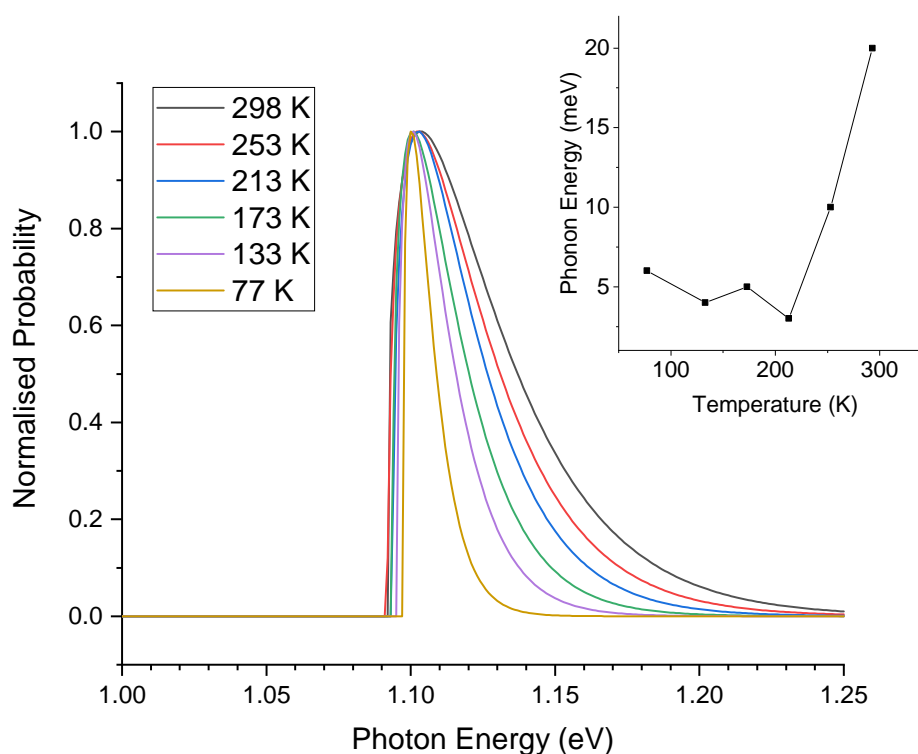


Figure 4.28: Fitted Maxwell Boltzmann distributions to temperature dependent photoluminescence of SoI Figure 4.26. Inset: Phonon energy from Maxwell Boltzmann fit.

4.4.4 Room Temperature Microphotoluminescence of Molybdenum Ditelluride

In order not to damage the flakes, low excitation power must be used. Therefore, the excitation power on a sample is measured by placing a power meter under the microscope in place of the sample and setting the laser power to produce a reading of $30 \mu\text{W}$. A Mitutoyo M Plan Apo 50x objective was used and this provided a spotsize of approximately $2 \mu\text{m}$ which give an excitation power

density of 2.3 W/cm^2 . Figure 4.29 shows the room-temperature photoluminescence of monolayer and bilayer MoTe_2 .

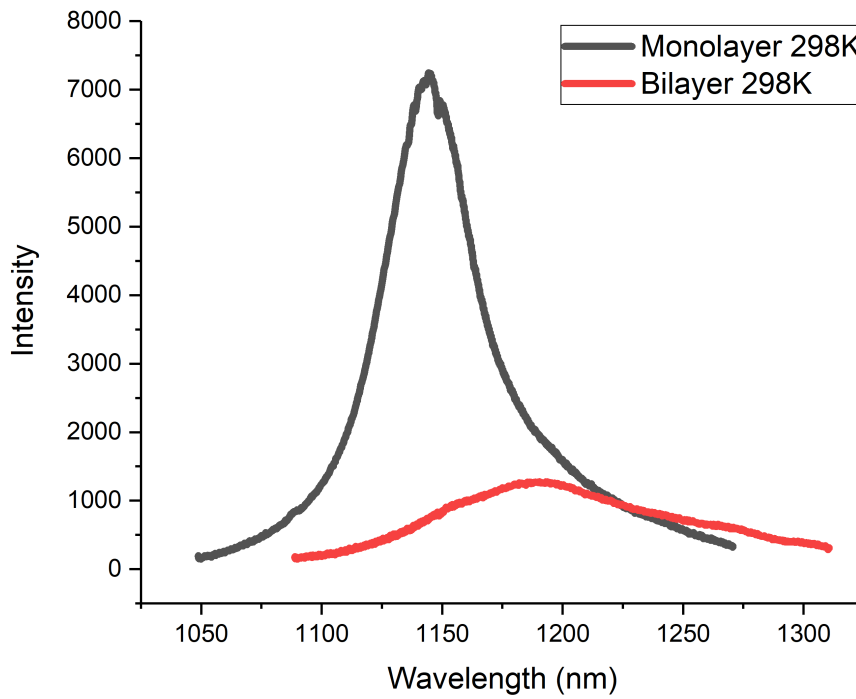


Figure 4.29: Monolayer and bilayer MoTe_2 photoluminescence.

The photoluminescence of monolayer MoTe_2 peaks at $1145 \pm 0.01 \text{ nm}$ and bilayer MoTe_2 peaks at $1197 \pm 0.3 \text{ nm}$ and these values are consistent with those reported by Ruppert et al. [14]. The photoluminescence peak position were determined from a Lorentzian fit to the spectra. The photoluminescence peak of monolayer MoTe_2 is narrower and more intense than that of the bilayer MoTe_2 . The bilayer flake may be trilayer or a mix of the two due to the asymmetry of the peak. It is these observable differences between the peaks within the spectrum, that makes photoluminescence spectroscopy a simple method to identify optically active flakes.

4.4.5 Temperature Dependent Microphotoluminescence of Molybdenum Ditelluride

The temperature dependence of MoTe₂ was investigated as it is well documented that the photoluminescence intensity from other TMDs increases with reduced temperature [35]. Further, many of the early TMD light sources relied upon low temperatures to enhance photoluminescence intensity as discussed in the review of 2D-TMD light emitters (Section 1.2). To investigate the temperature dependence of the PL peak energy, the PL peak was fitted with the Varshni function [87]. The Varshni function has been shown to fit for TMDs such as MoS₂ and MoSe₂ [88] and was shown to also fit for MoTe₂ [89].

Figure 4.30 shows the evolution of the PL peak of monolayer MoTe₂ from room temperature to 77 K. As the temperature decreases, the PL peak narrows and blueshifts. The PL peak remains as a single peak down to liquid nitrogen temperature (77 K) but if cooled to liquid helium temperature (4 K) the peak splits into its constituent exciton (X^0) and trion (X^T) peaks below 60 K [89, 90].

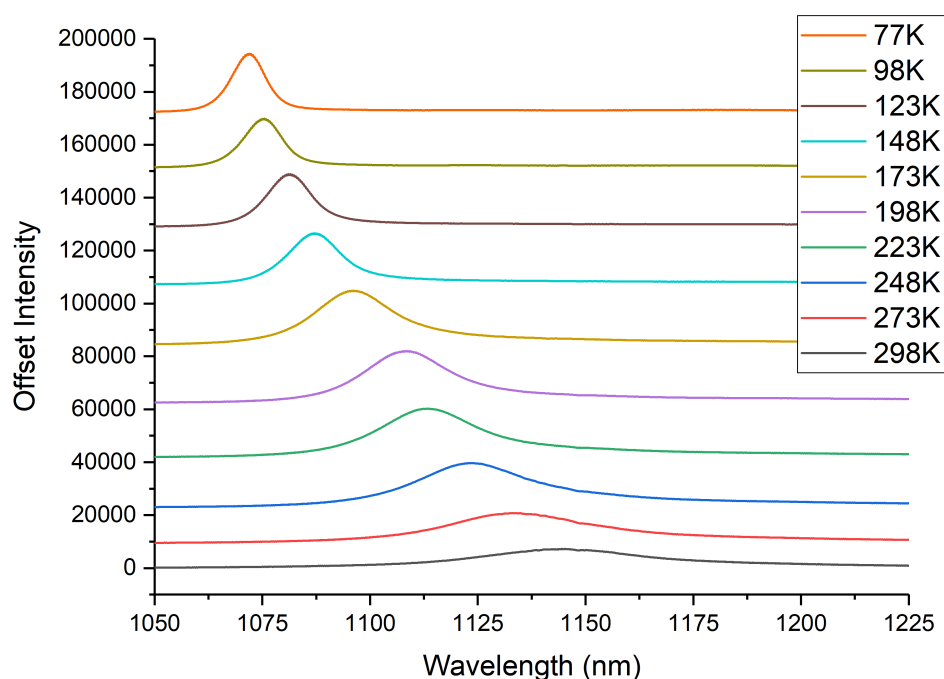


Figure 4.30: Temperature dependent photoluminescence of MoTe₂.

The temperature dependent measurement was repeated for bilayer MoTe₂. The PL peak wavelength was converted into PL peak energy and plotted against temperature. The data points were fitted with the Varshni function in Origin and values for α and β were extracted (Table 4.4). Figure 4.31 shows the Varshni function fitted temperature dependant PL measurement for monolayer and bilayer MoTe₂.

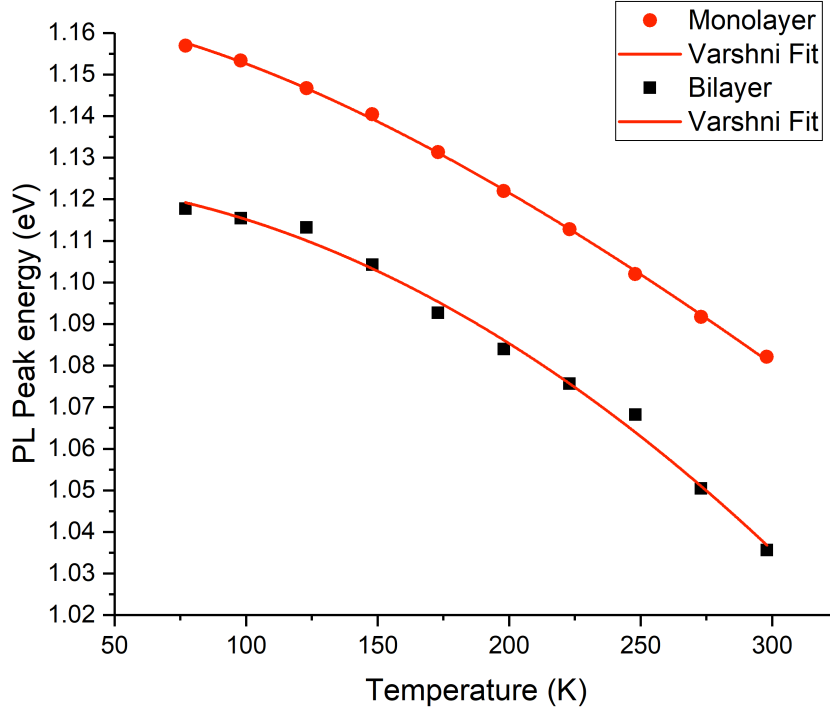


Figure 4.31: Photoluminescence peak energy of monolayer (red circles) and bilayer (black squares) MoTe₂ versus temperature. The solid red lines represent fits by the Varshni function.

Table 4.4: Varshni function fit data for monolayer (ML) MoTe₂ and bilayer (BL) MoTe₂.

	This Work		Helmrich et al. [89]	
	ML MoTe ₂	BL MoTe ₂	ML MoTe ₂	BL MoTe ₂
$E_g(0)$ (eV)	1.170	1.132	1.189	1.154
α (10^{-4} eV K ⁻¹)	5.01	6.21	5.05	6.01
β (K)	205	308	191	236

From Table 4.4, we see that our values for α and β are similar to those of Helmrich et al. [89]. There is a small difference in the measurement of $E_g(0)$ as we could only measure down to 77 K. The Varshni function significantly levels off below 50 K explaining why our fitted γ -intercept differs.

4.4.6 Photoluminescence from CVD Molybdenum DiteLLuride

While it was possible to measure photoluminescence from exfoliated MoTe_2 on our microphotoluminescence system at York, we found we could not observe photoluminescence of CVD MoTe_2 . A sample was taken to be measured down to 5 K on a trip to visit collaborators in China by Dr Yue Wang. A 4 nm thick CVD grown MoTe_2 sample was cooled to 5 K in a Montana Instruments Cryostation with a Cryo-Optic 0.9 NA 100X Zeiss objective. The microphotoluminescence was captured by a Princeton Instruments SpectraPro 2500 spectrometer with a Princeton Instruments NIRVana InGaAs focal plane array. The NIRVana has far lower dark noise and read-out noise than that of the PyLon-IR we have in York. The CVD MoTe_2 was excited by a 785 nm laser with 30 μW of optical power. Even at 5K no photoluminescence was observed.

The CVD MoTe_2 was then thinned using an oxygen plasma. It has been reported that by exposing MoTe_2 flakes to an oxygen plasma that the layers can be selectively thinned [91, 92]. An Oxford Instruments ICP plasma etcher was used to process the sample. The ICP was pumped down to a base pressure of 10^{-9} mBar then filled with 30 sccm of O_2 and the pressure was regulated to 10^{-2} mBar. A plasma was struck in the ICP with 400 W and that plasma was then drawn towards the sample with 30 W of forwards power.

Figure 4.32 shows the measured PL spectrum from 40 K down to 5 K. The peak observed at 1126 nm is the silicon photoluminescence peak from the SOI substrate. From 40 K to 7.1 K, no photoluminescence from MoTe_2 was observed. From 6.3 K to 5 K, a peak at 1150 nm was observed which we attribute to the CVD MoTe_2 .

The very low temperature appearance of photoluminescence from CVD MoTe_2 suggests strong thermal quenching within the sample. As the CVD was

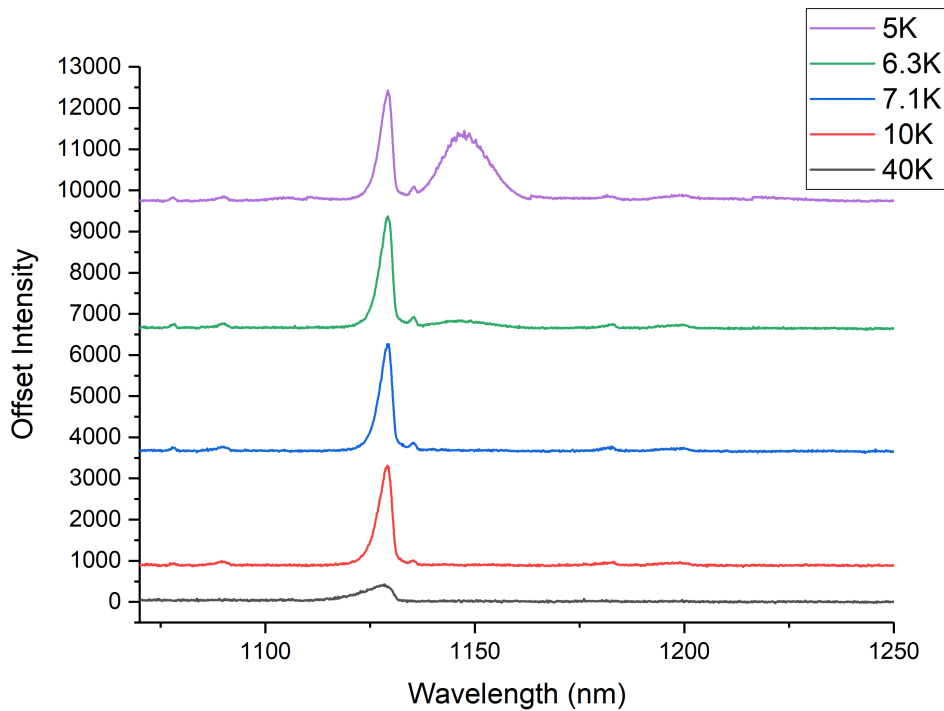


Figure 4.32: Stacked photoluminescence plot of O₂ plasma treated CVD MoTe₂ at 40, 10, 7.1, 6.3 and 5 K.

found to be polycrystalline in Section 4.3 the poor photoluminescence compared with the crystalline exfoliated MoTe₂ could be due to defects at the grain boundaries which can cause strong non-radiative recombination. There may also be dislocations, vacancies and anti-site defects from the growth that could quench photoluminescence [93–95].

4.5 Summary

In this chapter we detailed the creation of few-layer MoTe₂ flakes using both exfoliation and CVD methods (See Section 4.1 and 4.2). Structural characterisation in Section 4.3 showed that for both the exfoliated and CVD MoTe₂ the optically active 2H polymorph was present.

The photoluminescence setup used in these studies has been described in detail with key decisions highlighted. The system was optimised by careful choice of optical components and countless days improving the optical

alignment. This culminated in a study of the temperature dependent photoluminescence of exfoliated MoTe₂ flakes. Photoluminescence from CVD MoTe₂ was not observable using our microphotoluminescence system. Measurements were taken at liquid He temperatures in a collaborator's lab and some photoluminescence from CVD MoTe₂ was observable below 6.3 K after an oxygen plasma treatment. Clearly this is an area where further work is required and this will be detailed within the following section.

5 Conclusions

During my PhD Project, I was fortunate enough to be exposed to all areas of photonics research from the design of devices to nanofabrication and optical testing. I also had the opportunity to build many pieces of equipment, including an ellipsometer and several microscopes, and commissioned our in-house designed sputterer. I learnt to characterize novel materials both optically and structurally.

In Chapter 1, I discussed the motivation behind the project. With the breakdown of Moore's Law, microprocessor clock speeds are no longer increasing exponentially. This is due to transistor node sizes shrinking to the point where quantum tunnelling from source to drain is an issue that results in leakage current and increased power consumption. The use of silicon photonics aims to reduce the power consumption, due to resistive losses in the microprocessor, while simultaneously increasing the available data transmission bandwidth and enable higher clock speeds. To achieve integration of silicon photonics on-chip a light source is required as silicon is a poor light emitter. We investigated the use of 2D materials, specifically transition metal dichalcogenides, as a candidate light source.

When reviewing TMD microcavity light sources (Section 1.2) a number of devices were presented that apparently meet the conditions for lasing, yet there was considerable debate in the community as to whether lasing was actually achieved. By employing a very comprehensive set of assessment criteria, it was shown that none of the TMD devices met all the conditions for lasing, despite some very convincing data being presented. However, this is not that surprising as history shows that every time a new class of laser is developed, early publications seem to forget that coherent emission is the key evidence to proving lasing. The more stringent lasing criteria we set out in Section 2.3 and published in [96] provide robust standards for the determination of lasing from microcavity

emitters using TMDs as gain material. This work is already having an impact with our paper already achieving 13 citations as of April 2020.

In Chapter 2, the theory of waveguide optics and photonic crystal cavities was discussed. Photonic crystal cavities, specifically the Ln-type, are well suited to producing an on-chip light source due to their high Q -factor and easy integration with 2D gain materials via dry transfer techniques.

Chapter 3 discusses the nanofabrication and optical characterization of Ln-type photonic crystal cavities. The fabricated Ln-type cavities were characterized spectroscopically using a variety of light sources. Where a broadband light source for the designed resonant wavelength was available, the resonant scattering technique provided a high SNR measurement by filtering the light not coupled to the cavity mode. For cavities with resonant wavelength in the bandedge emission of silicon, the silicon cavity was pumped with a laser and light was generated within the cavity. Finally, for cavities with high Q -factor, a tunable laser was used in the resonant scattering configuration to resolve the cavity resonances.

The structural and optical properties of exfoliated and CVD grown MoTe_2 were investigated in Chapter 4. The exfoliated MoTe_2 was found to be in the 2H phase, as specified by HQ Graphene, and single crystal (through analysis by Raman, XRD and TEM). The CVD grown MoTe_2 was confirmed to be 2H phase through Raman, XRD, and TEM, but a polycrystalline structure was alluded to by XRD analysis and confirmed by the TEM diffraction pattern. Microphotoluminescence of the exfoliated MoTe_2 showed good light emission for the monolayer and weaker emission for the bilayer which was as expected from the literature. Temperature dependant microphotoluminescence of the exfoliated MoTe_2 was performed down to liquid nitrogen temperature (77 K) and the fitted parameters for the PL peak energy compare well with the literature. Microphotoluminescence of the CVD MoTe_2 was conducted at 5 K but no PL was observed until an oxygen plasma treatment was undertaken. We believe that the oxygen plasma may thin the sample down from 4 nm to mono or bilayers, yet photoluminescence was only detected below 6.3 K and this was attributed to the polycrystalline structure of the sample.

Developing a microphotoluminescence system to measure PL from 2D materials was far more challenging than could have ever been predicted. The

countless number of iterations and rebuilds of the system tested my patience but all the effort was rewarded when I first measured MoTe₂ PL (even though it was at the 11th hour of my PhD). I take solace in the fact that not many research groups have a μ PL system as capable as ours.

5.1 Future Work

To continue the work started in this thesis to achieve a TMD microcavity laser operating at >1100 nm, integration of the MoTe₂ and the photonic crystal cavity needs to be performed. Some preliminary work was done towards the end of my PhD but when the MoTe₂ flake was transferred to the silicon cavity the photoluminescence was quenched. This effect could be mitigated by sandwiching the MoTe₂ flake between two layers of hexagonal boron nitride (h-BN). The insulating properties of h-BN would both insulate the flake from the effect of silicon and also encapsulate the flake preventing degradation. Once that has been achieved, then the coherence of the emission should be characterized either via a $g^{(2)}$ measurement or achieving linewidth narrowing of a factor 2 and a convincing kink in the L-L curve.

To continue the work with CVD grown MoTe₂, more characterization of the grown films needs to be conducted to optimise the CVD growth process. One key factor to control will be the grain size of the polycrystalline material, as grain boundaries can cause strong non-radiative recombination. To assess the grain size, techniques such as TEM can be employed. More in-depth characterization of the atomic structure could also be done using TEM by looking for vacancies, dislocations and stacking faults with High-Angle Annular Dark-Field Scanning Transmission Electron Microscopy (HAADF-STEM). Furthermore, anti-site defects could be identified by Electron Energy Loss Spectroscopy (EELS) which, if present, could explain the current lack of photoluminescence. Other techniques that would improve understanding of the surface of the CVD grown MoTe₂ include X-Ray Photoluminescence Spectroscopy (XPS) and Scanning Probe Microscopy (SPM). By knowing more about the structure of the CVD grown MoTe₂, it is hoped that the CVD process could be further optimised to produce optically active MoTe₂ layers.

The next step towards a practical device would be to investigate electroluminescence from MoTe₂. Some preliminary work has been conducted by Dr Yue Wang and Dr Fahrettin Sarcan. They investigated the electrical properties of MoTe₂ flakes by a Hall-bar measurements. Once electroluminescence is observed, the flake could be coupled to a PhCC to produce an electrically pumped MoTe₂ microcavity laser. This would make an ideal on-chip silicon light source for photonic applications. I wish Dr Yue Wang and her new PhD student the best fortune in continuing this work.

References

- [1] G. M. Moore. “Cramming more components onto integrated circuits”. In: *Electronics* 38.8 (1965), p. 114.
- [2] P. Alcorn. *AMD Unveils 7nm EPYC Rome Processors, up to 64 Cores and 128 Threads for \$6,950*. 0.
- [3] N. Jones. “How to stop data centres from gobbling up the world’s electricity.” In: *Nature* 561.7722 (2018), p. 163.
- [4] A. Andrae et al. “On Global Electricity Usage of Communication Technology: Trends to 2030”. In: *Challenges* 6.1 (2015), pp. 117–157. DOI: 10.3390/challe6010117.
- [5] A. Narasimha et al. “A 40-Gb/s QSFP optoelectronic transceiver in a 0.13 μ m CMOS silicon-on-insulator technology”. In: *OFC/NFOEC 2008 - 2008 Conference on Optical Fiber Communication/National Fiber Optic Engineers Conference* (2008), pp. 1–3. DOI: 10.1109/OFC.2008.4528356.
- [6] G. Roelkens et al. “III-V/silicon photonics for on-chip and intra-chip optical interconnects”. In: *Laser and Photonics Reviews* 4.6 (2010), pp. 751–779. DOI: 10.1002/lpor.200900033.
- [7] G. T. Reed et al. “Silicon optical modulators”. In: *Nat Photon* 4.8 (Aug. 2010), pp. 518–526. DOI: 10.1038/nphoton.2010.179.
- [8] J. Michel et al. “High-performance Ge-on-Si photodetectors”. In: *Nature Photonics* 4.8 (Aug. 2010), pp. 527–534. DOI: 10.1038/nphoton.2010.157.
- [9] W. Bogaerts et al. “Nanophotonic waveguides in silicon-on-insulator fabricated with CMOS technology”. In: *Journal of Lightwave Technology* 23.1 (Jan. 2005), pp. 401–412. DOI: 10.1109/JLT.2004.834471.

- [10] A. W. Fang et al. “Electrically pumped hybrid AlGaInAs-silicon evanescent laser.” In: *Optics express* 14.20 (2006), pp. 9203–9210. DOI: 10.1109/LPT.2006.874690.
- [11] F. Xia et al. “Two-dimensional material nanophotonics”. In: *Nature Photonics* 8.12 (2014), pp. 899–907. DOI: 10.1038/nphoton.2014.271.
- [12] O. Salehzadeh et al. “Optically Pumped Two-Dimensional MoS₂ Lasers Operating at Room-Temperature”. In: *Nano Letters* 15.8 (2015), pp. 5302–5306. DOI: 10.1021/acs.nanolett.5b01665.
- [13] S. Wu et al. “Monolayer semiconductor nanocavity lasers with ultralow thresholds”. In: *Nature* 520.7545 (2015), pp. 69–72. DOI: 10.1038/nature14290.
- [14] C. Ruppert et al. “Optical properties and band gap of single- and few-layer MoTe₂ crystals”. In: *Nano Letters* 14.11 (2014), pp. 6231–6236. DOI: 10.1021/nl502557g.
- [15] Y. Ye et al. “Monolayer excitonic laser”. In: *Nature Photonics* 9.11 (2015), pp. 733–737. DOI: 10.1038/nphoton.2015.197.
- [16] R. Dhall et al. “Direct bandgap transition in many-layer MoS₂ by plasma-induced layer decoupling”. In: *Advanced Materials* 27.9 (2015), pp. 1573–1578. DOI: 10.1002/adma.201405259.
- [17] Y. Li et al. “Room-temperature continuous-wave lasing from monolayer molybdenum ditelluride integrated with a silicon nanobeam cavity”. In: *Nature Nanotechnology* 12.10 (2017), pp. 987–992. DOI: 10.1038/nnano.2017.128.
- [18] J. D. Joannopoulos et al. *Photonic Crystals: Molding the Flow of Light - Second Edition*. 2nd ed. Princeton University Press, 2011, 2011.
- [19] M. Hammer. “2-D multilayer waveguide mode solver, variational effective index approximation”. In: <https://www.computational-photonics.eu/eims.html> ().
- [20] L. Rayleigh. “XVII. On the maintenance of vibrations by forces of double frequency, and on the propagation of waves through a medium endowed with a periodic structure”. In: *The London, Edinburgh, and Dublin Philosophical Magazine and Journal of Science* 24.147 (1887), pp. 145–159. DOI: 10.1080/14786448708628074.

- [21] D. Bouwmeester et al. “Far-field emission profiles from L3 photonic crystal cavity modes”. In: *Photonics and Nanostructures - Fundamentals and Applications* 11.1 (2012), pp. 37–47. DOI: 10.1016/j.photonics.2012.07.003.
- [22] M. Galli et al. “Light scattering and Fano resonances in high-Q photonic crystal nanocavities”. In: *Applied Physics Letters* 94.7 (2009), pp. 2007–2010. DOI: 10.1063/1.3080683.
- [23] E. M. Purcell. “Spontaneous emission probabilities at radio frequencies”. In: *Physical Review* 69 (1946), pp. 681+. DOI: 10.1007/978-1-4615-1963-8{_}40.
- [24] J. Vuckovic et al. “Linewidth narrowing and Purcell enhancement in photonic crystal cavities on an Er-doped silicon nitride platform”. In: *Optics Express* 18.3 (2010), p. 2601. DOI: 10.1364/oe.18.002601.
- [25] C. Javerzac-Galy et al. “Excitonic Emission of Monolayer Semiconductors Near-Field Coupled to High-Q Microresonators”. In: *Nano Letters* 18.5 (May 2018), pp. 3138–3146. DOI: 10.1021/acs.nanolett.8b00749.
- [26] Y. Akahane et al. “High-Q photonic nanocavity in a two-dimensional photonic crystal”. In: *Nature* 425.6961 (Oct. 2003), pp. 944–947. DOI: 10.1038/nature02063.
- [27] H. Sekoguchi et al. “Photonic crystal nanocavity with a Q-factor of ~9 million”. In: *Optics Express* (2014). DOI: 10.1364/oe.22.000916.
- [28] S. L. Portalupi et al. “Planar photonic crystal cavities with far-field optimization for high coupling efficiency and quality factor”. In: *Optics Express* 18.15 (2010), p. 16064. DOI: 10.1364/OE.18.016064.
- [29] K. S. Novoselov et al. “Electric Field Effect in Atomically Thin Carbon Films”. In: *Science* 306.5696 (Oct. 2004), 666 LP –669. DOI: 10.1126/science.1102896.
- [30] M. Wang et al. “A platform for large-scale graphene electronics - CVD growth of single-layer graphene on CVD-grown hexagonal boron nitride”. In: *Advanced Materials* 25.19 (2013), pp. 2746–2752. DOI: 10.1002/adma.201204904.
- [31] K. S. Novoselov et al. “Two-dimensional gas of massless Dirac fermions in graphene”. In: *Nature* 438.7065 (2005), pp. 197–200. DOI: 10.1038/nature04233.

- [32] A. T. Hanbicki et al. “Measurement of high exciton binding energy in the monolayer transition-metal dichalcogenides WS₂ and WSe₂”. In: *Solid State Communications* 203 (2015), pp. 16–20. DOI: 10.1016/j.ssc.2014.11.005.
- [33] J. A. Wilson et al. “The transition metal dichalcogenides discussion and interpretation of the observed optical, electrical and structural properties”. In: *Advances in Physics* 18.73 (1969), pp. 193–335. DOI: 10.1080/00018736900101307.
- [34] K. Behnia. “Condensed-matter physics: Polarized light boosts valleytronics”. In: *Nature Nanotechnology* 7.8 (2012), pp. 488–489. DOI: 10.1038/nnano.2012.117.
- [35] M. Koperski et al. “Optical properties of atomically thin transition metal dichalcogenides: Observations and puzzles”. In: *Nanophotonics* 6.6 (2017), pp. 1289–1308. DOI: 10.1515/nanoph-2016-0165.
- [36] G. Wang et al. “Colloquium: Excitons in atomically thin transition metal dichalcogenides”. In: *Rev. Mod. Phys.* 90.2 (Apr. 2018), p. 21001. DOI: 10.1103/RevModPhys.90.021001.
- [37] C. Robert et al. “Exciton radiative lifetime in transition metal dichalcogenide monolayers”. In: *Physical Review B* 93.20 (2016), pp. 1–10. DOI: 10.1103/PhysRevB.93.205423.
- [38] M. Palumbo et al. “Exciton radiative lifetimes in two-dimensional transition metal dichalcogenides”. In: *Nano Letters* 15.5 (2015), pp. 2794–2800. DOI: 10.1021/nl503799t.
- [39] H. Zeng et al. “Optical signature of symmetry variations and spin-valley coupling in atomically thin tungsten dichalcogenides”. In: *Scientific Reports* 3.4 (2013), pp. 4908–4916. DOI: 10.1038/srep01608.
- [40] M. Currie et al. “Optical control of charged exciton states in tungsten disulfide”. In: *Applied Physics Letters* 106.20 (2015). DOI: 10.1063/1.4921472.
- [41] “Scrutinizing lasers”. In: *Nature Photonics* 11 (Mar. 2017), p. 139. DOI: 10.1038/nphoton.2017.28.
- [42] I. D. W. Samuel et al. “How to recognize lasing”. In: *Nature Photonics* 3.10 (2009), pp. 546–549. DOI: 10.1038/nphoton.2009.173.
- [43] G. Björk et al. “Definition of a laser threshold”. In: *Physical Review A* 50.2 (1994), pp. 1675–1680. DOI: 10.1103/PhysRevA.50.1675.

- [44] W. W. Chow et al. “Emission properties of nanolasers during the transition to lasing”. In: *Light: Science and Applications* 3.March (2014), pp. 1–8. DOI: 10.1038/lsa.2014.82.
- [45] R. Hanbury Brown et al. “A test of a new type of stellar interferometer on Sirius”. In: *Nature* 178.4541 (1956), pp. 1046–1048. DOI: 10.1038/1781046a0.
- [46] L. Mandel et al. “Coherence Properties of Optical Fields”. In: *Reviews of Modern Physics* 37.2 (Apr. 1965), pp. 231–287. DOI: 10.1103/RevModPhys.37.231.
- [47] A. L. Schawlow et al. “Infrared and optical masers”. In: *Physical Review* 112.6 (1958), pp. 1940–1949. DOI: 10.1103/PhysRev.112.1940.
- [48] A. E. Siegman. *Lasers*. University Science Books, 1986.
- [49] S. Kreinberg et al. “Emission from quantum-dot high- β microcavities: transition from spontaneous emission to lasing and the effects of superradiant emitter coupling”. In: *Light: Science & Applications* 6 (Aug. 2017), e17030. DOI: 10.1038/lsa.2017.30.
- [50] R. Lo Savio et al. “Room-temperature emission at telecom wavelengths from silicon photonic crystal nanocavities”. In: *Applied Physics Letters* 98.20 (2011), pp. 1–4. DOI: 10.1063/1.3591174.
- [51] Z. Luo et al. “Two-dimensional material-based saturable absorbers: towards compact visible-wavelength all-fiber pulsed lasers”. In: *Nanoscale* 8.2 (2016), pp. 1066–1072. DOI: 10.1039/C5NR06981E.
- [52] H. Ito et al. “Chemical amplification resists: History and development within IBM”. In: *IBM Journal of Research and Development* 44.1.2 (2000), pp. 119–130. DOI: 10.1147/rd.441.0119.
- [53] H. M. Park. “Control of Ion Energy in a Capacitively Coupled Reactive Ion Etcher”. In: *Journal of The Electrochemical Society* 145.12 (2006), p. 4247. DOI: 10.1149/1.1838945.
- [54] H. Jansen et al. “A survey on the reactive ion etching of silicon in microtechnology”. In: *Journal of Micromechanics and Microengineering* 6.1 (1996), pp. 14–28. DOI: 10.1088/0960-1317/6/1/002.
- [55] D. O’Connell et al. “The role of the relative voltage and phase for frequency coupling in a dual-frequency capacitively coupled plasma”. In: *Applied Physics Letters* 93.8 (2008), pp. 2006–2009. DOI: 10.1063/1.2972117.

- [56] H. Jansen et al. “BSM 7: RIE lag in high aspect ratio trench etching of silicon”. In: *Microelectronic Engineering* 35.1-4 (2002), pp. 45–50. DOI: 10 . 1016 / s0167-9317(96)00142-6.
- [57] L. Novotny et al. *Propagation and focusing of optical fields*. 2012, pp. 45–85. DOI: 10 . 1017 / cbo9780511794193 . 005.
- [58] U. Fano. “Effects of Integration on Intensities and Phase Shifts”. In: *Physical Review* 124.6 (1961), pp. 1866–1878.
- [59] D. P. Cai et al. “High Q-factor microring resonator wrapped by the curved waveguide”. In: *Scientific Reports* 5 (2015), pp. 1–8. DOI: 10 . 1038 / srep10078.
- [60] A. Singh. “Free charge carrier induced refractive index modulation of crystalline Silicon”. In: *IEEE International Conference on Group IV Photonics GFP* 2.4 (2010), pp. 102–104. DOI: 10 . 1109 / GROUP4 . 2010 . 5643412.
- [61] L. S. Yu et al. “Direct measurement of the refractive index change of silicon with optically injected carriers”. In: *Applied Physics Letters* 68.11 (1996), pp. 1546–1548. DOI: 10 . 1063 / 1 . 115694.
- [62] I. G. Lezama et al. “Indirect-to-direct band-gap crossover in few-layer MoTe₂”. In: *Nano letters* 15.4 (2015), pp. 2336–42. DOI: 10 . 1021 / n15045007.
- [63] K. S. Novoselov et al. “Two-dimensional atomic crystals”. In: *Proceedings of the National Academy of Sciences of the United States of America* 102.30 (July 2005), pp. 10451–10453. DOI: 10 . 1073 / pnas . 0502848102.
- [64] A. Castellanos-Gomez et al. “Deterministic transfer of two-dimensional materials by all-dry viscoelastic stamping”. In: *2D Materials* 1.1 (2014). DOI: 10 . 1088 / 2053-1583 / 1 / 1 / 011002.
- [65] S. Balendhran et al. “Two-dimensional molybdenum trioxide and dichalcogenides”. In: *Advanced Functional Materials* 23.32 (2013), pp. 3952–3970. DOI: 10 . 1002 / adfm . 201300125.
- [66] B. S. Jessen et al. “Quantitative optical mapping of two-dimensional materials”. In: *Scientific Reports* 8.1 (2018), pp. 2–9. DOI: 10 . 1038 / s41598-018-23922-1.

- [67] R. Frisenda et al. “Recent progress in the assembly of nanodevices and van der Waals heterostructures by deterministic placement of 2D materials”. In: *Chemical Society Reviews* 47.1 (2018), pp. 53–68. DOI: 10.1039/c7cs00556c.
- [68] F. Pizzocchero et al. “The hot pick-up technique for batch assembly of van der Waals heterostructures”. In: *Nature Communications* 7.May (2016). DOI: 10.1038/ncomms11894.
- [69] J. C. McGlynn et al. “Molybdenum Ditelluride Rendered into an Efficient and Stable Electrocatalyst for the Hydrogen Evolution Reaction by Polymorphic Control”. In: *Energy Technology* 6.2 (2018), pp. 345–350. DOI: 10.1002/ente.201700489.
- [70] J. McAllister et al. “Tuning and mechanistic insights of metal chalcogenide molecular catalysts for the hydrogen-evolution reaction”. In: *Nature Communications* 10.1 (2019). DOI: 10.1038/s41467-018-08208-4.
- [71] P. Song et al. “Few-layer 1T’ MoTe₂ as gapless semimetal with thickness dependent carrier transport”. In: *2D Materials* 5.3 (2018). DOI: 10.1088/2053-1583/aac78d.
- [72] Y. Tan et al. “Controllable 2H-to-1T’ phase transition in few-layer MoTe₂”. In: *Nanoscale* 10.42 (2018), pp. 19964–19971. DOI: 10.1039/c8nr06115g.
- [73] T. A. Empante et al. “Chemical Vapor Deposition Growth of Few-Layer MoTe₂ in the 2H, 1T’, and 1T Phases: Tunable Properties of MoTe₂ Films”. In: *ACS Nano* 11.1 (2017), pp. 900–905. DOI: 10.1021/acsnano.6b07499.
- [74] B. D. Cullity et al. *Elements of X-Ray Diffraction: Pearson New International Edition*. Pearson Education Limited, 2013.
- [75] R. b. P. D. Brown. “Transmission Electron Microscopy-A Textbook for Materials Science, by David B. Williams and C. Barry Carter”. In: *Microscopy and Microanalysis* 5.6 (1999), pp. 452–453. DOI: DOI:10.1017/S1431927699990529.
- [76] M. K. Jana et al. “Two-dimensional inorganic analogues of graphene: Transition metal dichalcogenides”. In: *Philosophical Transactions of the Royal Society A: Mathematical, Physical and Engineering Sciences* 374.2076 (2016). DOI: 10.1098/rsta.2015.0318.

- [77] B. Wang et al. “Enhanced current rectification and self-powered photoresponse in multilayer p-MoTe₂/n-MoS₂ van der Waals heterojunctions”. In: *Nanoscale* 9.30 (2017), pp. 10733–10740. DOI: 10.1039/c7nr03445h.
- [78] P. Instruments. *Acton Series SP-2750 Manual*. 2003.
- [79] Andor. *iDus InGaAs detector array for Spectroscopy Manual*. 2019.
- [80] Princeton-Instruments. *PyLoN-IR Specifications (PyLoN-IR Rev. N2.2)*. 2019.
- [81] P. K. Narayanaswamy. “Influence of temperature on the Raman spectra of crystals”. In: *Proceedings of the Indian Academy of Sciences - Section A* 28.2 (1948), pp. 40–45. DOI: 10.1007/BF03171428.
- [82] A. Gkouzou et al. “Controlling adhesion between multi-asperity contacting surfaces in MEMS devices by local heating”. In: *Journal of Micromechanics and Microengineering* 26.9 (2016). DOI: 10.1088/0960-1317/26/9/095020.
- [83] M. Fryling et al. “Intensity calibration and sensitivity comparisons for CCD/Raman spectrometers”. In: *Applied Spectroscopy* 47.12 (1993), pp. 1965–1974. DOI: 10.1366/0003702934066226.
- [84] A. K. Gaigalas et al. “Procedures for wavelength calibration and spectral response correction of CCD array spectrometers”. In: *Journal of Research of the National Institute of Standards and Technology* 114.4 (2009), pp. 1–14. DOI: 10.6028/jres.114.015.
- [85] W. S. Yoo et al. “Temperature dependence of photoluminescence spectra from crystalline silicon”. In: *ECS Journal of Solid State Science and Technology* 4.12 (2015), P456–P461. DOI: 10.1149/2.0251512jss.
- [86] M. A. Green. “Improved value for the silicon free exciton binding energy”. In: *AIP Advances* 3.11 (2013). DOI: 10.1063/1.4828730.
- [87] Y. P. Varshni. “Temperature dependence of the energy gap in semiconductors”. In: *Physica* 34.1 (1967), pp. 149–154. DOI: [https://doi.org/10.1016/0031-8914\(67\)90062-6](https://doi.org/10.1016/0031-8914(67)90062-6).
- [88] G. Kioseoglou et al. “Optical polarization and intervalley scattering in single layers of MoS₂ and MoSe₂”. In: *Sci. Rep.* 6 (2016), p. 25041.
- [89] S. Helmrich et al. “Exciton-phonon coupling in mono- and bilayer MoTe₂”. In: *2D Materials* 5.4 (July 2018), p. 045007. DOI: 10.1088/2053-1583/aacfb7.

- [90] S. Koirala et al. “Homogeneous linewidth broadening and exciton dephasing mechanism in MoTe₂”. In: *Physical Review B* 93.7 (2016), pp. 1–5. DOI: 10 . 1103/PhysRevB . 93 . 075411.
- [91] Y. Liu et al. “Layer-by-layer thinning of MoS₂ by plasma”. In: *ACS Nano* 7.5 (2013), pp. 4202–4209. DOI: 10 . 1021/nn400644t.
- [92] Q. Wang et al. “Precise layer control of MoTe₂ by Ozone treatment”. In: *Nanomaterials* 9.5 (2019). DOI: 10 . 3390/nano9050756.
- [93] Z. Lin et al. “Defect engineering of two-dimensional transition metal dichalcogenides”. In: *2D Materials* 3.2 (2016). DOI: 10 . 1088/2053-1583/3/2/022002.
- [94] H. Nan et al. “Strong photoluminescence enhancement of MoS₂ through defect engineering and oxygen bonding”. In: *ACS Nano* 8.6 (2014), pp. 5738–5745. DOI: 10 . 1021/nn500532f.
- [95] N. Kang et al. “Photoluminescence quenching in single-layer MoS₂ via oxygen plasma treatment”. In: *Journal of Physical Chemistry C* 118.36 (2014), pp. 21258–21263. DOI: 10 . 1021/jp506964m.
- [96] L. Reeves et al. “2D Material Microcavity Light Emitters: To Lase or Not to Lase?” In: *Advanced Optical Materials* 6.19 (2018), pp. 1–11. DOI: 10 . 1002/adom.201800272.